UNIVERSIDADE FEDERAL DO ESPÍRITO SANTO
DEPARTAMENTO DE ENGENHARIA CIVIL
PROGRAMA DE PÓS-GRADUAÇÃO EM ENGENHARIA CIVIL

ANDRÉ VASCONCELOS SOARES GOMES

FINITE ELEMENT MODELLING OF A COLD-FORMED STEEL PROFILE EMPLOYED IN COMPOSITE RIBBED SLABS

VITÓRIA
2020

ANDRÉ VASCONCELOS SOARES GOMES

FINITE ELEMENT MODELLING OF A COLD-FORMED STEEL PROFILE EMPLOYED IN COMPOSITE RIBBED SLABS

A Thesis submitted as a partial fulfilment of the requirements for the Master's Degree in Civil Engineering at Universidade Federal do Espírito Santo. Advisor: Prof.ª Dra. Adenilcia Fernanda Grobério Calenzani

VITÓRIA
2020

FINITE ELEMENT MODELLING OF A COLD-FORMED STEEL PROFILE EMPLOYED IN COMPOSITE RIBBED SLABS

Dissertação apresentada ao Programa de Pós-Graduação em Engenharia Civil do Centro Tecnológico da Universidade Federal do Espírito Santo, como requisito parcial para obtenção do título de Mestre em Engenharia Civil, na área de concentração Estruturas.

Aprovada em 29 de julho de 2020.

COMISSÃO EXAMINADORA

_____
Profª Dra. Adenilcia Fernanda Grobério Calenzani
Doutora em Engenharia Civil
Universidade Federal do Espírito Santo
Orientadora

_____
Prof. Dr. Macksuel Soares de Azevedo
Doutor em Engenharia Civil
Universidade Federal do Espírito Santo
Membro Interno

_____
Eng. Dr. Johann Andrade Ferrareto
Doutor em Engenharia Civil
ArcelorMittal
Membro Externo

_____
Prof. Dr. Luiz Carlos Marcos Vieira Junior
Doutor em Engenharia Civil
Universidade Estadual de Campinas
Membro Externo

To my daughter Ana Lívia and my wife Gabriela.
To my parents Mírian and Edivaldo, and my brother Israel.

ACKNOWLEDGMENTS

Have I not commanded you? Be strong and courageous. Do not be afraid; do not be discouraged, for the Lord your God will be with you wherever you go.

Joshua 1:9

ABSTRACT

Structural systems comprised by prefabricated flooring systems and/or cold-formed steel members are frequently employed in the construction industry due to their versatility, high strength-to-weight ratio, ease of prefabrication, transportation and assembly on site. The unification of these structural systems motivated the creation of composite ribbed slabs, which were defined in this research as ribbed floor systems in which cold-formed steel members are used as joists, and the space between them is filled with inert elements. During concrete casting, the cold-formed steel members are solely responsible for bearing the construction loads, and, after this phase, the steel elements work partially or completely as rebar reinforcement. As part of this structural system, the Trelifácil® solution is the object of study of this research, which is a prefabricated element comprising a trussed girder coupled to a cold-formed steel formwork by plastic spacers. Although these prefabricated joists have already been used to replace reinforced concrete lattice girders, it was only recently that researchers started looking into the design of these structural elements as well as into the feasibility of considering the composite action between components to achieve an economical design. Therefore, the focus of this research is to develop finite element models using ANSYS® 2020R1 capable of predicting the flexural behaviour of the Trelifácil® solution with and without the trussed girder attached to it. Additionally, the outcome of the finite element analyses aims to support the design of physical tests to validate the modelling techniques employed herein. To develop the finite element models, a variety of studies are conducted to assess the main parameters found in the literature review that may influence finite element predictions. The results indicated that the collapse analyses of the cold-formed steel member are sensitive to boundary conditions, loading position, element choice, mesh density, plasticity model and solution scheme. Based on the literature review, this research presented possible modelling techniques for each of these major issues. In addition, the gains in strength and stiffness found with the suggested finite element model for the entire configuration of the Trelifácil® solution reinforced the potential of this structural system that can be derived through the consideration of composite action between its components.

Keywords: Numerical analysis. Cold-formed steel structures. Trelifácil® solution. Composite ribbed slab.

RESUMO

Sistemas estruturais formados por lajes pré-fabricadas e/ou perfis formados a frio são frequentemente empregados na Construção Civil devido à sua versatilidade, alta relação entre resistência *versus* peso, facilidade de fabricação, transporte e montagem. A unificação desses sistemas estruturais deu origem às lajes nervuradas mistas, as quais são definidas nesta pesquisa como sistema de lajes com elementos inertes de enchimento e nervuras com fôrma de aço em perfil formado a frio. Antes da cura do concreto, o perfil de aço resiste isoladamente às cargas de construção e, após a cura, atua como toda ou parte da armadura de tração. Como parte desse sistema estrutural, a solução Trelifácil® é destacada nesta pesquisa, a qual corresponde a uma armadura treliçada acoplada numa fôrma de aço por meio de espaçadores plásticos. Embora essas vigotas de aço pré-fabricadas pareçam uma opção promissora como substituição às vigotas treliçadas de concreto, apenas recentemente pesquisadores começaram a analisar seu desempenho estrutural bem como a viabilidade de incluir a ação mista entre seus componentes para alcançar seu dimensionamento econômico. Portanto, o foco desta pesquisa é desenvolver modelos de elementos finitos utilizando o ANSYS® 2020R1, os quais devem ser capazes de prever o comportamento à flexão da solução Trelifácil® com e sem a armadura treliçada acoplada à forma de aço. Além disso, o resultado da análise em elementos finitos visa apoiar a construção de ensaios laboratoriais para validar as técnicas de modelagem aqui empregadas. Para desenvolver os modelos em elementos finitos, vários estudos de sensibilidade são conduzidos avaliando os principais parâmetros encontrados na revisão de literatura que podem influenciar as previsões numéricas para perfis formados a frio. Em resumo, as análises numéricas do perfil formado a frio foram altamente sensíveis às condições de contorno, posição de carregamento, escolha do elemento finito, densidade de malha, modelo de plasticidade e esquema de solução. Com base na revisão da literatura, esta pesquisa apresentou possíveis técnicas de modelagem para cada uma dessas questões. Além disso, os ganhos de resistência e rigidez encontrados com o modelo de elementos finitos sugerido para toda a configuração da solução Trelifácil® reforçaram o potencial desse sistema estrutural que pode ser obtido por meio da consideração da ação mista entre seus componentes.

Palavras-chave: Análise numérica. Perfis formado a frio. Solução Trelifácil®. Laje nervurada mista.

LIST OF FIGURES

LIST OF TABLES

LIST OF ABBREVIATIONS

CFS	Cold-Formed Steel
SFEA	Shell Finite Element Analyses
DSM	Direct Strength Method
AISI	American Iron and Steel Institute
GMNIA	Geometric and Material Nonlinear Analysis with Imperfections Included
SFEM	Shell Finite Element Model
FE	Finite Element
CDF	Cumulative Distribution Function
FSM	Finite Strip Method
GBT	Generalised Beam Theory
LVDT	Lateral Variable Displacement Transducers

CONTENTS

1 INTRODUCTION

1.1 Background

In the last decades, the construction industry has greatly progressed by seeking more efficient and economical solutions. In this context, prefabricated structural systems play a significant role since they are manufactured in a controlled environment and present fast installation. Among them, steel lattice girders and cold-formed steel (CFS) structures are highlighted in this research. Lattice girders are usually used in prefabricated flooring systems of small and medium-sized constructions and have been, since their inception, an accessible option due to their simple construction techniques. Cold-formed steel members, in turn, may reduce the cost of structures as a result of its lower weight, relatively easy method of manufacturing, fast assembly, easy transportation and handling, high strength and stiffness, and others, when compared to materials such as timber and concrete. The numerous attempts to combine the accessibility of prefabricated slabs with the mechanical capacity of cold-formed structures, resulted in the development of composite ribbed slabs, defined herein as ribbed floor systems in which cold-formed steel profiles are used as girders, and the space between them is filled with inert elements. During concrete casting, the steel profiles are solely responsible for bearing the construction loads, and, after this phase, the steel elements work partially or completely as rebar reinforcement. The object of study in this research is a cold-formed steel profile coupled with a lattice girder employed in composite ribbed slabs. A brief description of this structural system and its component is given in subsequent sections.

1.2 Prefabricated slabs featuring lattice girders

According to Caixeta (1998), prefabricated slabs with lattice girders, or simply lattice slabs, are a result of the evolution of flat reinforced concrete slabs that, which quickly developed into cast-in-place ribbed slabs. These flooring systems progressed to prefabricated slabs, designated as such due to the employment of industrialized reinforced or prestressed concrete girders. Subsequentially, steel reinforcement lattices were added to said girders, and the resulting structural system was designated as lattice slab. A development timeline of lattice slabs is illustrated in Figure 1.1.

Among the advantages of lattice slabs, one can highlight the accessibility of its

components as well as the design procedures already well established commercially. These slabs are formed by lattice girders spaced by means of inert elements and covered by a cast-in-place concrete layer. This configuration allows a straightforward and fast assembly when compared to other reinforced concrete floor systems. For structural design purposes, tables published in catalogues based on design standards are typically employed in the construction industry. Furthermore, various computational packages offer tools for their application in structural design models. For these reasons, prefabricated slabs with lattice girders became commonplace in structural systems.

Figure 1.1 — Evolution of concrete flooring systems.
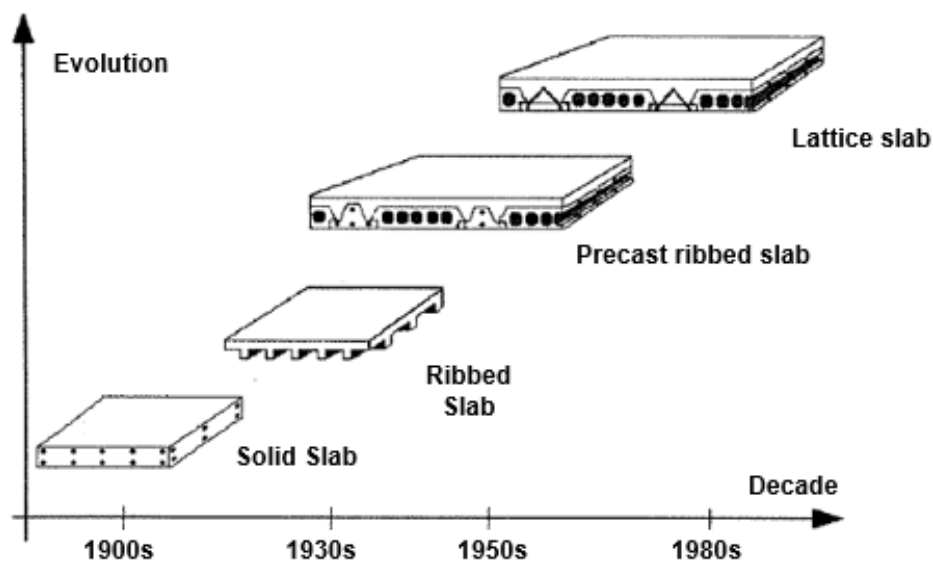
Source: Caixeta (1998).

1.3 Cold-formed steel members

Cold-formed steel profiles are structural members formed at room temperature via two main manufacturing processes: (i) press brake operations (Figure 1.2a) and (ii) cold roll forming machines (Figure 1.2b). Press brake operations consist of forming predetermined products by pressing the workpiece between a movable punch tool and die, as illustrated in Figure 1.2a. Alternatively, a cold roll forming machine is a set of paired rolls that progressively shapes a flat metal sheet into a particular profile, as shown in Figure 1.2b. Press braking operations may be used when producing a small quantity of members that require simpler configuration (YU; LABOUBE; CHEN, 2019).

Figure 1.2 — Processes of (a) press-braking and (b) roll forming to manufacture cold-formed steel members.

(a)Press-braking

(b)Roll forming
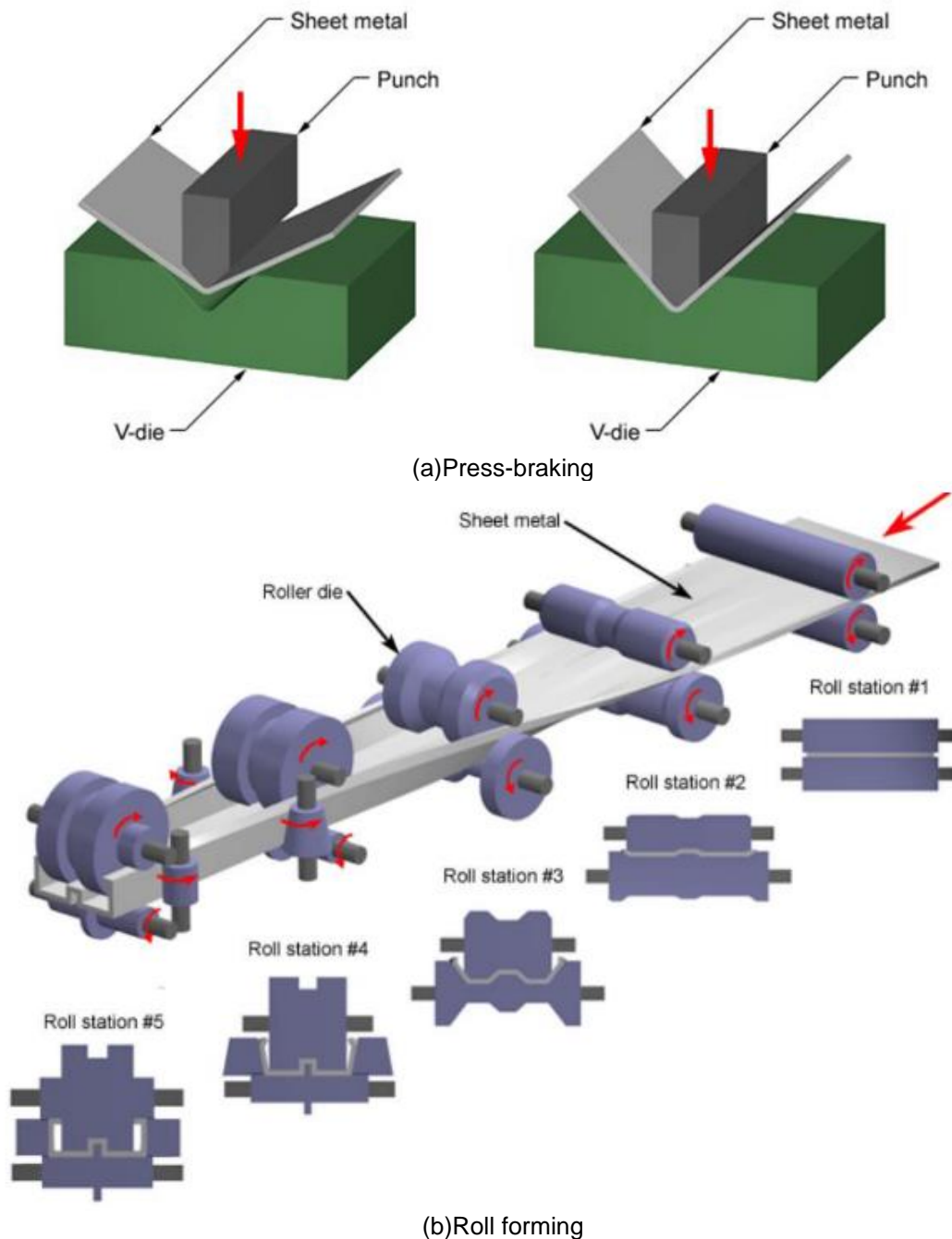
Source: ("Sheet Metal Forming", [s.d.])

1.4   Composite ribbed slabs

Composite ribbed slabs can be considered as a combination of prefabricated slabs and cold-formed steel structures. In these systems, cold-formed steel members are used as formwork for the ribs of the slab. In both commercial and academic contexts, composite ribbed slabs have been used and studied, respectively. Examples of scientific literature on composite ribbed slabs include the works conducted by Takey

(2001) (Figure 1.3a), Beltrão (2003) (Figure 1.3b), Vieira (2003) (Figure 1.3d) and Vianna (2005) (Figure 1.3c), who proposed different systems of composite ribbed slabs. In the commercial context, two flooring systems can be used as example of such a system: Tuper slab system (Figure 1.4) and slabs formed by the Trelifácil® solution (Figure 1.5 and Figure 1.6). Generally, the chief objective of these proposals is to optimise manufacturing and assembly aspects such as safety, cost, factory productivity and sustainability, while also minimising the cost and time of transportation. In this research, the Trelifácil® solution is the object of study, shortly described in subsequent sections, which also list the investigations performed herein.

Figure 1.3 — Cross-sectional view of four different composite ribbed slabs.

a) Takey (2001)   b) Beltrão (2003)

c) Vianna (2005)   d) Vieira (2003)

Source: Takey (2001), Beltrão (2003), Vieira (2003) and Vianna (2005).

Figure 1.4 — Tuper composite ribbed slabs.
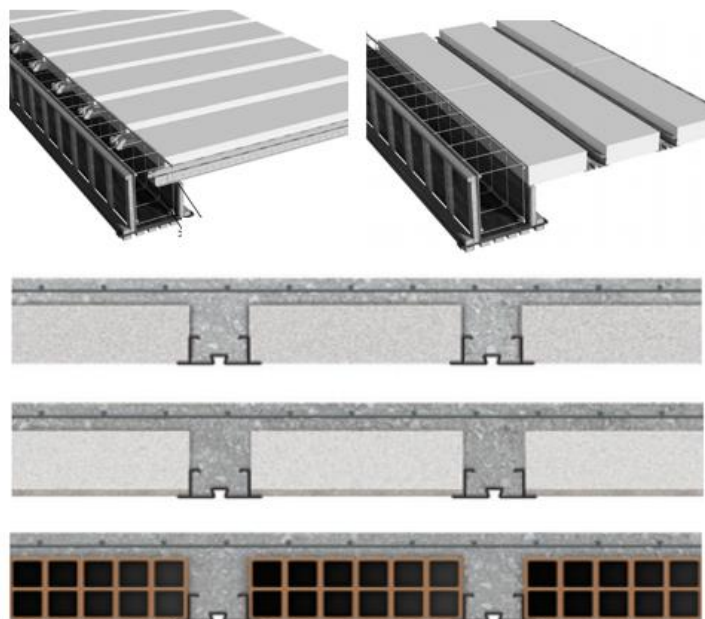
Source: (TUPER, [s.d.]).

Figure 1.5 — Composite ribbed slabs featuring the Trelifácil® solution.

Source: (ARCELORMITTAL, 2017b).

Figure 1.6 — Assembly of Trelifácil® composite ribbed slabs.

Source: ("Trelifácil® - Lajes Real", [s.d.]).

1.5 Trelifácil® solution

1.5.1 Initial considerations

The Trelifácil® solution uses plastic spacers to couple a lattice girder to a cold-formed steel formwork, forming a single element, as shown in Figure 1.7. Figure 1.8 illustrates the manufacturing process of the steel formwork, which employs the cold-forming technique. Figure 1.9 shows the cross-section dimensions of the CFS formwork, which is manufactured with a length of six meters.

Figure 1.7 — Configuration of the Trelifácil® solution.
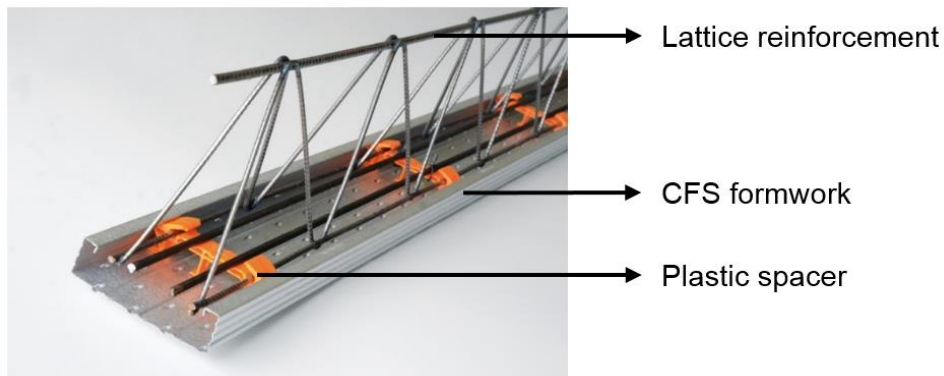
Source: (ARCELORMITTAL, 2017b).

Figure 1.8 — Manufacturing process of the Trelifácil® solution using cold-forming process.
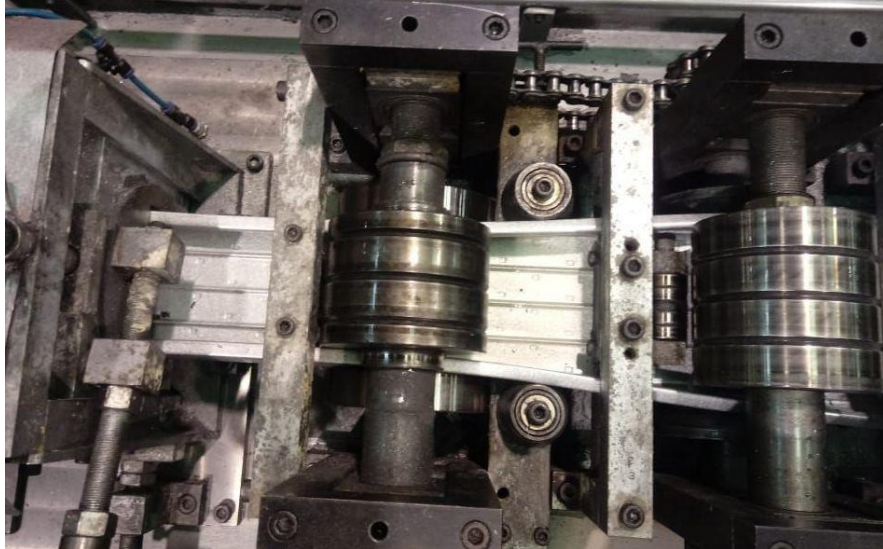
Source: author's own.

Figure 1.9 — Cross-section dimensions of the formwork used in the Trelifácil® solution.
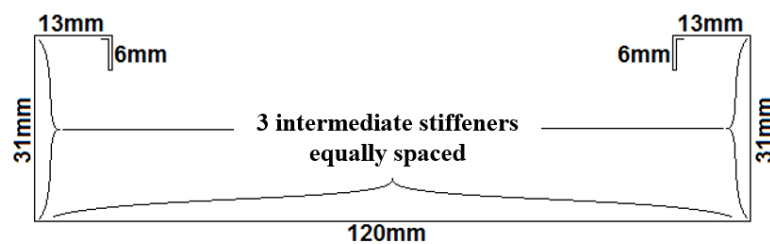
Source: author's own.

Although the Trelifácil® solution is already commercialised and used in the construction industry, in-depth investigations of its mechanical responses began recently. Currently, this system is designed similarly in similar fashion to concrete lattice girders, consolidated in the Brazilian market for decades. Studies concerning the behaviour of these girders during construction and serviceability phases date from the late 90's and early 2000's [see Gaspar (1997), Droppa Jr. (1999) and Magalhães

(2001)]. For construction loads (before concrete curing), design follows the Brazilian standard of propping for concrete structures: ABNT NBR 15696:2009 (Formworks and shoring for concrete structures — Bill, dimensioning and procedures executives). After concrete curing, the design follows ABNT NBR 6118:2014 (Design of concrete structures — Procedure). Therefore, studies have been carried out to propose specific design procedures for this system, as well as to examine its structural response. These studies are briefly described in the following section.

1.5.2 *Existing investigations on the use of the Trelifácil® solution*

The main investigations to date on the use of the Trelifácil® solution were conducted by Favarato (2018), who developed a computational tool to predict the resistance capacity of flooring systems featuring this element. A simplified design procedure was proposed based on Brazilian standards ABNT NBR 14762:2010, ABNT NBR 6118:2014, ABNT NBR 8800:2008 and ABNT NBR 14859-2:2016. Two main cases were considered in this study: flooring systems (i) without or (ii) with the use of temporary propping during construction phase, i.e., before concrete curing, in which the cold-formed steel formwork is subjected to dead loads and construction live load. For both cases, parametric studies were performed varying parameters related to geometry, service loads and materials, from which results were used to elaborate design tables with maximum spans and loads for pre-defined slab geometries. Then, the main conclusions were drawn regarding the maximum span that can be reached without or with shoring.

The findings for the first case, i.e., for simply supported slabs without shoring during construction, are also reported in Favarato et al. (2019b). For this case, two different scenarios of geometry and material properties were analysed:

a) scenario 1: 5 cm concrete layer thickness and 27x8 cm light filling inert blocks;

b) scenario 2: 6 cm concrete layer thickness and 37x8 cm light filling inert blocks.

In addition, three different cross-section thicknesses for the steel formwork were evaluated. Results indicated that slab span lengths up to 1.2 m can be used without shoring for the steel formwork with nominal geometry properties (cross-section thickness of 0.65 mm) and yield stress of 340 MPa. In this case, the limit state related

to combined bending and shear of the steel formwork, i.e., before concrete curing, governed the design of the slab. Alternatively, the design of thicker cold-formed steel formworks is governed by excessive deflection. However, it is important to mention that the composite action between steel formwork and trussed girder was neglected, since this expected behaviour is still not grounded on measured data. Therefore, this flooring system may reach longer span lengths by considering the coupled behaviour between the components of the Trelifácil® solution.

Due to the low flexural strength and stiffness of the steel formworks, Favarato (2018) conducted studies considering the use of temporary propping during construction in the design calculations, which is also reported in Favarato et al. (2020). Maximum live load versus span lengths found for the two aforementioned scenarios are shown in Figure 1.10, in which limit states related to service loads governed the slab designing. To achieve such results, Favarato et al. (2020) concludes that a mean propping distance of 0.80 m must be used. In this case, the steel formworks were designed as continuous beams, which led to different limit states. Local instability related to combined negative bending and shear of the steel formwork controlled the maximum propping distance design. Therefore, longer propping distances may be achieved due to the potential increase of flexural strength and stiffness promoted by the composite action between the Trelifácil® solution components.

Furthermore, Gomes et al. (2019) conducted four-point bending tests of simply supported beams in order to assess the design procedures used by Favarato (2018) to predict the moment capacity of the cold-formed steel formwork used in the Trelifácil® solution. Also, these physical tests were also used as a pilot experiment to support the experimental layout proposed by Candido (2020, in progress). Overall, good agreement was found between theoretical and experimental results and the testing techniques of Candido (2020, in progress) worked satisfactorily. Since the findings of Gomes et al. (2019) are also part of this research, they are later detailed in this thesis.

Although Favarato (2018) developed a robust computational tool for the design of flooring systems using the Trelifácil® solution, simplifications were taken which must be assessed by laboratorial measurements. Hence, Candido (2020, in progress) proposes the execution of a variety of physical tests to evaluate the main assumptions of Favarato (2018) and to quantify the potential benefits of the composite action between components of this floor system before and after concrete curing. Specifically,

the tests aim to: (i) determine the bending resistance of the cold-formed steel member used as formwork in the Trelifácil® solution, (ii) evaluate the gains in flexural strength and stiffness by considering the composite action between components before concrete curing, (iii) determine the mechanical capacity of the system after concrete curing and (iv) assess the benefits of the composite action between cold-formed steel member and concrete after concrete curing. Therefore, Candido (2020, in progress) aims to determine if an economical design of such a system can be achieved by considering the composite action between its elements.

Furthermore, Gomes et al. (2019) conducted four-point bending tests of simply supported beams in order to assess the design procedures used by Favarato (2018) to predict the moment capacity of the cold-formed steel formwork used in the Trelifácil® solution. Plus, these physical tests were also used as a pilot experiment to support the experimental layout proposed by Candido (2020, in progress). Overall, good agreement was found between theoretical and experimental results and the testing techniques of Candido (2020, in progress) worked satisfactorily.

Figure 1.10 — Overload for two different scenarios of geometry and material properties for the flooring system using the Trelifácil® solution.
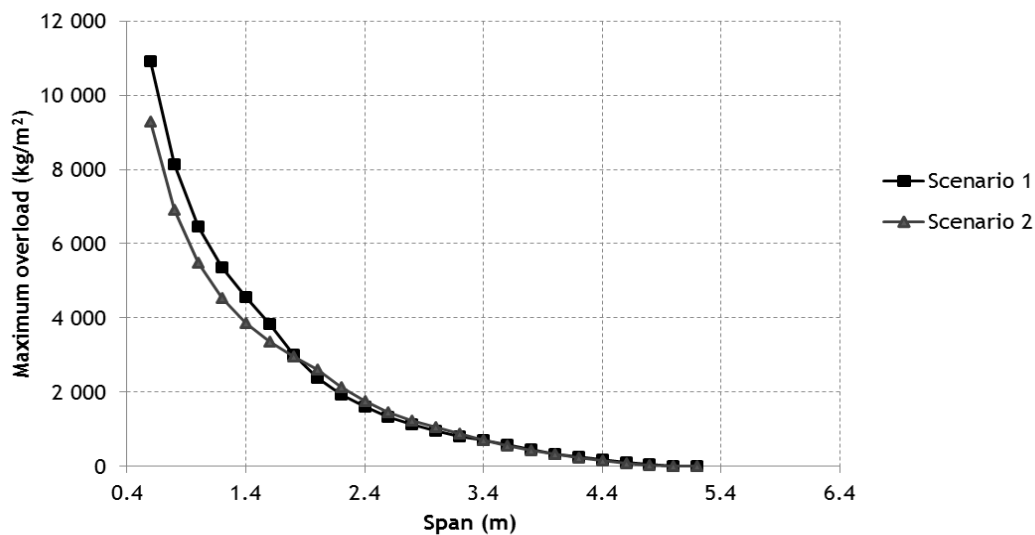
Source: (FAVARATO, 2018).

In summary, Favarato (2018) proposed a design approach based on the scope of current structural design codes to estimate the complex mechanical capacity of flooring systems using the Trelifácil® solution through suitable simplifications and assumptions. A portion of the research work was already validated by laboratory measurements of Gomes et al. (2019) and the remaining procedure will be assessed by the research of Candido (2020, in progress). In addition, the tests conducted by

Candido (2020, in progress) will quantify the potential improvements in the mechanical behaviour of such a system due to the interaction between its elements. However, even though an extensive set of physical tests has been proposed by Candido (2020, in progress), complementary approaches must be used to extrapolate laboratory results. Thus. This demand shaped the main motivations and objectives of this research, which are described in the following section.

1.6   Research motivation

In the civil construction industry, composite ribbed slabs, category in which the Trelifácil® solution belongs, have great growth potential. This is justified mainly due to their industrialised characteristics, which are always looking forward to optimising cost and delivery time, as well as improving sustainable factors. An example of such advantages is the substitution of temporary formworks by permanents ones, which enhances the assembly productivity. The basic problem to achieve economic design for these composite ribbed slabs is associated with its maximum structural efficiency, which may be improved by enhancing the interaction between its elements. Although the benefits of steel and concrete composite structures are well-known, no research appears to have been conducted on the improvements achieved by exploiting the composite action between cold-formed steel and associated elements of the composite ribbed slabs formed by the Trelifácil® solution. Thus, optimal design of this flooring system can be achieved through studies focused on the composite action of the materials.

Due to the presence of different structural components interacting with each other, composed of materials with different properties and an unusual geometry, the analysis of composite ribbed slabs denotes a wide complexity. The usual alternative for this type of problem is the structural characterisation performed experimentally, which examines the behaviour of the system with destructive tests. On the other hand, laboratory tests do not allow the evaluation of all parameters related to the composite interaction between materials and may require expensive techniques for their set-up. An alternative to time and cost consuming experimental studies for problems of this difficulty is the use of sophisticated shell finite element analyses (SFEA), accounting for initial geometrical and physical imperfections and employing nonlinear constitutive laws. Thus, through numerical simulations validated by laboratory measurements, similarly to the concept of digital twins, it is possible to expand the empirical results

and evaluate other possible parameters that allows the characterisation of the structural behaviour of composite ribbed slabs.

1.7 Objectives

The primary objective of the research described in this thesis is to develop a sound basis for finite element modelling of the cold-formed steel profile used in the Trelifácil® solution, through nonlinear numerical analysis performed using the software ANSYS® 2020R1. Additionally, the outcome of this research aims to support the design of physical tests of the ongoing research of Candido (2020, in progress), which can be used in the future to validate the accuracy of the developed modelling techniques presented in this thesis.

As such, the specific objectives of this research are summarised as follows:

a) propose finite element models to predict the flexural strength of the Trelifácil® solution;

b) assess the sensitivity of the models to a variety of parameters and compare its results with laboratory measurements;

c) evaluate the influence of the main parameters that may affect the flexural resistance of the Trelifácil® solution.

1.8 Outline of the dissertation

Chapter 1 gives a brief introduction to the main components employed in composite ribbed slabs, i.e., prefabricated slab systems and cold-formed steel members, as well as a summary of the existing investigations on the use of the Trelifácil® solution. The chapter also presents the motivation and objectives to initiate this research work and the outline of this dissertation.

Chapter 2 provides a review of the literature on topics relevant to the modelling of the structural response of cold-formed steel members. It includes a review of the theoretical background behind the design of cold-formed steel beams and existing research on the modelling of geometrical imperfections, material models, residual stresses, element section, solution schemes and cases in which beams subjected to flexure about minor axis were analysed. In this chapter, a review of existing researches on lattice reinforcement is also presented.

Chapter 3 presents the finite element approaches used to model the flexural

behaviour of the Trelifácil® solution. In this chapter, comparisons between numerical results and available laboratory measurements of physical tests conducted on the steel formwork of the Trelifácil® solution are given to demonstrate the validity and accuracy of the modelling techniques proposed.

Chapter 4 presents the results of parametric studies of the main geometrical characteristics of the Trelifácil® solution and its components. This section also presents results from a comparative study between predictions from theoretical analyses and the finite element-based method presented in Chapter 3.

In Chapter 5, important findings and conclusions from this research are summarised. Suggestions for further work are also given.

2 LITERATURE REVIEW

The investigation of the structural behaviour of cold-formed steel members and lattice girders under a variety of load and boundary conditions is fundamental to the improvement of design criterions of these prefabricated systems and, consequently, the whole construction industry.

Therefore, in order to contribute to the knowledge development of such structural systems, it is necessary to comprehend their current state-of-the-art. As such, this literature review is divided in three main sections that include: (i) theoretical formulations to calculate the bending resistance of cold-formed steel beams, (ii) finite element (FE) techniques used to model cold-formed steel members and (iii) current researches that investigate the structural behaviour of lattice reinforcements. These sections cover the main theoretical background employed in this research.

2.1 Theoretical prediction of the flexural resistance of cold-formed steel beams

As previously mentioned, Favarato (2018) proposed design procedures to estimate the resistance capacity of floor systems featuring the Trelifácil® solution. The determination of the flexural capacity of the cold-formed steel formwork used in the Trelifácil® solution was based on the Direct Strength Method (DSM) for beams presented in the Brazilian standard ABNT NBR 14762:2010. An in-depth review of this method is outside the scope of this research since its main goals are related to the finite element modelling of cold-formed steel beams. Hence, only a succinct description of the method and the formulations used in this research are presented.

The DSM was proposed by Schafer (2008), firstly mentioned in Schafer and Peköz (1998a), and rooted in the research work of Hancock, Kwon and Bernard (1994). Hancock, Kwon and Bernard (1994) suggested strength design curves to predict the capacity of cold-formed steel sections undergoing distortional buckling, unlike the concept of effective width in which local buckling is analysed. The DSM, in turn, considers in its strength curves the interaction between local and global instabilities, as well as post-buckling reserve. Then, the basic premise of the DSM is to extend the results of elastic buckling analyses to ultimate strength through semi-empirical strength curves, shown in Figure 2.1 for beams (SCHAFER, 2008). Therefore, the accuracy of this method is intrinsically related to the estimate of the critical elastic moments of a

member. Further details of this method can be found on many papers and books, such as Schafer (2008) and Yu, LaBoube and Chen (2019). Discussions on the theory of stability and coupled instabilities in steel structures can be found on Rondal (1998).

Figure 2.1 — Comparison between theoretical and test data for flexural strength (M_{test}) using the Direct Strength Method.
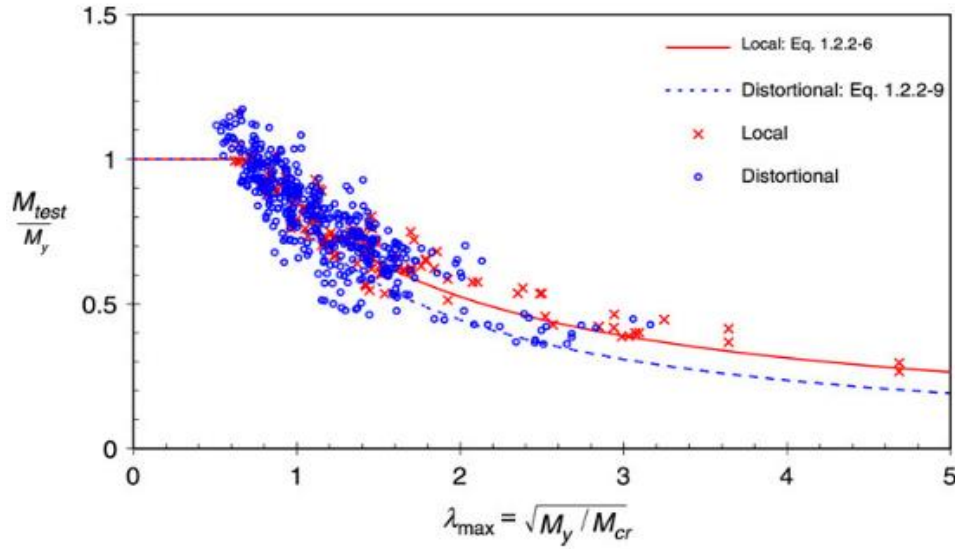
Source: (SCHAFER, 2008).
Note: The referred Equations 1.2.2-6 and 1.2.2-9 are respectively given by Equation (2.5) and Equation (2.7) normalised against the moment at first yield, M_y. M_{cr} refers to the critical elastic moment of local or distortional buckling.

According to the DSM, the design value of the bending moment resistance M_{Rd} of a gross cross-section is determined by Equation (2.1):

$$M_{Rd} = \frac{M_{Rk}}{\gamma} \tag{2.1}$$

where γ is equal to 1,1 and M_{Rk} corresponds to the characteristic resistance to bending moment, which is the smallest value among nominal flexural strengths: $M_{R,e}$ (where the 'e' stands for Euler buckling) for lateral-torsional buckling, $M_{R,\ell}$ for local buckling and $M_{R,dist}$ for distortional buckling.

The nominal flexural strength for global instability $M_{R,e}$ is given by:

$$M_{R,e} = \begin{cases} W f_y \text{ for } \lambda_0 \leq 0,6 \\ 1,11\big(1 - 0,278\lambda_0{}^2\big)W f_y \text{ for } 0,6 < \lambda_0 < 1,336 \\ W f_y/\lambda_0{}^2 \text{ for } \lambda_0 \geq 1,336 \end{cases} \tag{2.2}$$

where W is the elastic section modulus referenced to the extreme fibre in first yield and f_y corresponds to the yield stress. The slenderness factor λ_0, associated to lateral torsional buckling, is given as follows:

$$\lambda_0 = \sqrt{\frac{W f_y}{M_e}} \tag{2.3}$$

where M_e is the elastic critical moment for flexural-torsional buckling. Although M_e may be obtained from computational stability analysis, for singly symmetric sections bending about the centroidal axis perpendicular to the symmetry axis, this variable can be computed by using Equation (2.4):

$$M_e = \frac{C_s N_{ex}}{C_m} \left[j + C_s \sqrt{j^2 + r_0^2 \left(\frac{N_{ez}}{N_{ex}} \right)} \right] \tag{2.4}$$

The detailed definition and calculation procedure for each of the variables involved in determining M_e are obtained from subsection 9.8.2.2 of the Brazilian standard ABNT NBR 14762:2010.

The nominal flexural strength for local instability $M_{R,\ell}$ is given by:

$$M_{R,\ell} = \begin{cases} M_{R,e} \text{ for } \lambda_\ell \leq 0{,}776 \\ \left(1 - \frac{0{,}15}{\lambda_\ell^{0,8}} \right) \frac{M_{R,e}}{\lambda_\ell^{0,8}} \text{ for } \lambda_\ell > 0{,}776 \end{cases} \tag{2.5}$$

where the slenderness factor associated with local instability λ_ℓ is given by:

$$\lambda_\ell = \sqrt{\frac{M_{R,e}}{M_\ell}} \tag{2.6}$$

where M_ℓ refers to the elastic critical moment of local buckling, obtained from elastic stability analysis.

The nominal flexural strength for local instability $M_{R,dist}$ is given by:

$$M_{R,dist} = \begin{cases} W f_y \text{ for } \lambda_{dist} \leq 0{,}673 \\ \left(1 - \frac{0{,}22}{\lambda_{dist}} \right) \frac{W f_y}{\lambda_{dist}} \text{ for } \lambda_{dist} > 0{,}673 \end{cases} \tag{2.7}$$

where the slenderness factor associated to distortional instability λ_{dist} is given by:

$$\lambda_{dist} = \sqrt{\frac{W f_y}{M_{dist}}} \tag{2.8}$$

where M_{dist} refers to the elastic critical moment of distortional buckling, obtained from elastic stability analysis.

Concerning the determination of critical buckling moments, an elastic stability

analysis must be sought. There exists a variety of methods implemented in computational tools to perform those analyses. In the DSM design guide published by the American Iron and Steel Institute (AISI, 2006), four alternatives are described: finite strip method, finite element method, generalised beam theory or closed-form solutions (i.e., manual elastic buckling solutions). Procedures for the application of these methods are given in the DSM design guide (AISI, 2006), as well as examples of a variety of computational tools and codes to perform those analyses. In this research, such analysis is conducted using the finite strip software CUFSM (LI; SCHAFER, 2010; SCHAFER; ÁDÁNY, 2006), which provides the stability solution by means of a signature curve for thin-walled members based on the material properties and cross-sectional shape. Then, mode shapes, elastic critical loads and half-wavelengths can be derived from this open-source software.

Finally, by using the DSM, the determination of elastic deflection of cold-formed steel beams must consider an effective second moment of area (I_{ef}) linearly proportional to the strength of the section at the serviceability stress of interest, as follows:

$$I_{ef} = I_g \left(\frac{M_{Rser}}{M_n} \right) \leq I_g \tag{2.9}$$

where I_g is the moment of inertia of the gross cross-section, M_{Rser} is the minimum of the member strengths determined according to Equations (2.2), (2.5) and (2.7) but with $W f_y$ replaced with M_n, which is the bending moment at the service loads to be considered.

2.2 Finite element modelling of cold-formed steel members

2.2.1 Initial considerations

Currently, a powerful technique to study the strength behaviour of structural members is the use of a geometric and material nonlinear analysis with imperfections included (GMNIA). For thin-walled structures, shell finite element model (SFEM) is commonly developed to conduct a GMNIA. According to Schafer and Peköz (1998b), the computational prediction of the ultimate strength and collapse behaviour of CFS members using SFEM are sensitive to: solution schemes, element type and discretisation, boundary conditions, plasticity models, initial geometrical imperfections and initial residual stresses and strains. Therefore, in the following sections some of

these factors are briefly discussed. Also, each section shortly reviews the employment of these parameters in the researches of Torabian, Zheng and Schafer (2014), Martins, Camotim and Dinis (2017), Kyvelou, Gardner and Nethercot (2018), Matsubara, Batista and Salles (2019) and Santos, Landesmann and Camotim (2019), enable us to review a diversity of finite element modelling techniques.

2.2.2 *Geometric imperfections*

According to Ziemian (2010), initial imperfection of steel structures is "an unavoidable deviation from perfect geometry which is within the accepted practical tolerance of the particular applicable fabrication technology". In general, authors classify geometric imperfections in two groups: global imperfections (flexure and flexure-torsional) and cross-sectional imperfections (local and distortional). Although in the last decades many researchers focused on the investigation of this subject, no consensus is found on the correct application of geometric imperfections in FE modelling of CFS structural members (FARZANIAN et al., 2019, preprint).

Schafer, Li and Moen (2010) stated that imperfections can be included in FE models as a modelling convenience or a physical reality. The first approach is usually used for either design purposes or to trigger expected deformed shapes. Generally, for modelling convenience, authors employ buckling modes as imperfection distribution factored by section thickness or plate slenderness. In the case of adding imperfections as a physical reality, one of the main objectives, according to Farzanian et al. (2019, preprint), is to generate statistical data for the construction of geometric imperfection models of different CFS sections. Then, an attempt is made to reliably reconstruct a given structural geometry by accurately measuring the imperfections, as the characterization method proposed by McAnallen et al. (2014). In this research, geometric imperfections are applied as a modelling convenience; for this reason, greater emphasis is placed on this approach.

One can find a plethora of procedures for modelling initial geometrical imperfections in the literature. As stated before, the most common approach uses a superposition of eigenmode shapes. Farzanian et al. (2019, preprint) conducted a comparative review of the current geometric imperfection models for CFS structural members. The authors stated that imperfection distributions $[G_m(x, y, z)]$ are commonly assumed by the following form:

$$G_m(x,y,z) = \sum_{i=1}^{n} c_i \alpha_i \phi_{di}(x,y,z)$$

where $\phi_{di}(x,y,z)$ corresponds to imperfection shapes, α_i to their magnitudes and c_i to combination coefficients. The imperfection shapes $\phi_{di}(x,y,z)$ are usually associated with buckling modes, such as bow, camber, twist, local and distortional shapes, as shown in Figure 2.3. Magnitudes α_i are based on measured data, empirical relations or standardised tolerances. The combination coefficients are useful to approximate numerical and experimental results by combining the factored buckling modes. In their literature review, the authors describe the models proposed by Dawson and Walker (1972), Schafer and Peköz (1998b), Sivakumaran and Abdel-Rahman (1998), Sun and Butterworth (1998), Chou, Chai and Ling (2000), Gardner (2002), Dinis and Camotim (2008, 2009, 2010), Zeinoddini (2011), Torabian et al. (2016a, 2016b), Australian Standard AS 4084:2012 (Steel storage rackling) and the European code EN 1993-1-6:2007 (Design of Steel Structures – Part 1.6: strength and stability of shell structures).

Figure 2.2 — Representation of geometric imperfection shapes: (a) combined modes, (b) bow, (c) camber, (d) twist, (e) local and (f) distortional.
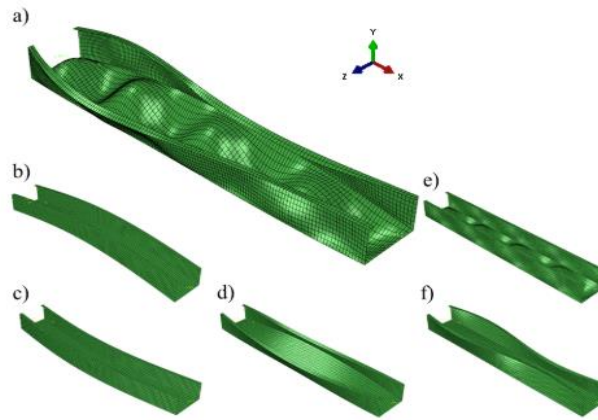
Source: (FARZANIAN et al., 2019, preprint).

Schafer and Peköz (1998b), for example, proposed magnitude values for local and distortional imperfection modes using empirical expressions and probabilistic analyses. Data collected from 11 different experimental studies were used to classify geometrical imperfection distributions into two categories: type 1 (local mode), which is the maximum web amplitude (d_1); and type 2 (distortional mode) characterised by the maximum stiffened flange amplitude (d_2), as illustrated in Figure 2.3. The proposed rules of thumb and statistical values are respectively displayed in Table 2.1 and Table 2.2. In these tables, t represents the section thickness, w the plate width and $P(\Delta < d)$ the cumulative distribution function of the random variable d (imperfection amplitude).

To exemplify the use of the table, a value $P(\Delta < d)$ taken as 0.95 corresponds to the d/t equal to 1.35 for type 1 and 3.44 for type 2. In other words, in a typical CFS section the maximum amplitude is expected to be greater than or equal to these values five per cent of the cases.

Figure 2.3 — Representation of the imperfection shapes type 1 and type 2.
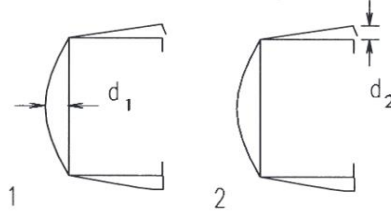
Source: (SCHAFER; PEKÖZ, 1998b).

Table 2.1 — Approximate expressions for local and distortional imperfection magnitudes.

Imperfection type	Approximate expression	
type 1	$d_1 \approx 0.006w$	for $\frac{w}{t} < 200$
type 1 (alternative rule)	$d_1 \approx 6te^{-2t}$ (d_1 and t in mm)	for $\frac{w}{t} < 200$
type 2	$d_2 \approx t$	for $\frac{w}{t} < 100$

Source: (SCHAFER; PEKÖZ, 1998b).

Table 2.2 — Cumulative Distribution Function (CDF) values of geometric imperfections types 1 and 2.

	Type 1	Type 2
$P(\Delta < d)$	d_1/t	d_2/t
0.25	0.14	0.64
0.50	0.34	0.94
0.75	0.66	1.55
0.95	1.35	3.44
0.99	3.87	4.47
Mean	0.50	1.29
Standard deviation	0.66	1.07

Source: (SCHAFER; PEKÖZ, 1998b).

Furthermore, the employment of such geometrical imperfection distributions relies on the extraction of elastic buckling modes of CFS members. Generally, authors perform an eigenvalue finite element analysis in order to generate meshes with imperfections associated to buckling mode shapes. However, the finite element stability analysis captures a high number of modes with buckling interaction, which makes selecting the appropriate imperfection shapes difficult. For this reason, other researchers employ different methods to perform elastic buckling analysis, such as the finite strip (FSM) and the generalized beam theory (GBT). Chodraui et al., (2006), Schafer, Li and Moen (2010), Haidarali (2011) and Kyvelou, Gardner and Nethercot,

(2018), for example, used the finite strip software CUFSM (SCHAFER; ÁDÁNY, 2006) to extract the buckling mode shapes. Then, the eigenvalues can be used to manually create the perturbed meshes or to verify the accuracy of finite element buckling analyses.

In what follows, the modelling techniques used to apply geometrical imperfections in the finite element models of different authors are shortly presented.

2.2.2.1 Torabian, Zheng and Schafer (2014)

Torabian, Zheng and Schafer (2014) modelled geometric imperfections of lipped channel sections by using buckling mode shapes as imperfection distributions. They state that for short members (like the specimens tested in the research), only local buckling modes and/or distortional buckling modes should be applied in the model, since global modes of failure are not predominant. Therefore, a sensitivity analysis was conducted to find the appropriate magnitude factor and sign of each imperfection shape to accurately predict ultimate load and failure mode of experimental tests. Magnitude factors for each imperfection shape were taken from a statistical summary provided by Zeinoddini and Schafer (2012), which is displayed in Table 2.3. The selected imperfection shapes correspond to local and distortional buckling with magnitudes of 50% of the CDF. In addition, eigen buckling analysis was conducted in the finite strip software CUFSM (SCHAFER; ÁDÁNY, 2006) to generate the imperfection modes used in the shell finite element model developed.

Table 2.3 — Magnitudes factors for local, distortional, bow, camber and twist imperfection shapes.

CDF	Local (δ_0/t)	Distortional (δ_0/t)	Bow (L/d_0)	Camber (L/d_0)	Twist (deg/m)
Mean	0,47	1,03	2242	3477	0,36
St.dev.	0,62	0,97	3054	5643	0,23
25%ile[a]	0,17	0,43	4755	6295	0,2
50%ile	0,31	0,75	2909	4010	0,3
75%ile	0,54	1,14	1659	2887	0,49
95%ile	1,02	3,06	845	1472	0,85
99%ile	3,87	4,46	753	1215	0,95

Source: (ZEINODDINI; SCHAFER, 2012).
Note "a": %ile values are the probabilities that imperfection will be less than the table values.

Another important aspect of initial geometrical imperfection modelling is the measurement of actual dimensions of the member cross-section. For this reason, Torabian, Zheng and Schafer (2014) carried out nonlinear analyses using two types of geometric dimensions: nominal and actual measured dimensions. They found that

nominal dimensions can provide results close to actual dimensions and, therefore, they were used to build the numerical model.

2.2.2.2 Martins, Camotim and Dinis (2017)

Martins, Camotim and Dinis (2017) followed recommendations given by Dinis and Camotim (2010) to identify the appropriate perturbed mesh for their finite element model. The approach recommended by Dinis and Camotim (2010) is illustrated in Figure 2.4, in which "pure" local and distortional modes, factored by $0.1t$, are linearly combined by $C_{L,0}$ (local combination factor) and $C_{D,0}$ (distortional combination factor), so that $(C_{L,0})^2 + (C_{D,0})^2 = 1$. The GBT buckling analysis code GBTUL [see current version in Bebiano, Camotim and Gonçalves (2018)] was employed to extract the "pure" buckling modes.

Figure 2.4 — Illustration of the geometrical imperfection modelling technique recommended by Dinis and Camotim (2010).
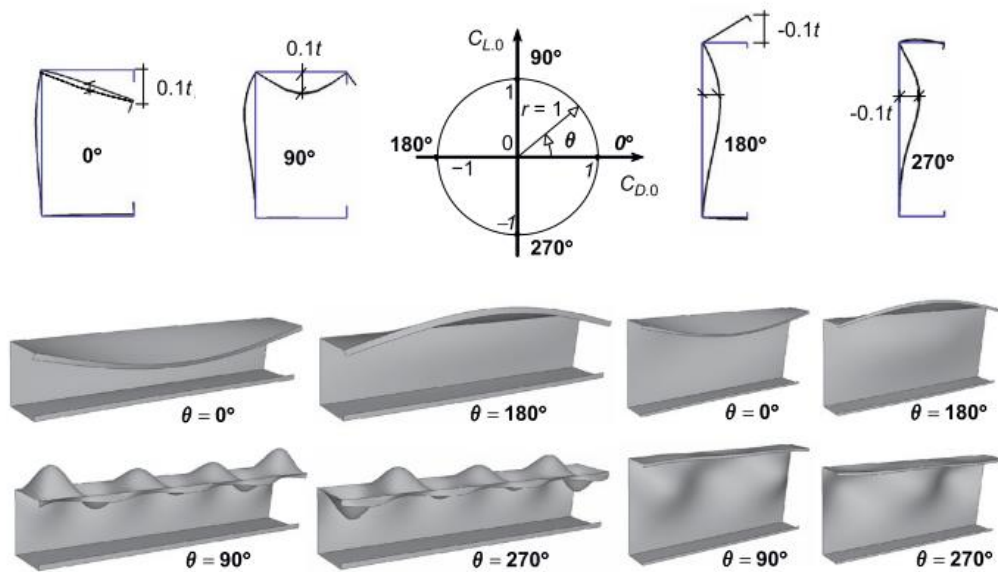
Source: adapted from Dinis and Camotim (2010)

2.2.2.3 Kyvelou, Gardner and Nethercot (2018)

Kyvelou, Gardner and Nethercot (2018) also combined local and distortional buckling modes to create the geometrical imperfection distribution in their finite element models. In their case, in turn, amplitudes for each "pure" mode were measured, obtaining approximately $0.1t$ and $0.3t$ for local and distortional geometrical imperfection shapes, respectively, as shown in Figure 2.5. The technique employed to determine these imperfection factors followed the procedure suggested by Schafer and

Peköz (1998b). Additionally, they used the finite strip software CUFSM 3.12 (SCHAFER; ÁDÁNY, 2006) to extract the "pure" local and distortional buckling mode shapes. Afterwards, these mode shapes were manually distributed along the member length and superposed in the finite element model. Sinusoidal functions with periods equal to the corresponding critical half-wavelengths obtained in the finite strip software were used to distribute the geometrical imperfection through the CFS member length.

Figure 2.5 — Cross-sectional view of (a) local and (b) distortional mode shapes employed in the study of Kyvelou, Gardner and Nethercot (2018).
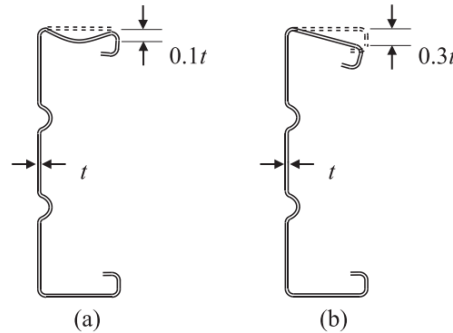
Source: (KYVELOU; GARDNER; NETHERCOT, 2018).

2.2.2.4 Matsubara, Batista and Salles (2019)

Matsubara, Batista and Salles (2019) used the classical approach to create the imperfection distribution in their finite element model, i.e., using the lowest buckling mode extracted by finite element buckling analysis. A magnitude factor of $0,1t$ was used to scale the normalised critical buckling mode shape.

2.2.2.5 Santos, Landesmann and Camotim (2019)

Santos, Landesmann and Camotim (2019) used different geometrical imperfection modelling techniques to validate their shell finite element models and to perform parametric studies.

Measures of the actual imperfection distribution along the member length was used to validate the finite element model. A detailed description of the numerical and experimental techniques used to model the imperfection distribution along the CFS member is found in Santos (2017). To put it briefly, seven displacement transducers (DT) were placed on the CFS cross-section to measure the imperfections along the specimen length (Figure 2.6a). Six parameters (Figure 2.6b) are then used to model the cross-sectional initial torsional rotation and displacements of the CFS member: torsional rotation (β), flange displacements (δ_{12}^{D} and δ_{76}^{D}), local web undulations (δ_{W}^{L})

and global minor and major initial displacements (δ_m^G and δ_M^G, respectively). Experimental and modelled geometrical imperfections were compared and showed reasonable agreement.

Figure 2.6 — Illustration of the (a) experimental instrumentation and (b) numerical parameters used to model geometrical imperfections in the study of Santos (2017).

(a)   (b)
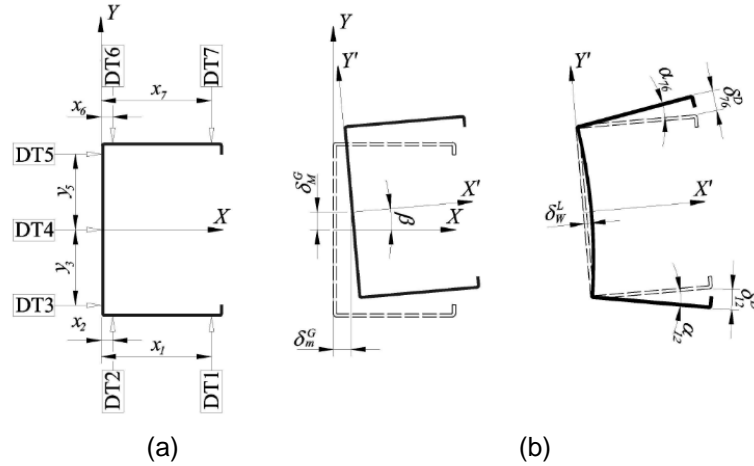
Source: (SANTOS, 2017).

The following relations were employed to calculate the initial torsional and displacements based on the DTs readings of CFS members with web width b_w and flange width b_f:

a) $\beta = \tan^{-1}\left[\dfrac{DT5-DT3}{y_5-y_3}\right]$

b) $DT3 = \delta_m^G + (y_3 - \delta_M^G)\tan\beta$

c) $DT6 = \delta_M^G + [(\cos\beta - 1)b_w]/2 + [x_6 + \delta_m^G + (b_w/2)]\tan\beta$

d) $\delta_M^G = \{DT6 + y_3\tan^2\beta - [x_3 + DT3 + (b_w/2)sen\beta]\tan\beta + (b_w/2)(1 - \cos\beta)\}/(1 + \tan^2\beta)$

e) $\delta_m^G = DT3 + (\delta_M^G - y_3)\tan\beta$

f) $\delta_W^L = [(DT3 - DT3)\delta_M^G + (\delta_m^G - DT4)y_3]/[(DT3 - DT4)sen\beta - y_3\cos\beta]$

g) $\delta_{12}^D = \begin{cases} b_f\sqrt{2(1 - \cos\alpha_{12})} \text{ if } DT1 \geq DT2 \\ -b_f\sqrt{2(1 - \cos\alpha_{12})} \text{ if } DT1 < DT2 \end{cases}$

h) $\delta_{76}^D = \begin{cases} b_f\sqrt{2(1 - \cos\alpha_{76})} \text{ if } DT7 \geq DT6 \\ -b_f\sqrt{2(1 - \cos\alpha_{76})} \text{ if } DT7 < DT6 \end{cases}$

i) $\alpha_{12} = \tan^{-1}\left|\dfrac{y_1' + \frac{b_w}{2}}{x_1'}\right|$ and $\alpha_{76} = \tan^{-1}\left|\dfrac{y_7' - \frac{b_w}{2}}{x_7'}\right|$

j) $(x_1', y_1') \equiv \begin{pmatrix} \cos\beta(x_1 - \delta_m^G) + sen\beta(-b_w/2 - DT1 - \delta_M^G), \\ -sen\beta(x_1 - \delta_m^G) + \cos\beta(-b_w/2 - DT1 - \delta_M^G) \end{pmatrix}$

k) $(x_7', y_7') \equiv \begin{pmatrix} cos\beta(x_7 - \delta_m^G) + sen\beta(b_w/2 + DT7 - \delta_M^G), \\ -sen\beta(x_7 - \delta_m^G) + cos\beta\left(\frac{b_w}{2} + DT7 - \delta_M^G\right) \end{pmatrix}$

In their parametric study, Santos, Landesmann and Camotim (2019) used the critical buckling mode extracted from shell finite element buckling analysis to model the initial imperfections. A sensitivity study was carried out to determine the amplitude factor for the imperfection shape. Magnitudes values were tested from recommendations reported by Landesmann and Camotim (2013), $0.1t$, Schafer and Peköz (1998b), $1,0t$, and a mean value taken from the measured readings, which was equal to $0,23t$. Failure load variation was below 5 per cent and, therefore, the average reading $0,23t$ was chosen as the amplitude factor in all parametric analyses.

2.2.2.6 Concluding remarks on geometrical imperfection

Table 2.4 shows a summary of geometrical imperfection models used in parametric studies of current researches on computational modelling of CFS. In all cases, imperfection shapes were assumed as buckling modes. Magnitude factors for local and distortional buckling modes were approximately between $0.1t$ and $0.75t$. For the study cases reviewed here, global buckling modes were not frequently included in the imperfection models. Additionally, three different numerical methods were used to perform the elastic stability analyses, FSM, GBT and FEM. Therefore, it can be observed that no consensus exists on geometric imperfection finite element modelling techniques for cold-formed steel members.

Table 2.4 — Summary of geometrical imperfection models used in parametric studies of current researches on computational modelling of CFS.

Source	Local	Distortional	Global	Elastic buckling analysis method
	Buckling mode amplitude			
Torabian, Zheng and Schafer (2014)	$0.31t$	$0.75t$	--	FSM
Martins, Camotim and Dinis (2017)	$0.1t$	--	--	GBT
Kyvelou, Gardner and Nethercot (2018)	$0.1t$	$0.3t$	--	FSM
Matsubara, Batista and Salles (2019)	$0.1t$ for the critical buckling mode			FEM
Santos, Landesmann and Camotim (2019)	$0.23t$ for the critical buckling mode			FEM

2.2.3 Material properties

2.2.3.1 Stress-strain relationships

According to Chen and Han (1988), the development of stress-strain relationships to describe the plastic deformation of structures under a complex stress state is the first step of plasticity theory. The graph in Figure 2.7 shows stress-strain curves obtained from tensile coupon tests of different metals. The graph shows that hot-rolled steel presents a stress-strain response linearly up to an upper yield point and back to a lower yield point, which extends infinitely. In contrast, cold-formed steel and stainless-steel exhibit a rounded stress-strain curve followed by strain hardening, or work hardening. For this reason, differently from hot-rolled steel, the yield stress for cold-formed steel is generally defined by an offset yield stress (σ_{ys}) that corresponds to a defined strain where initial yield stress occurs. It is common to adopt 0.2% proof stress ($\sigma_{0,2}$), as suggested by Schafer, Li and Moen (2010) and exemplified in Figure 2.7.

Moreover, for hot-rolled steel, an elastic perfectly-plastic material model (see Figure 2.8a) may satisfactorily represent its uniaxial tensile stress-strain behaviour. For cold-formed steel or stainless steel, instead, neglecting work hardening may lead to highly inaccurate results, as found by Rasmussen et al. (2003) and Lecce and Rasmussen (2006). In Chen and Han (1988), three alternative of simplified uniaxial tensile stress-strain curves with work hardening are presented: elastic-linear work-hardening model (Figure 2.8b), elastic-exponential hardening model (Figure 2.8c) and Ramberg-Osgood model (Figure 2.8d). The latter allows the rounding of the stress-strain portion of the material curve. For this reason, several researchers applied a distinct modification of the Ramberg-Osgood stress-strain relationship to represent tensile and compressive behaviour of CFS structural components.

Figure 2.7 — Stress-strain curves of typical metals used for steel structures.
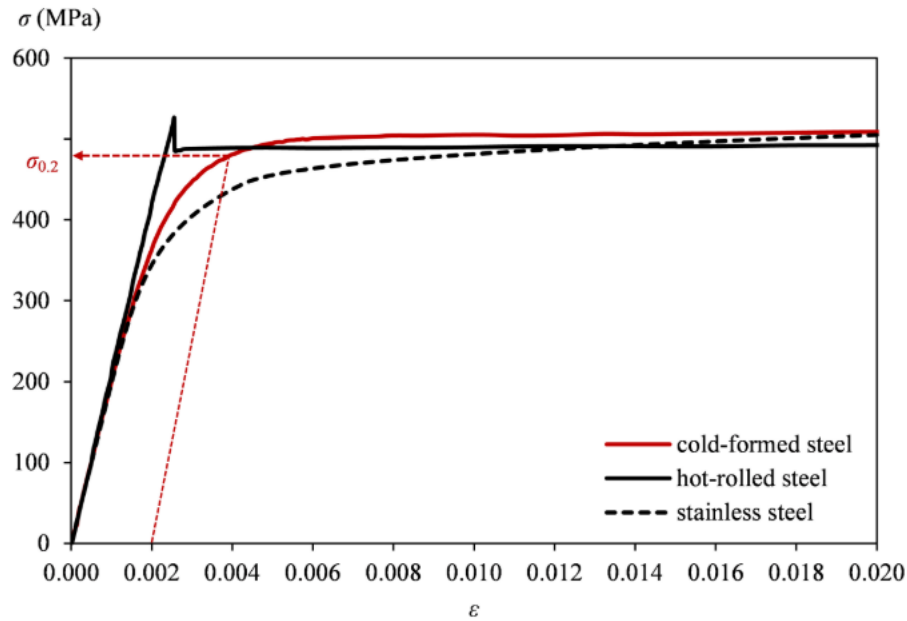
Source: (KYVELOU, 2017).

This formulation was initially proposed by Ramberg and Osgood (1943) for aluminium alloys and, afterwards, it was adapted for other nonlinear metallic materials by several authors [e.g., by Rasmussen (2003), Mirambell and Real (2000), Gardner and Ashraf (2006), Arrayago, Real and Gardner (2015), Gardner et al., (2016)]. The modification proposed by Gardner and Ashraf (2006) for stainless steel, which is described in Table 2.5, was also satisfactorily employed in the studies of Haidarali (2011), Haidarali and Nethercot (2011), Kyvelou, Gardner and Nethercot (2018) and Ye et al., (2016), that proposed finite element models for cold-formed steel structures. Haidarali and Nethercot (2011) and Ye et al., (2016), however, employed a straight line with a constant slope for stresses higher than 0.2% proof stress instead of using the Ramberg-Osgood curve again.

Table 2.5 — Modification of the Ramberg-Osgood stress-strain relationship proposed by (GARDNER; ASHRAF, 2006).

Stress interval	Stress-strain curve expression
For $\sigma \leq \sigma_{0,2}$:	$\epsilon_e = \dfrac{\sigma_e}{E} + 0,002 \left(\dfrac{\sigma_e}{\sigma_{0,2}}\right)^n$
for $\sigma_{0,2} < \sigma \leq \sigma_u$	$\epsilon_e = (\sigma_e - \sigma_{0,2})/E_{0,2} + \left[\epsilon_{1,0} - \epsilon_{0,2} - (\sigma_{1,0} - \sigma_{0,2})/E_{0,2}\right]\left[\dfrac{\sigma_e - \sigma_{0,2}}{\sigma_{1,0} - \sigma_{0,2}}\right]^{n'_{0,2,1,0}} + \epsilon_{0,2}$

Source: (GARDNER; ASHRAF, 2006).

In Table 2.5 σ_e and ϵ_e indicate the engineering stress and strain respectively, E the Young's modulus of the material, $\sigma_{0.2}$ and $\sigma_{1.0}$ the 0.2% and 1.0% proof stresses

respectively, $E_{0,2}$ the tangent modulus of the stress-strain curve at $\sigma_{0.2}$, $\epsilon_{0.2}$ and $\epsilon_{1.0}$ the total strain corresponding to the 0.2% and 1.0% proof stresses while n and $n'_{0.2,1.0}$ the strain hardening exponents to determine the degree of roundedness of the stress-strain curve.

Furthermore, it is common in researches dealing with CFS structures to model the material stress-strain curves with selected points from tensile coupon tests. For example, the researches of Yu and Schafer (2007), Torabian, Zheng and Schafer (2015), Maia et al. (2016) and (Santos, Landesmann and Camotim (2019).

Figure 2.8 — Examples of simplified uniaxial tensile stress-strain curves: (a) elastic perfectly-plastic model, (b) elastic-linear work-hardening model, (c) elastic-exponential hardening model and (d) Ramberg-Osgood model.
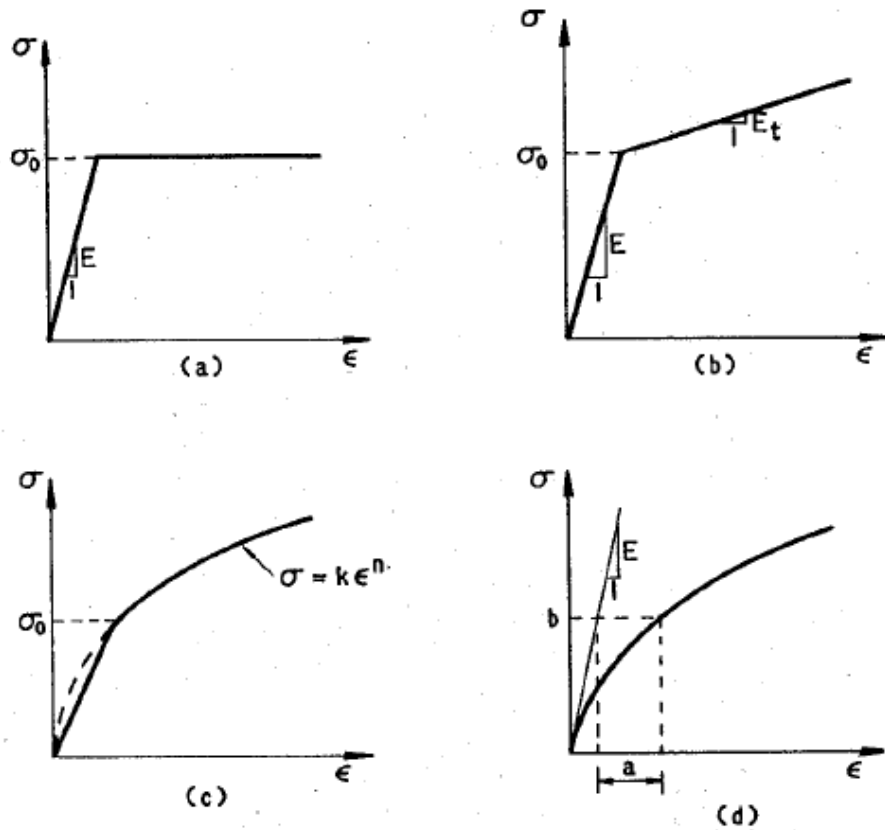
Source: (CHEN; HAN, 1988).

Finally, when modelling the material stress-strain curve for numerical analyses, true (Cauchy) stress-strain values must be specified, mainly when ultimate capacity and post-buckling behaviour are investigated. Thus, tensile coupon tests results (engineering stress-strain) need to be converted to true (Cauchy) stress-strain curves, as follows:

$$\sigma_t = \sigma_e(1 + \epsilon_e)$$

$$\epsilon_t = \ln(1 + \epsilon_e)$$

where σ_t and ϵ_t correspond to true stress and strain and σ_e and ϵ_e to engineering stress-strain values.

2.2.3.2 Yield and failure criteria

In the literature, the three main components commonly used to generalise the uniaxial behaviour of a material into a combined stress state are: (1) yield condition, that describes the combination of stresses that leads the material to yielding; (2) flow rule (associative or non-associative plasticity), that gives a mathematical description for plastic deformation; and, (3) hardening rule, that gives the description of evolution of yield surface with plastic strain. Hence, this section briefly presents how these three aspects are frequently adopted in the finite element models of the studies reviewed here.

Recently, the most widely used yield criterion and plastic flow rule for cold-formed steel are respectively the von Mises yield criterion with associated flow rule. As example, the researches of Martins, Camotim and Dinis (2017) and Santos, Landesmann and Camotim (2019). Chen and Han (1988), in contrast, affirm that the yield criterion of Tresca and von Mises model, both with associated flow rule, can achieve accurate agreement with experimental tests for metals.

Furthermore, according to Chen and Han (1988). isotropic and kinematic hardening are the most appropriate rules for describing the material during the process of plastic flow. In the last decades, the isotropic hardening has been the most employed hardening rule in researches of CFS members, such as in Yu and Schafer (2007), Torabian, Zheng and Schafer (2014), Maia et al. (2016), and others. However, it cannot account for the Bauschinger effect exhibited by most structural materials, which refers to a reduction in the material resistance when subjected to reversed loading. The plastic deformations during the manufacturing process may induce the Bauschinger effect, for example. The kinematic hardening rule, however, has a more complex implementation, but can account for this effect. Thus, the material hardening rule must be carefully selected. Moen, Igusa and Schafer (2008) suggest the use of kinematic rule when residual stresses are considered, otherwise, the isotropic hardening rule should be employed since its application is simpler.

2.2.3.3 Corner strength enhancements

During the manufacturing process, the plastic deformation induced in cold-formed steel members, mainly in the corners of a section, leads to different mechanical properties along the cross-section. In various experiments, considerable strength enhancement is observed in the corner regions when compared to flat ones [e.g. in Kyvelou (2017) and Ye et al. (2018)]. Figure 2.9 shows a comparative study between corner and flat tensile coupon tests conducted by Kyvelou (2017), in which an average strength enhancement of 17% was found in the corner region.

However, some researches, such as Narayanan and Mahendran (2003) and Young (2004), ignored corners strength enhancements due to the small proportion of area between corner regions and the whole cross-sectional area. Nonetheless, good agreement with experimental data was observed. Additionally, other researchers also found satisfactory numerical results in the collapse analysis of CFS members neglecting the corner strength effects, such as Haidarali (2011), Landesmann and Camotim (2013) and Santos, Landesmann and Camotim (2019). Generally, corner strength is ignored assuming that its effect is offset by the effects of residual stresses, as explained in the subsequent section (see Section 2.2.4).

2.2.3.4 Concluding remarks on material properties

Table 2.6 summarises the material models adopted in recent researches that developed a shell finite element model to verify the strength of CFS members. At first glance, it seems that von Mises yield criterion with associative flow rule and isotropic hardening are the most used plasticity parameters. However, considering the total amount of studies conducted on the subject, the number of researches reviewed herein should not be taken as a representative sample for this generalization. Moen, Igusa and Schafer (2008), for instance, present situations in which kinematic hardening rule provides conservative strength results and must be used. To this end, they provided guidelines for the implementation of the kinematic hardening rule. Concerning the stress-strain curve, no consensus was found amongst the researches reviewed here to determine which technique is the most suitable to represent the cold-formed steel material. Therefore, in this research two different stress-strain modelling techniques will be used to assess the sensitivity of the finite element model to this parameter: (i) elastic perfectly-plastic model and (ii) two-stage Ramberg-Osgood model .

Figure 2.9 — Comparison between corner and flat tensile coupon tests.
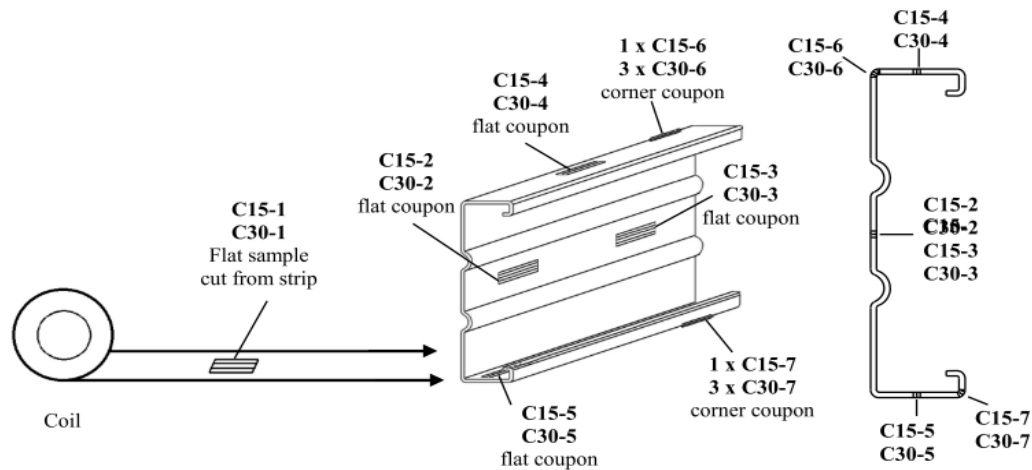
(a) Position of extracted coupon specimens
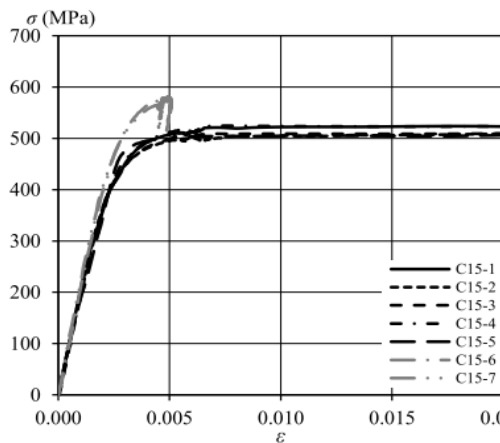
(b) Results for specimens of 1,5 mm thickness
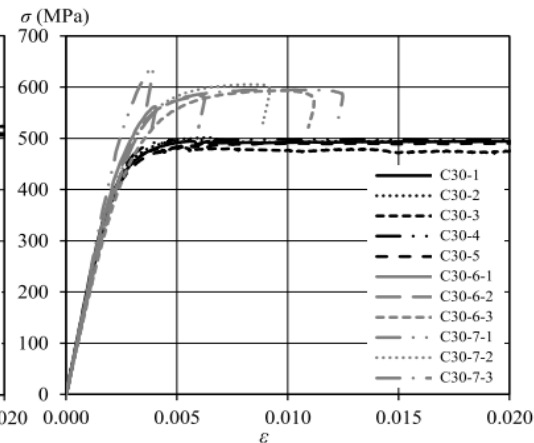
(c) Results for specimens of 3,0 mm thickness

Source: (KYVELOU, 2017).

Table 2.6 — Summary of material models used in the parametric study of recent researches on computational modelling of CFS.

Source	Material properties			
	Yield criterion	Flow rule	Hardening rule	Stress-strain curve
Torabian, Zheng and Schafer (2014)	von Mises criterion	Associative plasticity	Isotropic hardening	Multilinear model from coupon tests.
Martins, Camotim and Dinis (2017)	von Mises criterion	Associative plasticity	Isotropic hardening	Elastic perfectly-plastic model
Kyvelou, Gardner and Nethercot (2018)		Not specified		The two-stage Ramberg-Osgood
Matsubara, Batista and Salles (2019)	von Mises criterion	Not specified		Bilinear elastoplastic material model
Santos, Landesmann and Camotim (2019)	von Mises criterion	Associative plasticity	Isotropic hardening	Elastic perfectly-plastic model

2.2.4 Residual stresses

According to Amouzegar, Schafer and Tootkaboni (2016), the distribution of residual stresses and strains (denominated only as residual stresses in this research) along the cross-section of CFS members are usually derived from manufacturing processes — such as coiling, uncoiling, flattening and cold-forming of the cross section (Figure 2.10). Hence, including residual stresses in finite element models is an evolving procedure since it is necessary to follow the manufacturing process step by step to predict such stresses, as shown in Amouzegar, Schafer and Tootkaboni (2016).

This laborious procedure may be a potential challenge for numerical analyses that focus exclusively on predicting the collapse behaviour of steel members. In contrast, several recent researches reached satisfactory results in finite element analysis of CFS members without considering residual stresses, such as Anbarasu (2016), Kyvelou, Gardner and Nethercot (2018) and Santos, Landesmann and Camotim (2019). Additionally, a parametric study conducted by Amouzegar, Schafer and Tootkaboni (2016) indicates that the maximum residual stresses are almost zero for sheets with thicknesses smaller than one millimetre (as the CFS members studied herein). For this reason, in this research the representation of the effects of residual stresses are neglected in future finite element analyses. However, in what follows, a brief overview on residual stresses for cold-formed steel is given.

Figure 2.10 — Manufacturing processes of cold-formed steel members.
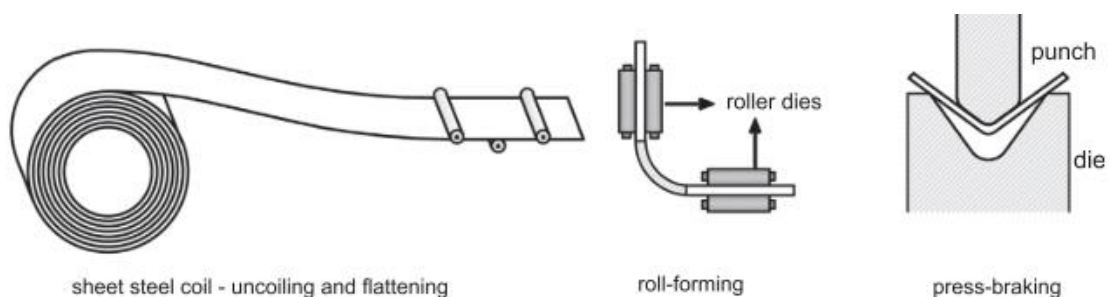
Source: (AMOUZEGAR; SCHAFER; TOOTKABONI, 2016).

An extensive literature review of available analytical expressions for predicting residual stresses in steel members is conducted by Abambres and Quach (2016). General methods are given in Moen, Igusa and Schafer (2008) and Amouzegar, Schafer and Tootkaboni (2016).

Briefly, according to Schafer and Peköz (1998b), residual stresses in CFS

sections consist of two fundamental components, the flexural component and the membrane component, as shown in Figure 2.11.

Figure 2.11 — Definition of flexural and membrane residual stresses.
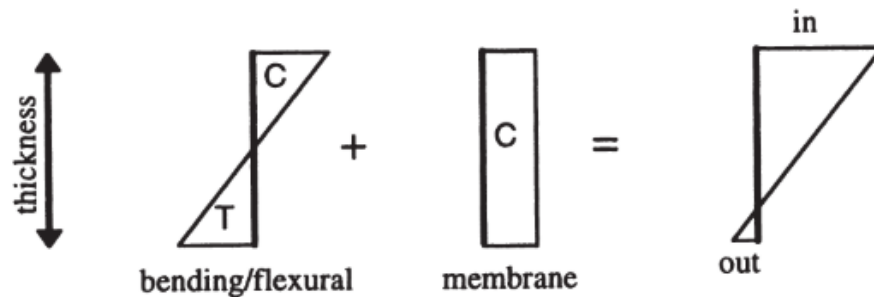
Source: (SCHAFER; PEKÖZ, 1998b).

In the last decades, several authors measured these different components of residual stresses in CFS members, such as Ingvarsson (1975), Dat and Peköz (1980) and Batista and Rodrigues (1992). Schafer and Peköz (1998b) and Moen, Igusa and Schafer (2008) analysed several available measured data on residual stresses and concluded that membrane stress magnitudes are small when compared to the bending counterpart. Experimental data on membrane stress magnitudes indicates that they are more prevalent in roll-formed members than press-braked members, and are higher in section corners (SCHAFER; PEKÖZ, 1998b).

In numerical models, the membrane stresses are commonly ignored due to either low magnitudes [e.g. Young (2004) and Young and Rasmussen (1998)] or an offset by the corner strength effect (see section 2.2.3.3). Schafer, Li and Moen (2010) affirm that increases in the yield stress due to the cold-work of forming in corner regions derive from the same process of residual stresses. Therefore, it is common to implicitly consider that these effects counterbalance one another so that their magnitudes can be taken as null in numerical models.

Schafer and Peköz (1998b) observed high magnitudes of the flexural residual stress component in the available experimental data on CFS members. However, Jandera, Gardner and Machacek (2008) indicated that bending residual stresses should not be inserted in numerical simulations when stress-strain curves obtained from tensile coupon tests extracted from CFS members are included. They found that these residual stresses have influence on the material stress–strain curve, since their research results indicate that the secant modulus is reduced in the presence of residual

stresses while the tangent modulus increases in some regions of the stress–strain curve. Further, Schafer, Li and Moen (2010) state that a complete characterization of residual stresses must include other effects from the manufacturing process [see Amouzegar, Schafer and Tootkaboni (2016) for a detailed description of said effects], otherwise the initial conditions of the model would not reflect the real member.

Table 2.7 summarises the considerations upon the residual stress' models used in current researches on computational modelling of CFS. Among the researches reviewed here, residual stress effects are commonly ignored.

Table 2.7 — Summary of residual stresses models used in current researches on computational modelling of CFS.

Source	Residual stress model
Torabian, Zheng and Schafer (2014)	Residual stress and effective plastic strain distribution modelled according to Moen et al. (2008) only in the corner regions.
Martins, Camotim and Dinis (2017)	Not mentioned
Kyvelou, Gardner and Nethercot (2018)	Ignored due to recommendations of Jandera, Gardner and Machacek (2008)
Matsubara, Batista and Salles (2019)	Not mentioned
Santos, Landesmann and Camotim (2019)	Ignored due to recommendations of Young and Budynas (2002) and Ellobody and Young (2005)

2.2.5 Element selection

In the modelling of thin-walled structures, in which thickness is much smaller than other dimensions, shell elements are generally employed. On the other hand, solid elements or solid-shell elements, as available in some finite element packages, are also capable of accurately modelling these structures. In this research, however, only shell elements are used to discretize finite element models of CFS structures, and, for this reason, this section focuses only on this element type.

Employment of shell elements must account for several parameters, such as: the element order (linear or quadratic shape functions), the shell theory implemented (e.g. Kirchhoff for thin plates and Reissner–Mindlin for thick plates), the integration scheme (full or reduced integration, for example) and the number of integration points through the thickness. Firstly, in the literature reviewed here, linear shell elements are the most widely used to model CFS structures ((Yu and Schafer (2007), Anbarasu (2016), Kumar and Sahoo (2016), Maia et al. (2016), Martins, Camotim and Dinis (2017), Kyvelou, Gardner and Nethercot (2018), Matsubara, Batista and Salles (2019)

and Santos, Landesmann and Camotim (2019). Further, most of these studies employ the reduced integration scheme, which prevents shell finite element models from "shear locking", as discussed in Zienkiewicz and Taylor (2005) and Liu and Quek (2013). According to these authors, this phenomenon occurs for shell models under bending and using Reissner–Mindlin theory with high length-to-thickness ratio, which increases the element stiffness, consequently leading to erroneous results. Lastly, Schafer, Li and Moen (2010) state that a high number of integration points through thickness must be used when residual stresses are included and/or to decrease the sensitivity of the model to the beginning of yield. Table 2.8 displays a summary of the element type used in the researches reviewed here.

Table 2.8 — Summary of element type used by current researches on computational modelling of CFS.

Source	Element type
Torabian, Zheng and Schafer (2014)	9-node shell with reduced integration (S9R5 Abaqus element)
Martins, Camotim and Dinis (2017)	4-node shell (S4 Abaqus element)
Kyvelou, Gardner and Nethercot (2018)	4-node shell with reduced integration (S4R Abaqus integration)
Matsubara, Batista and Salles (2019)	4-node shell (SHELL181 Ansys element)
Santos, Landesmann and Camotim (2019)	4-node shell (SHELL181 Ansys element)

2.2.6 Solution schemes

The collapse and strength behaviour of structures is commonly described by a nonlinear load *versus* displacement relationship, which requires a nonlinear structural analysis. In finite element analysis, structural nonlinearities are generally classified as geometric nonlinearity, material nonlinearity and contact or boundary nonlinearity. The solution of such nonlinearities is usually achieved through an incremental approach. Several computational algorithms coupled with incremental load or displacement control are available in the literature to deal with nonlinear problems iteratively, such as full Newton-Raphson method, modified Newton-Raphson method and quasi-Newton method (CRISFIELD, 1991).

However, nonlinear collapse analyses of cold-formed steel profiles may pose issues of convergence, requiring the application of special nonlinear techniques (SCHAFER; LI; MOEN, 2010). ANSYS® (software employed in this research) theory manual (ANSYS® 2020R1) recommends its users to apply the arc-length method

(modified Riks) or a nonlinear stabilisation (artificial damping) when the structure becomes unstable. The arc-length method can reproduce non-monotonic equilibrium paths by circumventing global instabilities. For local instabilities, in turn, global solution methods may fail. This class of problems is usually solved either by dynamic analysis or artificial damping, as stated by Quach (2005). The nonlinear stabilisation algorithm uses an artificial damping to reduce the displacements at each degree-of-freedom of the elements that presents an instability problem.

Table 2.9 shows the solution schemes adopted in the researches reviewed here. Modified Riks method (arc-length method) is employed in most cases. However, the employment of the stabilisation method is also observed, such as in Haidarali (2011), Hui (2014), Kyvelou, Gardner and Nethercot (2018).

Table 2.9 — Summary of solution schemes employed by current researches on computational modelling of CFS.

Source	Solution scheme
Torabian, Zheng and Schafer (2014)	Modified Riks method
Martins, Camotim and Dinis (2017)	Not mentioned
Kyvelou, Gardner and Nethercot (2018)	Adaptive automatic stabilisation scheme
Matsubara, Batista and Salles (2019)	Modified Riks method
Santos, Landesmann and Camotim (2019)	Newton-Raphson's method with an arc-length control strategy

2.2.7 Existing investigations on the behaviour of cold-formed steel structures under minor-axis bending

The increasing use of cold-formed steel profiles as structural elements is mainly due to their versatility of application, a consequence of good weight/resistance ratio and high ductility, which in turn allows the fabrication of numerous profile shapes (JAVARONI, 2015). Amongst the commonly used shapes, "U" and stiffened "U" sections, e.g. lipped channel sections, are commonly employed as elements under flexure, especially about the major axis of inertia. A considerable number of academic studies focused on the mechanical behaviour of "U" and stiffened "U" CFS profiles subjected to major axis bending is found in the literature. For instance, the works conducted by (Anbarasu, 2016), Martins, Camotim and Dinis (2017), (Martins et al. (2018), Laím, Rodrigues and Silva (2013), Kankanamge and Mahendran (2012), Obst, Kurpisz and Paczos (2016), Matsubara, Batista and Salles (2019), Santos, Landesmann and Camotim (2019), and others. In contrast, studies concerning the

behaviour of the aforementioned types of CFS profiles under minor axis bending are scarce (YUAN, 2013), but nevertheless observed in academic literature.

Yuan (2013) proposed an analytical formulation, based on the geometric nonlinear Brazier approach, for nonlinear stability analysis of CFS "U" profiles subjected to minor axis pure bending (web compression). The author states that when a channel section beam is subjected to a load parallel to its principal axis, Brazier type of flattening deformation may occur, which can lead to nonlinear snap-through instability. This nonlinear bending response was first investigated by Brazier (1927), thus it is called Brazier effect or Brazier flattening. Figure 2.12 shows the effect of Brazier in a thin angle-section bent under its weak axis.

Figure 2.12 — Brazier effect of thin angle-section beam under minor axis bending.

Brazier effect
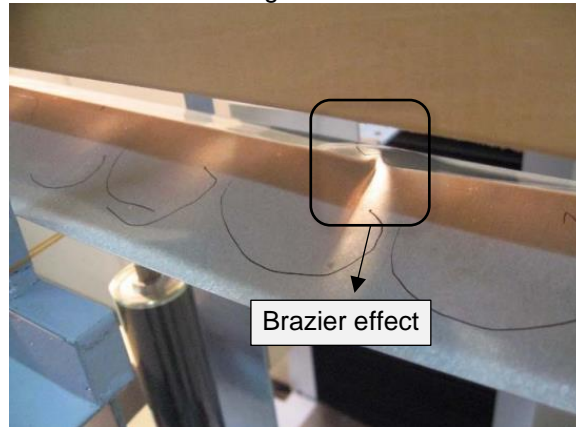
Source: (ZHOU et al., 2018).

In order to validate the proposed formulation, Yuan (2013) performed a finite element analysis with the software ANSYS (Figure 2.13a). However, the finite element method provided slightly stiffer solutions than the presented analytical method. This deviation was then explained by the effect of beam length employed in the finite element analysis, which was not considered in the analytical model. For this reason, in a subsequent work, Yuan and Chen (2015) proposed a new formulation with the inclusion of the beam length, besides the beam cross-sectional dimensions. The authors then observed better agreement with the modified approach, as shown in Figure 2.13b.

Torabian, Zheng and Schafer (2014) conducted a numerical and experimental study of stiffened "U" section profiles under combined influence of bending and compression (This research is expanded by Torabian, Zheng and Schafer (2015) by the inclusion of experimental tests of two additional member lengths, 61 cm and 122

cm. Both studies indicate that, in comparison with test results, standardized equations are overly simplistic and conservative.

Kumar and Sahoo (2016) calculated the moment capacity of multiple "U" and stiffened "U" CFS profile sections by means of standardized design equations and compared the results with a Finite Element Analysis performed with ABAQUS. For validation, the numerical results are compared with the behaviour of selected profile sections, subjected to four-point flexure experiments about the minor axis of inertia (Figure 2.15). The last step of the research consisted of an applicability analysis of the standardized equations as function of width-to-thickness ratio, lip lengths and depth-to-width ratio of CFS profiles under minor axis bending, using the numerical results as a reference point.

Figure 2.14). Experiments were conducted on seventeen 30,5 cm CFS profile specimens subjected to compression and multiple bending moment orientations, including minor axis bending. The research also presents a parametric numerical analysis using the software ABAQUS. In general, the numerical results are validated by the experiments and compared with limit state design (LSD) equations prescribed in the pertinent North American standard.

Figure 2.13 — Numerical study conducted by Yuan (2013) and Yuan and Chen (2015).

(a) Finite element model
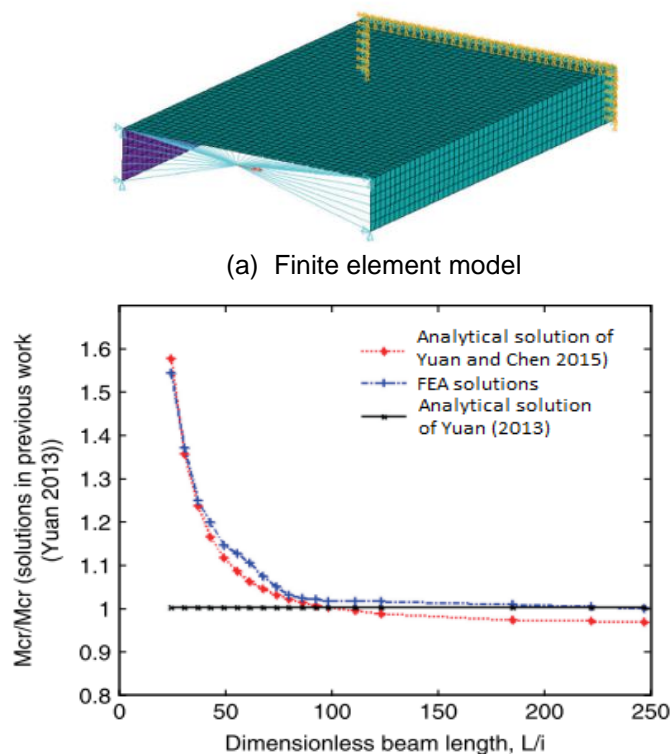
(b) Comparison of critical moment versus slenderness ratio between finite element analyses and analytical formulations proposed by Yuan (2013) and Yuan and Chen (2015).

Source: (YUAN, 2013) and (YUAN; CHEN, 2015).

This research is expanded by Torabian, Zheng and Schafer (2015) by the inclusion of experimental tests of two additional member lengths, 61 cm and 122 cm. Both studies indicate that, in comparison with test results, standardized equations are overly simplistic and conservative.

Kumar and Sahoo (2016) calculated the moment capacity of multiple "U" and stiffened "U" CFS profile sections by means of standardized design equations and compared the results with a Finite Element Analysis performed with ABAQUS. For validation, the numerical results are compared with the behaviour of selected profile sections, subjected to four-point flexure experiments about the minor axis of inertia (Figure 2.15). The last step of the research consisted of an applicability analysis of the standardized equations as function of width-to-thickness ratio, lip lengths and depth-to-width ratio of CFS profiles under minor axis bending, using the numerical results as a reference point.

Figure 2.14 — Numerical and experimental conducted by Torabian, Zheng and Schafer (2014): geometric and boundary condition assumptions.
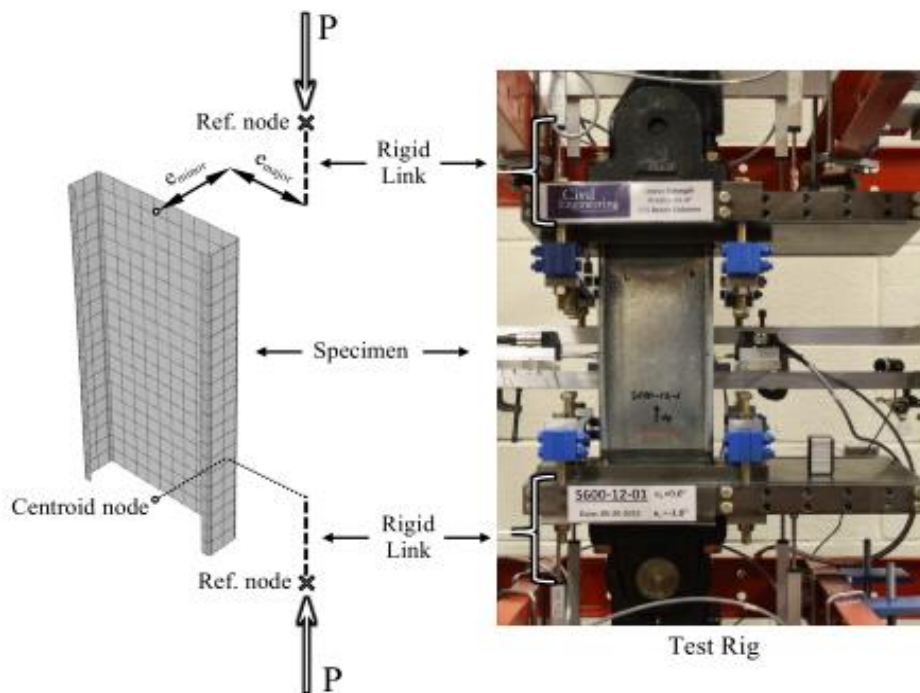
Source: (TORABIAN; ZHENG; SCHAFER, 2014).

Figure 2.15 — Numerical and experimental study conducted by Kumar and Sahoo (2016): comparison of modes of failure for lipped channel sections (a) Test, (b) Prediction.
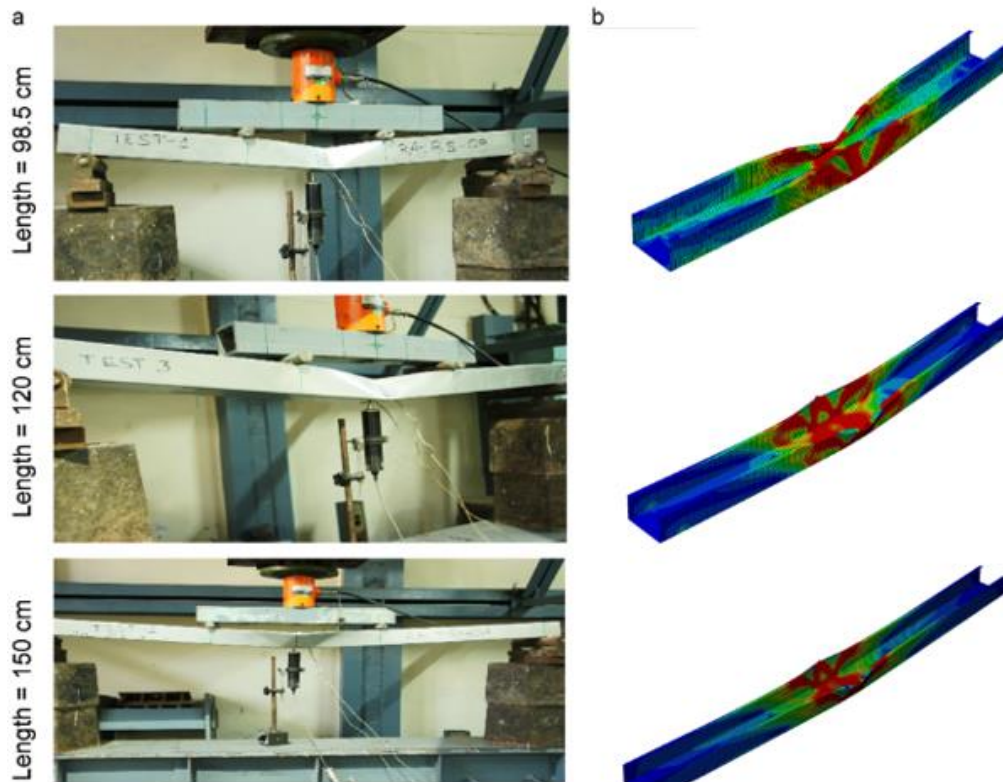
Source: (KUMAR; SAHOO, 2016).

In Favarato et al. (2019a), an investigation was conducted regarding the determination of critical elastic moment for lateral-torsional buckling by the analytical formulae prescribed in the Brazilian design code ABNT NBR 14762:2010, given by Equation (2.4). Several linear shell finite element analyses are performed for different length and number of spans for continuous beams under minor axis bending, as shown in Figure 2.16. Divergence was found between the Brazilian design code and the finite element results when the stiffeners are tensioned.

Figure 2.16 — Representation of the parametric study conducted by Favarato et al. (2019a).

(a) Two-span continnuous beam under bending.

(b) Three-span continnuous beam under bending.
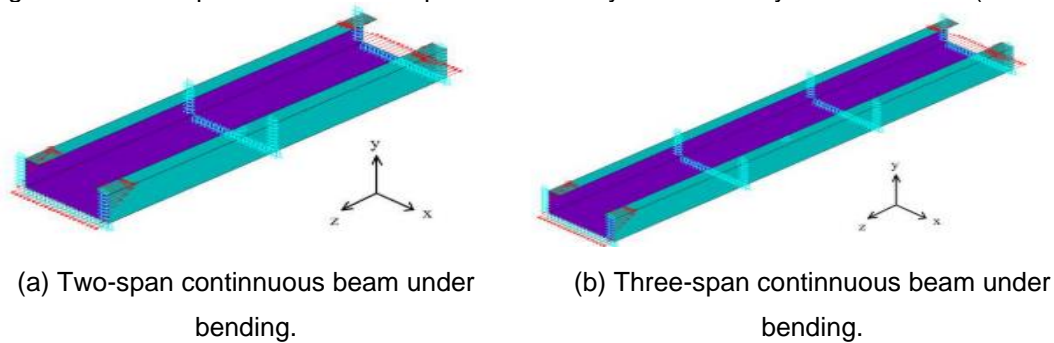
Source: (FAVARATO et al., 2019a).

2.3   Researches on lattice reinforcements

2.3.1   Introduction

Lattice reinforcement (Figure 2.17a), or truss reinforcement, is a common solution for floor systems in the construction industry. They are typically applied in the manufacture of lattice girders (Figure 2.17b), Trelifácil® solution (Figure 2.17c) or lattice girder planks (Figure 2.17d). This type of steel reinforcement consists of two bottom main chords, two diagonal main chords and one top main chord welded together (a). According to Gaspar (1997), the top bar is responsible for the maximum propping distance during the construction phase and the diagonal bars to provide shear resistance and to ensure that the system is monolithic after concrete curing. Droppa Jr. (1999) states that the diagonal bars offer good conditions of shipping and handling to the set and the bottom chords provide tensile resistance when the system is under bending. Therefore, all members of this steel reinforcement system play a role in the entire configuration.

Commercially, different types of lattice reinforcements are found around the world. In this research, the lattice reinforcements are fabricated according to ABNT NBR 14859-3:2017, using CA 60 steel, which has characteristic yielding stress of 600 MPa (ABNT NBR 7480:2007). Figure 2.18 illustrates the configuration of lattice reinforcements and Table 2.10 presents their geometrical dimensions available for commercial purposes. The lattice reinforcements are indicated by a code TR, followed by four parameters: the first one represents the height of the truss reinforcement, in centimetres, and the last three represent the diameters, in millimetres, of the top chord, the diagonals and the bottom chords respectively, without consideration of decimal places.

Figure 2.17 — Employment of lattice reinforcement in the construction industry.

(a) Steel lattice reinforcement

(b) Lattice joists

(c) Trelifácil® solution

(d) Lattice girders planks
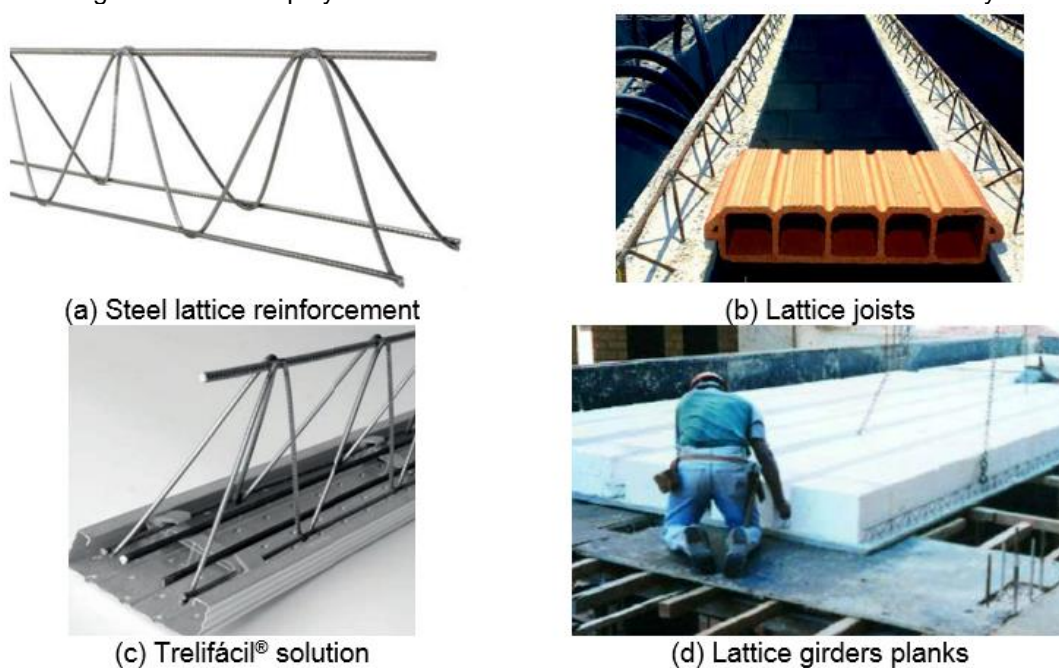
Source: (ArcelorMittal, 2017a).

Figure 2.18 — Lattice girder configurations.

(a) Perspective view

(b) Cross-sectional view
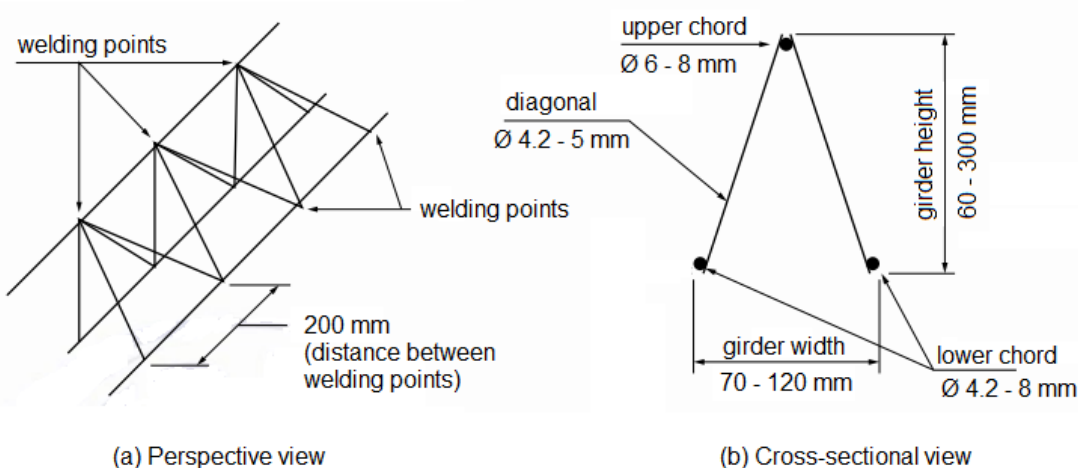
Source: adapted from ABNT NBR 14859-3:2017.

Table 2.10 — Lattice girder dimensions.

Lattice Girder Specification	Height (mm)	Upper chord (mm)	Diagonal (mm)	Lower chord (mm)
TR 8644	80	6	4.2	4.2
TR 8645	80	6	4.2	5
TR 12645	120	6	4.2	5
TR 12646	120	6	4.2	6
TR 16745	160	7	4.2	5
TR 16746	160	7	4.2	6
TR 20745	200	7	4.2	5
TR 20756	200	7	5	6
TR 25856	250	8	5	6
TR 25858	250	8	5	8
TR 30856	300	8	5	6
TR 30858	300	8	5	8

Source: (ARCELORMITTAL, 2017a).

2.3.2 *Existing investigations on the behaviour of lattice reinforcements*

In the last years, most researches on the behaviour of lattice reinforcements were conducted when they are applied to precast concrete slabs with lattice girders. An extensive literature review about the background of these slabs is carried out by Carvalho et al. (2005). In this study, they aimed to present the theoretical and experimental studies on precast slabs with lattice girders from that time. According to their findings, researches, such as Caixeta (1998), appointed that excessive deformation governs the design of these slabs. Additionally, they stated the importance of analysing the propping support distance during construction phase.

Due to the importance of the propping supporting distance for lattice girders, several authors dedicated their studies to investigate this subject. As stated by Carvalho et al. (2005), Gaspar (1997) is the pioneer to provide a design procedure to verify the propping distance. After that, other studies were conducted and even a computational program to determine the propping supporting distance (the program "PUMA ARMAÇÃO TRELIÇADA" [s.d.] developed by the Eng. Alonso Droppa in 2003) was developed, according to Carvalho et al. (2005). In 2013, Sartorti, Fontes and Pinheiro (2013) conducted an experimental study in order to determine the spacing between propping lines of lattice joist slabs. During their tests, the following ultimate limit states (ULS) were observed: buckling of the upper chord under the effect of positive bending moment (so-called sagging bending moment) (Figure 2.19a); failure of the weld in a node due to shear (Figure 2.19b); and buckling of the diagonals also due to shear (Figure 2.19c). Then, they developed formulations to calculate the propping support distances based on these ULS and the serviceability limit state of deflection.

Figure 2.19 — Failure modes of lattice girders under sagging bending moment tests.
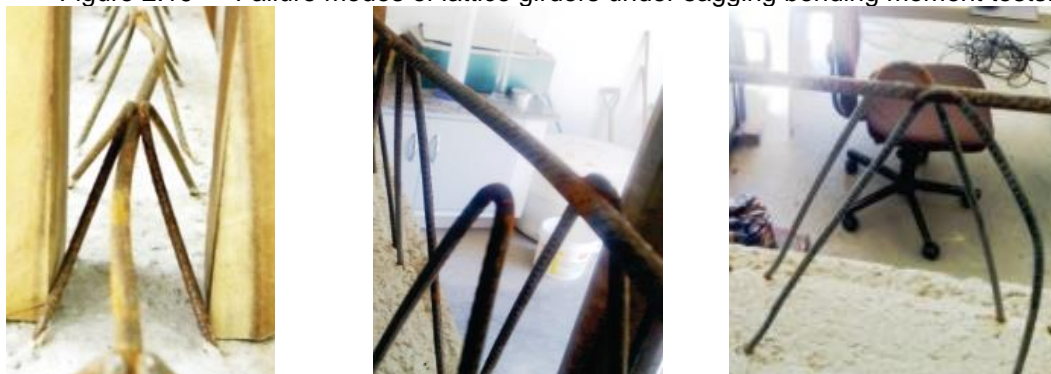
(a) Upper chord buckling   (b) Weld rupture   (c) Diagonals buckling

Source: (SARTORTI; FONTES; PINHEIRO, 2013).

More recently, studies on the behaviour of lattice girders slabs attempted to optimize the propping support distance and its design methods. Storch et al. (2017), for example, conducted a theoretical and experimental study on the behaviour of lattice girders slabs under negative bending (also referred as hogging bending moment). Figure 2.20 shows the failure modes found in their tests. In general, their results appointed that lattice girders shall be recommended when less propping is needed. Ferreira, de Lima and Delalibera (2017) performed a structural optimization of slabs formed by lattice girders with and without prestressing. Their results showed that the maximum span for the design of slabs without prestressing is 9 m and with the use of prestressed joist this limit increases to around 15 m.

Figure 2.20 — Failure modes of lattice girders under hogging bending moment tests.

(a) Diagonal chords buckling   (b) Lower chords buckling

Source: (STORCH et al., 2017).

3 DEVELOPMENT OF THE FINITE ELEMENT MODELS

3.1 Introduction

This chapter describes the basic features used to develop finite element numerical models using the computer program ANSYS® Academic Research Release 2020R1 (ANSYS® 2020R1) to study the flexural behaviour of the Trelifácil® solution.

First of all, the finite element method is a powerful and well-known numerical technique for solving partial differential equations in a variety of practical problems. Based on this method, John Swanson developed the commercial general-purpose software called ANSYS®, which was first released in 1970 (THOMPSON; THOMPSON, 2017). Therefore, the choice of this software to develop the numerical models of this research is justified by its satisfactorily employment in other several studies dealing with nonlinear structural analysis, such as: Dubina and Ungureanu (2002), Vieira Junior (2007), Bonada et al., (2012), Matsubara, Batista and Salles (2019), Santos, Landesmann and Camotim (2019) and Degtyarev (2020).

This research aims to develop finite element models to predict the flexural behaviour of the Trelifácil® solution with and without the trussed girder. Therefore, the first step was to choose an appropriate setup to subject the beams to bending. Figure 3.1 shows three possible ways for providing constant moment distribution in a beam without the presence of shear stresses (i.e., pure bending). Due to practical reasons for the experimental tests, four-point bending was applied in the finite element models to predict their flexural behaviour.

The basic features of two finite element models developed to the Trelifácil® solution without and with the trussed girder, namely specimen type 1 and specimen type 2, respectively, are presented in the subsequent sections. The first one, which models only the CFS member, is evaluated through a series of sensitivity analyses. The results obtained are compared with measured data obtained from the pilot experiment performed by Gomes et al. (2019), used as basis for the design of the physical tests conducted by Candido (2020, in progress). For the complete configuration of the Trelifácil® solution, a proposal of finite element model is presented with the objective of supporting the design of an experimental program by investigating the most relevant parameters that may affect its structural behaviour.

Figure 3.1 — Illustration of three different ways for providing constant moment distribution in a structural member.

M M

$+$ $\qquad M_{max} = M$

(a) Imposed bending moment

P $\qquad a$ $\qquad a$ $\qquad P$

$+$ $\qquad M_{max} = Pa$

(b) Beam with hanging

P $\qquad P$

a $\qquad a$

$+$ $\qquad M_{max} = Pa$

(c) Four-point bending

Source: author's own.
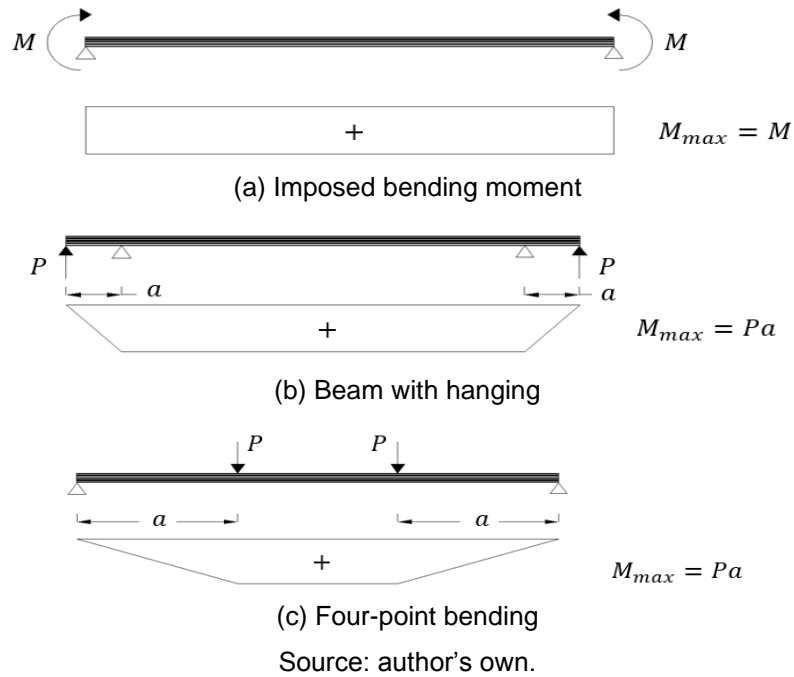
3.2 Finite element model of specimen type 1

According to Schafer, Li and Moen (2010) a finite element model for computational prediction of the ultimate strength and collapse behaviour of cold-formed steel is sensitive to: "solvers, element choice and discretization, boundary conditions, material models, initial imperfections, initial residual stresses and strains". Hence, a sensitivity study has been conducted for each of these input parameters, with the exception of initial residual stresses. As stated by Schafer, Li and Moen (2010), considering residual stresses without including the cold-work effects may lead to erroneous results, since both arise from the manufacturing process. As such, it is common practice to assume that these effects cancel each other and, for this reason, both parameters are ignored in the numerical analyses developed herein. The details of the finite element models are discussed in the following sections. Also, theoretical predictions using the Direct Strength Method are presented.

3.2.1 Finite element modelling of a pilot experiment conducted by Gomes et al. (2019)

3.2.1.1 Testing program

A total of six four-point bending tests about the minor axis of inertia (lips under

compression) were conducted on cold-formed steel members used in the Trelifácil®
solution. Nominal dimensions of the specimens' cross-section are shown in Figure 1.9.
The overall experimental layout and the employed instrumentation for all beam tests
are illustrated in Figure 3.2 and Figure 3.3, respectively. Three specimens were simply
supported on rollers across a 0.5 m span and the remainder with a free span of 0.90
m, both with a 50 mm overhanging length from each support. A spreader plate was
used to apply load from an EMIC hydraulic press at a constant rate of 0.04 mm/s until
failure. At the supports and loading points, where the beams were subjected to high
concentrated forces, the cross-sections were locally reinforced with wooden blocks
(dimensions are shown in Figure 3.4). These wooden blocks were also used to ensure
that load contact occurred at the web of the specimen. Two linear variable
displacement transducers (LVDTs) registered vertical deflection values at mid-span.
Load and displacement measurements were recorded using ADS2000 data acquisition
system at 0.2 s intervals.

Figure 3.2 — Experimental layout of four-point bending tests.
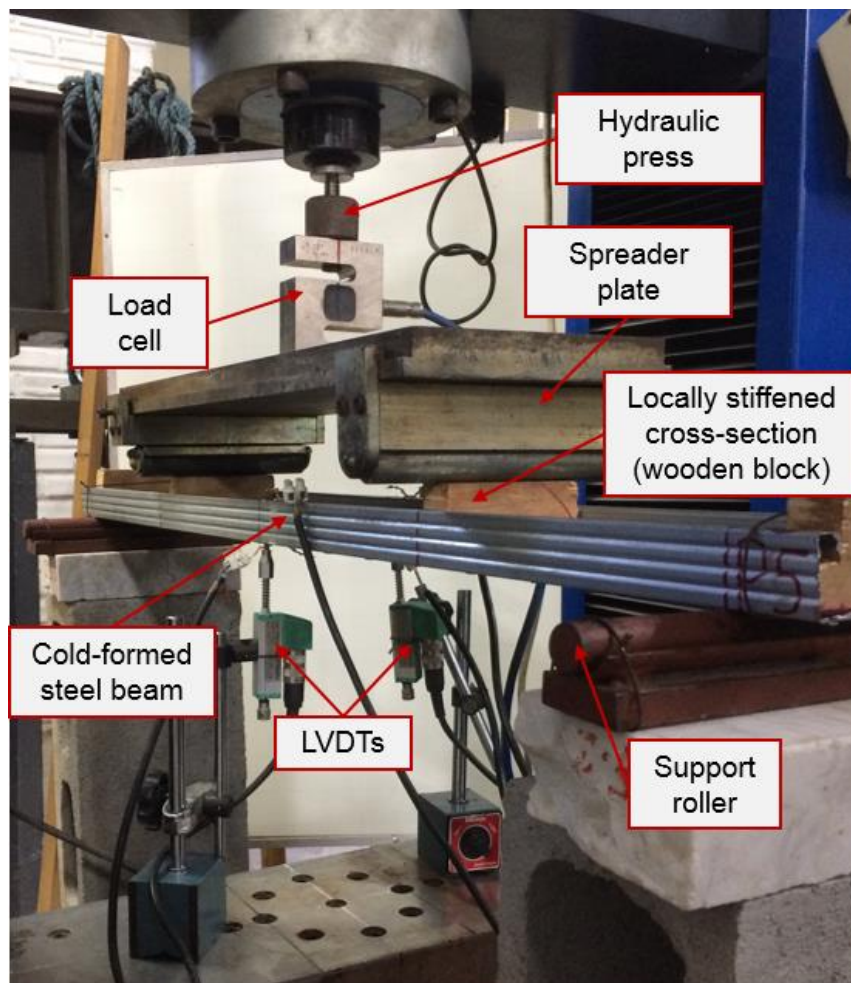
Source: author's own.

Figure 3.3 — Representation of (a) elevation and (b) cross-sectional view of the instrumentation employed in the bending tests of Gomes et al. (2019).

(a) Elevation view

(b) Cross-sectional view
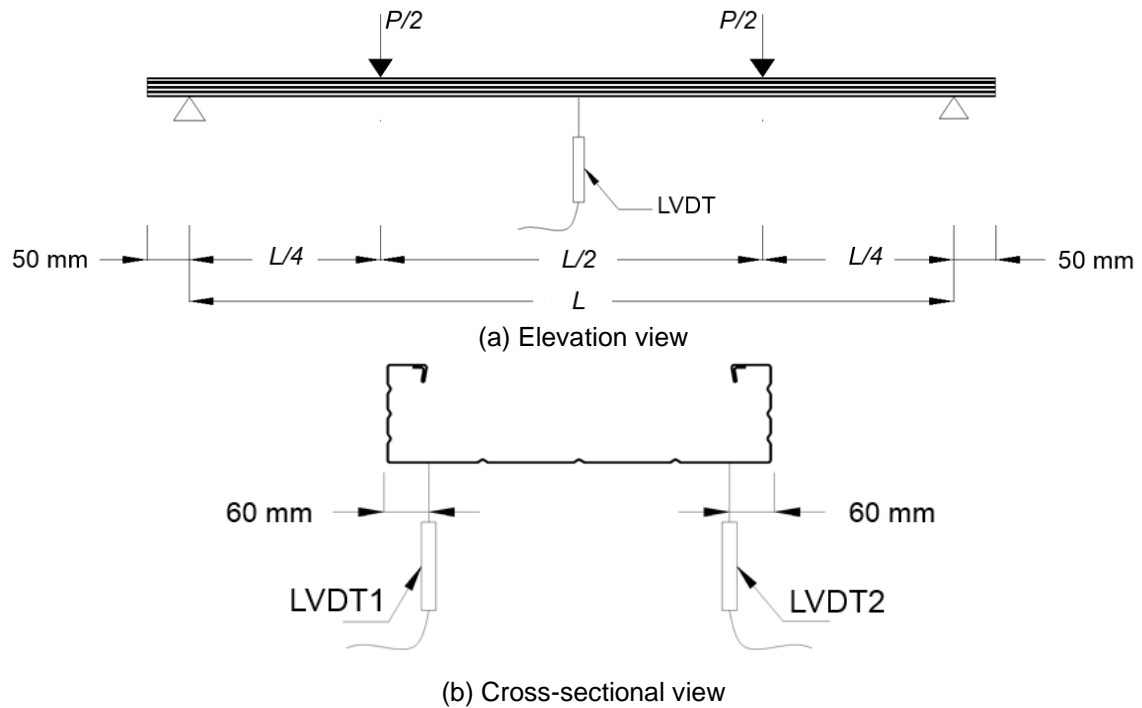
Source: author's own.

Figure 3.4 — Dimensions (in millimetres) of the wooden blocks used at supports and load points.
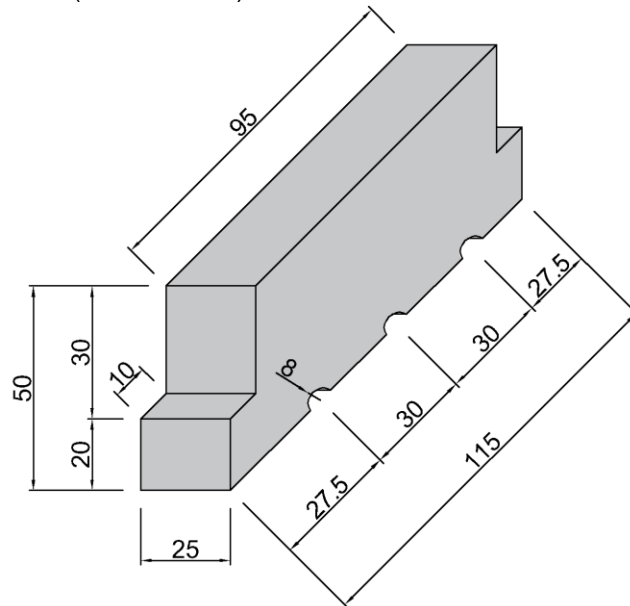
Source: author's own.
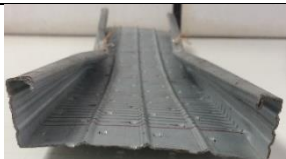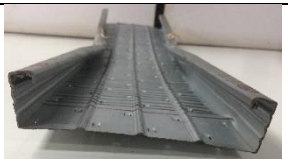
3.2.1.2 Theoretical predictions

The Direct Strength Method, briefly described in section 2.1, was used to obtain the theoretical predictions of nominal flexural strength ($M_{Rk,DSM}$) of the pilot experiment specimens. The finite strip software CUFSM (LI; SCHAFER, 2010; SCHAFER; ÁDÁNY, 2006) is used to determine the local and distortional critical

buckling moments for the examined cross-section, as shown in Figure 3.5. The elastic critical moment for flexural-torsional buckling is calculated according to Eq. (2.4), described in section 2.1, which is presented in the Brazilian standard ABNT NBR 14762:2010.

Table 3.2 presents the values of critical buckling moments, slenderness and moment capacity for specimens P0.5 and P0.9. Mean values of thickness (0.52 mm) and yield stress (290 MPa) provided by the manufacturer were used to perform the stability analysis. In both cases, distortional buckling controlled the moment capacity predictions.

Table 3.1 — Summary of the pilot experimental tests results.

	Specimen P0.5a			**Specimen P0.5b**	
	Span length (m)	0.50		Span length (m)	0.50
	P_u (kN)	4.16		P_u (kN)	4.06
	M_u (kN.m)	0.26		M_u (kN.m)	0.25

	Specimen P0.5c			**Specimen P0.9a**	
	Span length (m)	0.50		Span length (m)	0.90
	P_u (kN)	4.30		P_u (kN)	2.55
	M_u (kN.m)	0.27		M_u (kN.m)	0.29
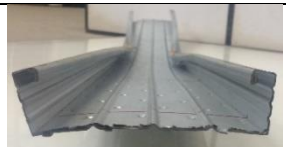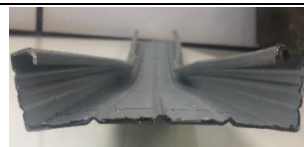
	Specimen P0.9b			**Specimen P0.9c**	
	Span length (m)	0.90		Span length (m)	0.90
	P_u (kN)	2.38		P_u (kN)	2.29
	M_u (kN.m)	0.27		M_u (kN.m)	0.26

Figure 3.5 — Signature curve from CUFSM (LI; SCHAFER, 2010; SCHAFER; ÁDÁNY, 2006) for typical examined cross-section.

(a) Local mode (b) Distortional mode
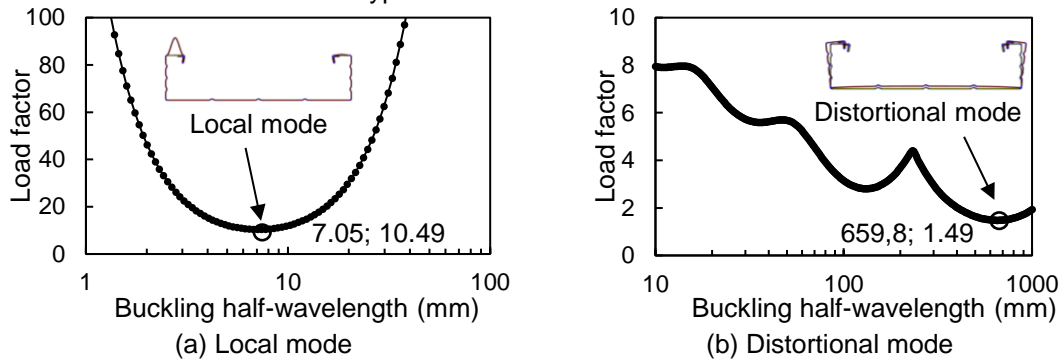
Source: author's own.

Table 3.2 — Theoretical predictions of nominal flexural strength (in kNm) per Direct Strength Method for the specimens of the pilot experimental program.

	Wf_y	Lateral-torsional buckling			Local buckling			Distortional buckling			$M_{Rk,DSM}$
		M_e	λ_0	$M_{R,e}$	M_ℓ	λ_ℓ	$M_{R,\ell}$	M_{dist}	λ_{dist}	$M_{R,dist}$	
P0.5	0.27	10.22	0.16	0.27	2.86	0.31	0.27	0.39	0.83	0.24	0.24
P0.9	0.27	3.17	0.29	0.27	2.86	0.31	0.27	0.39	0.83	0.24	0.24

3.2.1.3 Finite element model sensitivity analyses

3.2.1.3.1 Boundary conditions and loading

A general view of the boundary condition and loading position of the as-built physical tests is shown in Figure 3.6. Boundary conditions and loading positions were carefully examined by comparing the experimental and numerical failure mode and load-displacement response through a variety of attempts. Best results were found with the load applied by displacement control. Figure 3.7 illustrates the typical arrangement of the physical tests. Incremental displacements are imposed in the bottom corners of the transversal section of the CFS specimen, at a quarter of the span from its ends (see Figure 3.8a). Vertical displacements were constrained along the beam web at 50 mm from both ends, as shown in Figure 3.8b. To prevent rigid body motion, longitudinal displacements were constrained at midspan and transversal displacements at both ends. Additionally, lateral restraints were imposed on nodes along the flange at the supports and loading points to reproduce the effect of the wooden blocks used in physical tests.

Figure 3.6 — Overall scheme of the loading and boundary condition used in the physical tests.
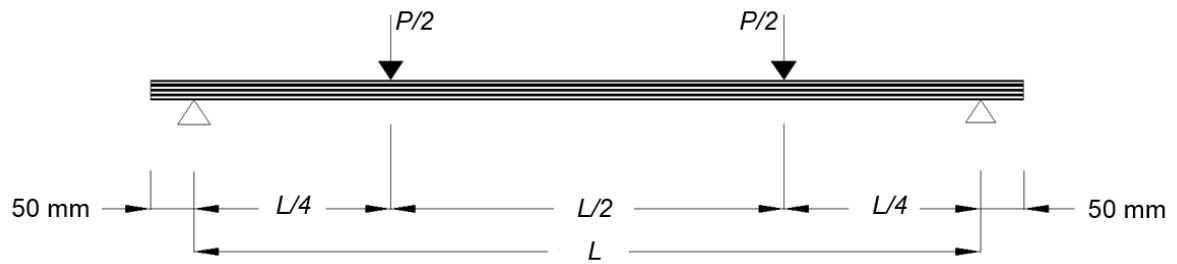
Source: author's own.

Figure 3.7 — Boundary conditions of a typical arrangement of the physical tests.
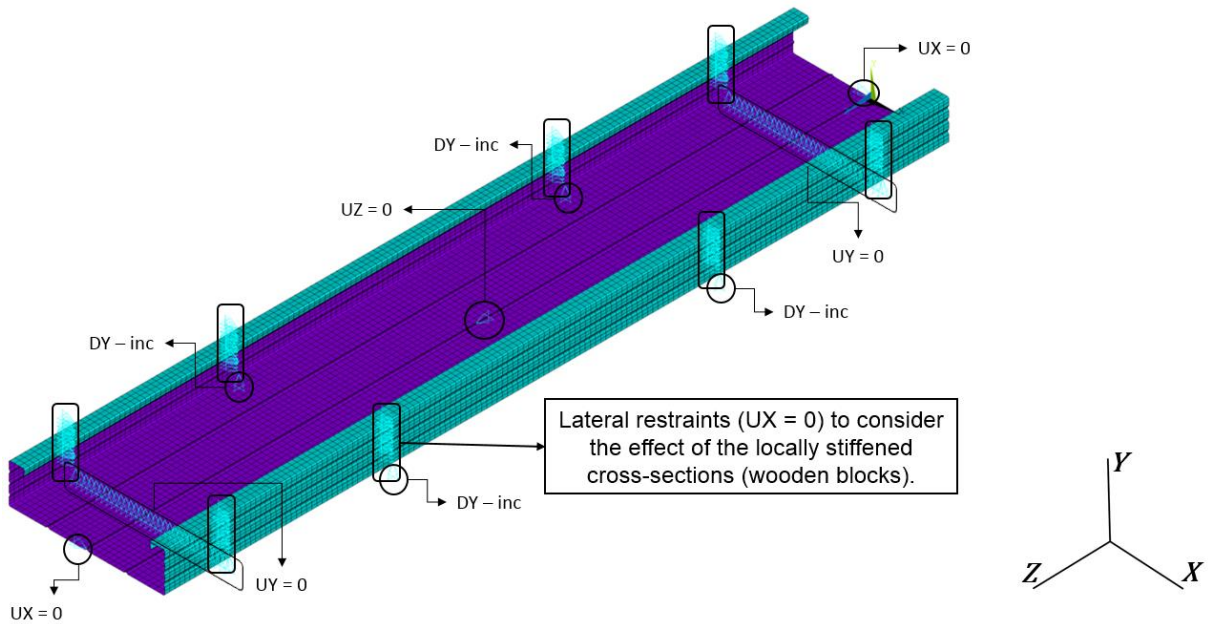
Source: author's own.

Figure 3.8 — Cross-section view of the (a) corners loading points and (b) vertical supports along the beam web.
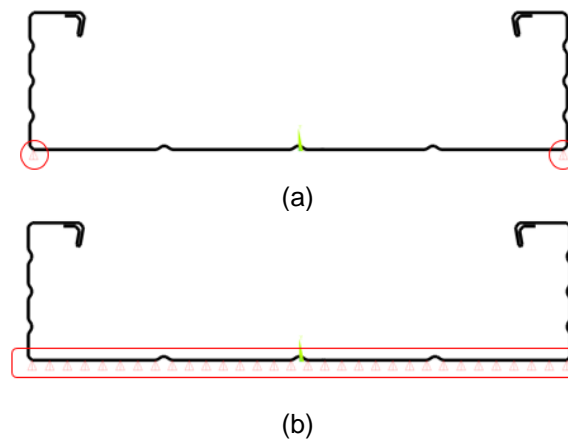
Source: author's own.

3.2.1.3.2 Element and mesh sensitivity

To assess the model's sensitivity to element choice and mesh density, different

element types and sizes, and number of integration points through the thickness were investigated. Only shell elements were tested in this study; even though other element types could be used to simulate thin-walled structures using ANSYS® 2020R1, such as solid elements (e.g. SOLID185 or SOLID186) or solid shell elements (e.g. SOLSH190). The four-node and eight-node shell elements SHELL181 and SHELL281, respectively, both with six degrees-of-freedom (DOF) at each node, were analysed. Whereas SHELL181 employs linear shape functions, SHELL281 employs quadratic shape functions.

A mesh study was performed with nominal element size varying from 100 mm to 3.5 mm with an aspect ratio, i.e., plate's length-to-width ratio, equal to one for flat elements, so that it is close to five for corner elements. Also, different numbers of integration points through the thickness were inspected: 5 points and 21 points.

The following modelling techniques were used in the studies: multilinear material model (see Section 3.2.1.3.4), loading with displacement control, Full Newton-Raphson solver solution method controlled by artificial damping (see Section 3.2.1.3.3) and no initial geometric imperfections (see Section 3.2.1.3.5). In addition, a cross-section thickness of 0.52 mm and beam free span length of 0.9 m were used in all analyses presented in this section. Also, default element options (KEYOPT) were used for both shell models and no issues related to shear locking were observed. Thereby, appropriate element type and mesh density could be selected for future finite element models.

Mesh density results are reported in Table 3.3 for SHELL181 models and in Table 3.4 for SHELL281 models. Results are presented in terms of comparisons between ultimate bending moment of each case ($M_{u,case\,\#}$) normalized by the value predicted by the finer mesh model ($M_{u,finer\,mesh}$). Figure 3.9 shows the ultimate bending moment *versus* number of elements for models with SHELL181 and SHELL281 elements. Figure 3.10 and Figure 3.11 show the load-displacement responses obtained from nonlinear analyses performed with each mesh size.

The model with nominal mesh size of 4 mm and SHELL181 elements (37500 elements), which is highlighted with red colour in Table 3.3 and Figure 3.10, was selected for subsequent analyses. Although both shell models present rapidly convergent solution (as shown in Table 3.3, Table 3.4 and Figure 3.9), the post-collapse response presented a high sensitivity to mesh density (as shown in Figure 3.10 and Figure 3.11). In both shell models the post-collapse response converges in

similar fashion when the nominal mesh size is smaller than 5 mm. Thus, all subsequent analyses are performed with 4 mm mesh size, since the ultimate bending moment deviated only 0.1% from results obtained with the finer mesh model. SHELL181 element was selected for subsequent analyses, since neither computational cost nor response accuracy were improved with the use of SHELL281 elements.

Table 3.3 — Comparison between ultimate bending moment of finite element models with different mesh densities of SHELL181 elements.

Case #	Element size [mm]	Number of elements	$\dfrac{M_{u,case\ \#}}{M_{u,finer\ mesh}}$
1	100.0	790	1.035
2	40.0	2295	1.012
3	20.0	4650	1.003
4	17.5	5394	1.006
5	15.0	6499	1.005
6	12.5	8400	1.004
7	10.0	10900	1.003
8	7.5	15946	1.007
9	5.0	35400	1.006
10	**4.0**	**37500**	**1.001**
11	3.5	49192	1.000

Table 3.4 — Comparison between ultimate bending moment of finite element models with different mesh densities of SHELL281 elements.

Case #	Element size [mm]	Number of elements	$\dfrac{M_{u,case\ \#}}{M_{u,finer\ mesh}}$
1	100.0	940	1.038
2	40.0	2350	1.019
3	35.0	2726	1.019
4	30.0	3196	1.016
5	25.0	3920	1.017
6	20.0	4900	1.019
7	15.0	6566	1.018
8	10.0	10400	1.015
9	5.0	23600	1.006
10	4.0	33000	1.001
11	3.5	38896	1.000

Figure 3.9 — Ultimate bending moment versus number of SHELL181 and SHELL281 elements.
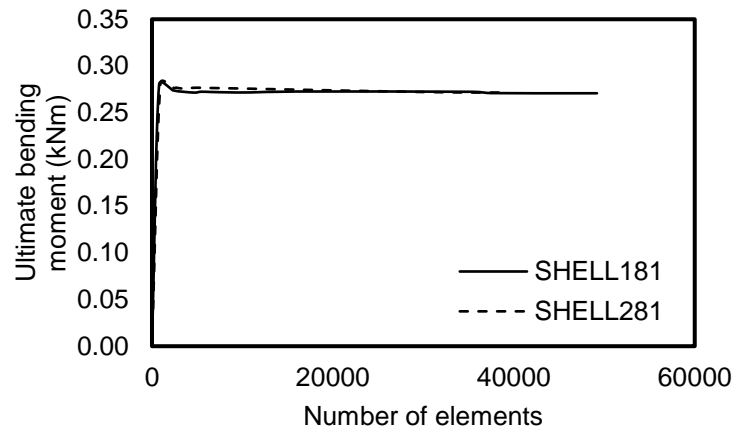
Source: author's own.

Figure 3.10 — Load-displacement responses of SHELL181 models with different mesh sizes.
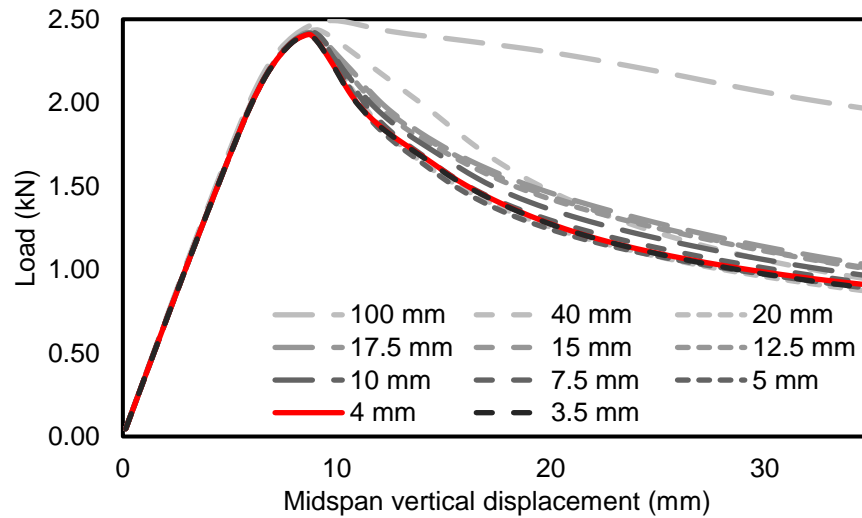
Source: author's own.

Figure 3.11 — Load-displacement responses of SHELL281 models with different mesh sizes.
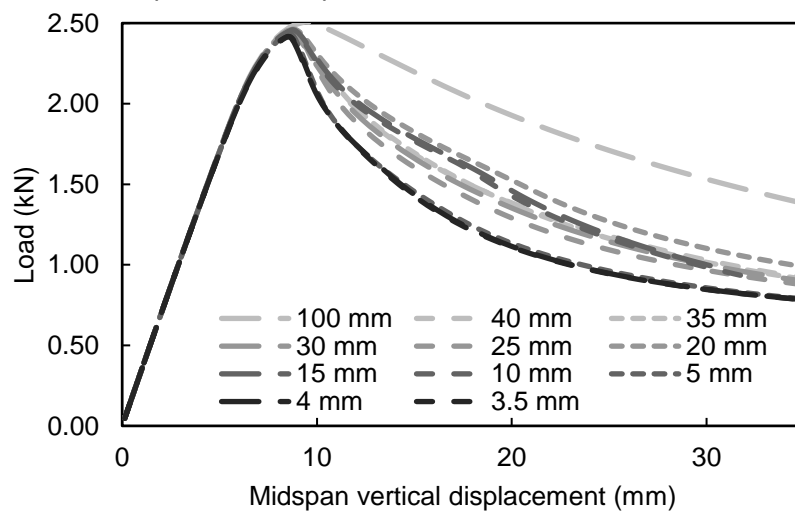
Source: author's own.

Figure 3.12 illustrates the number of elements used to represent the main

portions of the beams cross-section. Overall, 116 nodes are used to discretize the member cross-section, corresponding to: three elements for stiffeners (n_{stiff}), one element for corners (n_{corner}), two elements for flat flange portions (n_{flange}), seven elements for flat web portions(n_{web}) and five elements for intermediate stiffeners (n_{int}).

Figure 3.12 — Illustration of the number of elements used to represent the main portions of the beams cross-section.
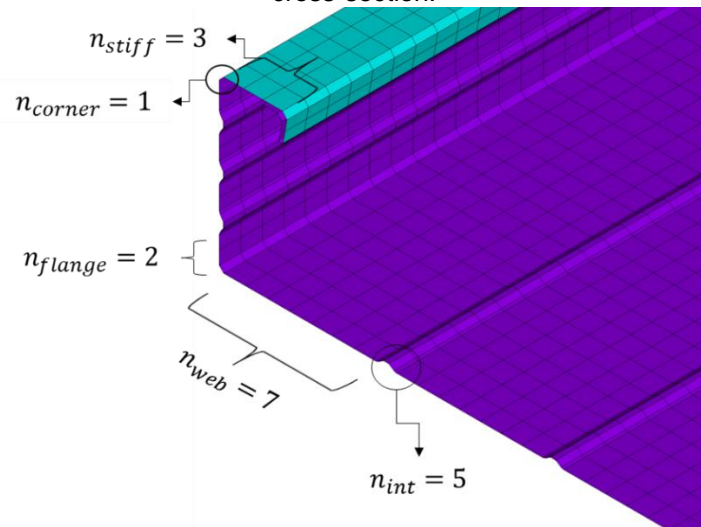
Source: author's own.

Figure 3.13 displays the load-displacement responses of the SHELL181 models with 5 and 21 integration points through the element thickness. A deviation smaller than 0.001% was found between the ultimate bending moment of the models. The main difference is that a higher number of iterations was successful converged with 21 integration points. Hence, 5 points of integration are employed in the FE models to obtain the numerical results of subsequent analyses and switched to 21 points when convergence issues arose during the prediction of post-collapse behaviour.

Figure 3.13 — Load-displacement responses of models with different number of integration points through the thickness.
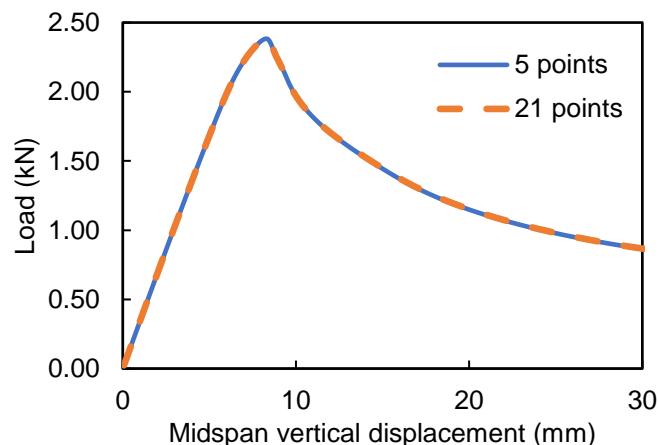
Source: author's own.

3.2.1.3.3 Solution solver sensitivity

Two different solution schemes are examined in this section to solve the nonlinear collapse analyses of cold-formed steel beams, since Full Newton-Raphson method presented convergence issues to reach peak load and/or capture post-ultimate response. The nonlinear stabilisation technique and arc-length (Riks) method are assessed in this study, and are shortly described in section 2.2.6.

Several researches discuss the accuracy of the nonlinear stabilisation technique when analysing cold-formed steel members (Kyvelou, 2017; Hui, 2014; Schafer, Li and Moen, 2010). Studies indicate that this technique can achieve results that are equivalent to those attained with arc-length (Riks) method if sufficient number of iterations prior to the peak load is ensured. For example, Schafer, Li and Moen (2010) found that the arc-length (Riks) method converges with less steps (about 5 steps) than artificial damping (about 15 steps). The first author of this paper suggests 20 steps prior to the peak load as a rule of thumb for any type of collapse analysis. Also, they found that artificial damping usually provides a higher peak load than arc-length (Riks) method. Therefore, the load increment size was carefully examined to determine the minimum number of successful iterations prior to peak load for any given analysis.

The following modelling techniques were used in the studies: multilinear material model, four-node shell elements (SHELL181), loading with displacement control, no initial geometric imperfections, cross-section thickness of 0.52 mm and beam free span length of 0.9 m.

Results of all cases analysed are reported in Table 3.5 and their load-displacement responses are shown in Figure 3.14. Whereas 19 steps prior to the peak load was enough to converge the solution with arc-length (Riks) solver, more than 60 steps were needed to reach a convergent solution using artificial damping. However, it should be observed that only a small deviation was found amongst the results. For example, normalizing the ultimate bending moments (M_u) obtained for the smallest and largest number of steps, less than 0.69% and 0.30% are found for the arc-length (Riks) and artificial damping responses, respectively. Comparing results from both algorithms directly, the ultimate bending moment (M_u) predicted with artificial damping tended to be slightly larger than those attained with arc-length (Riks) solver, as shown in Figure 3.14b.

In subsequent analyses, artificial damping will be used as the solution scheme. Even though the literature indicates that the arc-length (Riks) method is the preferred choice to ensure the solution convergence, artificial damping was able to predict the peak load and post-collapse response of the models developed for the Trelifácil® solution with the trussed girder coupled to the cold-formed steel beam (see section 3.3).

Moreover, Schafer, Li and Moen (2010) affirm that the artificial damping technique is a powerful algorithm and can provide a converged solution for several cases in which arc-length (Riks) solver fails to converge. On the other hand, the authors also state that the artificial damping solver is an approximation and should be used carefully. In general, this technique is controlled by an energy-dissipation ratio, which has a default value of $1x10^{-4}$ in ANSYS 2020R1. Therefore, to assess the model's sensitivity to this ratio and to find its most appropriate value, nonlinear analyses with different ratios of energy-dissipation were conducted. Load-displacement responses are shown in Figure 3.16, which shows that a converged solution may be obtained with energy-dissipation ratios smaller than 1E-3. To ensure that the solver approach is not artificially removing excessive energy from the system, an energy-dissipation ratio of 1E-4 will be used in subsequent analyses.

Table 3.5 — Ultimate bending moment values for arc-length (Riks) and artificial damping models with different number of steps prior to peak load.

Case #	Description	M_u (kNm)
1	6 steps – arc-length (Riks)	0.266
2	12 steps – arc-length (Riks)	0.267
3	19 steps – arc-length (Riks)	0.268
4	35 steps – arc-length (Riks)	0.268
5	66 steps – arc-length (Riks)	0.268
6	16 steps – Artificial damping	0.268
7	24 steps – Artificial damping	0.267
8	61 steps – Artificial damping	0.268
9	123 steps – Artificial damping	0.268
10	613 steps – Artificial damping	0.268

Figure 3.14 — Load-displacement responses for (a) arc-length (Riks) solver and (b) inset plot for arc-length (Riks) solver with different number of steps prior to peak load.

(a)

(b)
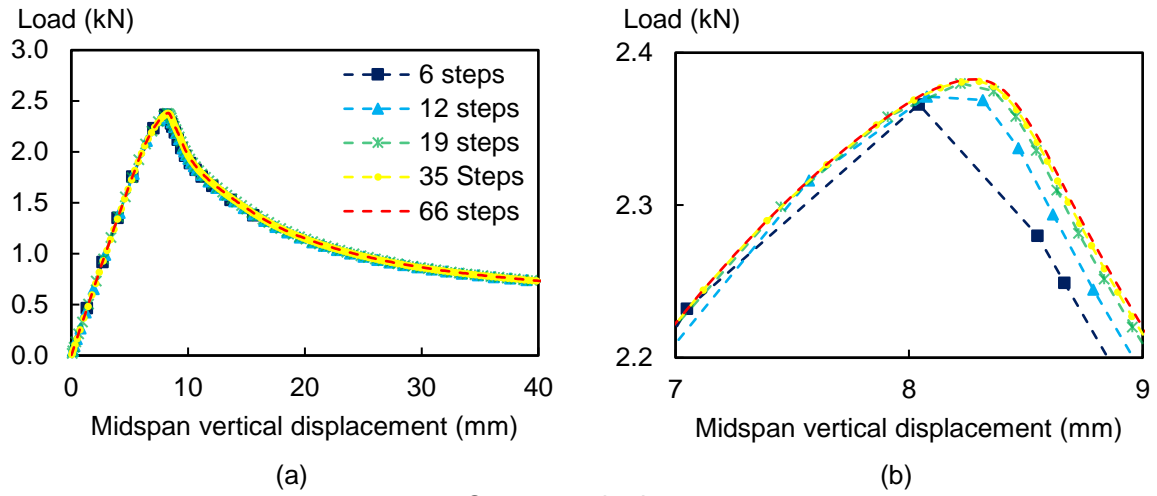
Source: author's own.

Figure 3.15 — Load-displacement responses for (a) artificial damping solver and (b) inset plot for artificial damping solver with different number of steps prior to peak load.

(a)

(b)
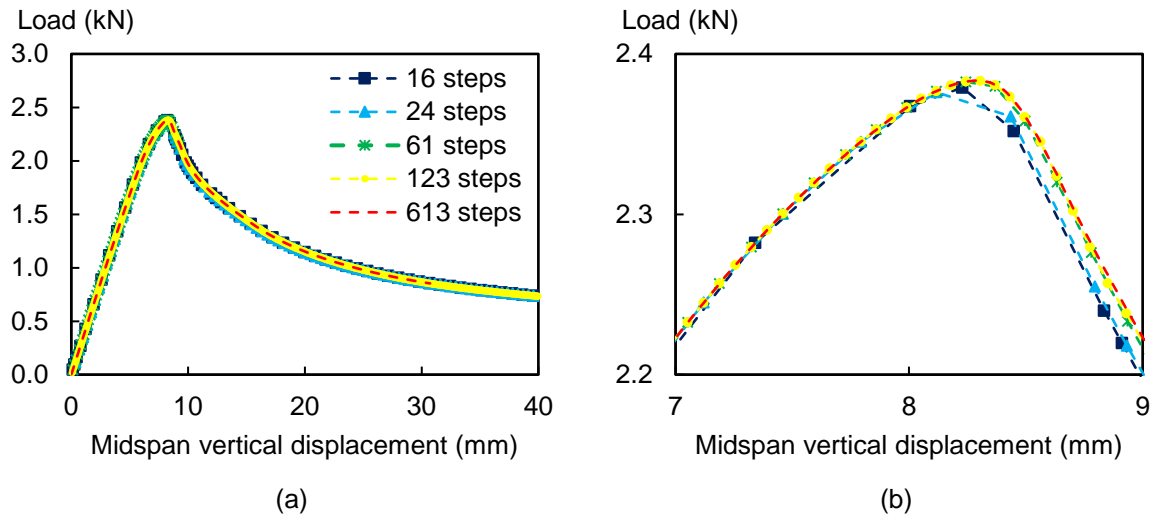
Source: author's own.

Figure 3.16 — Artificial damping solver sensitivity to energy-dissipation ratio.
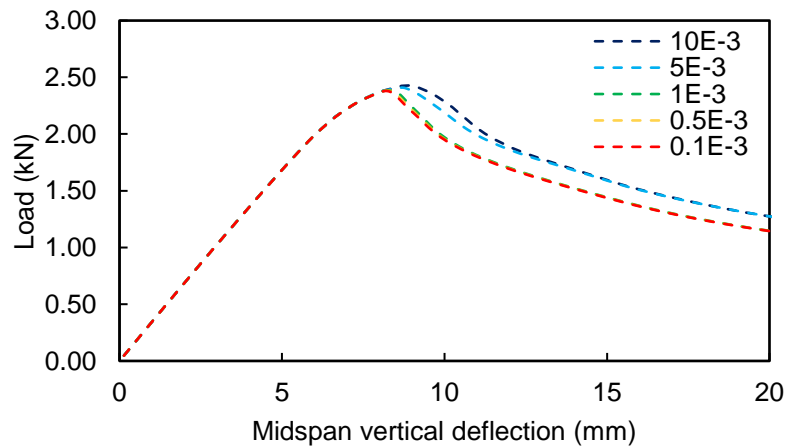
3.2.1.3.4 Plasticity model sensitivity

In section 2.2.3.1 different stress-strain relationships that may be used to represent cold-formed steel are presented. Therefore, two of those material modelling techniques are used to identify the appropriate stress-strain behaviour of the cold-formed steel used in the physical tests, as follows:

    a) Bilinear material model (BISO): an elastic perfectly-plastic material model with initial elastic modulus (E) of $200\ GPa$;

    b) Multilinear material model (MISO): the basic Ramberg-Osgood stress-strain relationship up to 0.2% proof stress followed by a straight line with a constant slope expressed as a fraction of initial elastic modulus ($E = 200\ GPa$), as shown in Eq. (3.1). The value of $E/50$ was adopted for the slope of the straight line and the shape parameter n equal to 28, as in Haidarali and Nethercot (2011) and Ye et al. (2016).

$$\epsilon_e = \frac{\sigma_e}{E} + 0{,}002\left(\frac{\sigma_e}{\sigma_{0,2}}\right)^n \qquad for\ \sigma \leq \sigma_{0,2}$$

$$\epsilon_e = \epsilon_{0.2} + \frac{50\left(\sigma - \sigma_{0,2}\right)}{E} \qquad for\ \sigma > \sigma_{0,2}$$

(3.1)

Figure 3.17 shows the two material models mentioned above. An elastic modulus of 200 GPa was adopted and yield stress (0.2% proof stress, $\sigma_{0.2}$) of 290 MPa provided by the steel manufacturer laboratory tests was used. Additionally, large-strain analyses (NLGEOM,ON) are performed in this study, then all the input engineering values for stresses and strains in the large-strain region (i.e., after 0.2% proof stress) are converted to true values, as explained in sub-section 2.2.3.1.

Figure 3.17 — Material models assessed in this study.
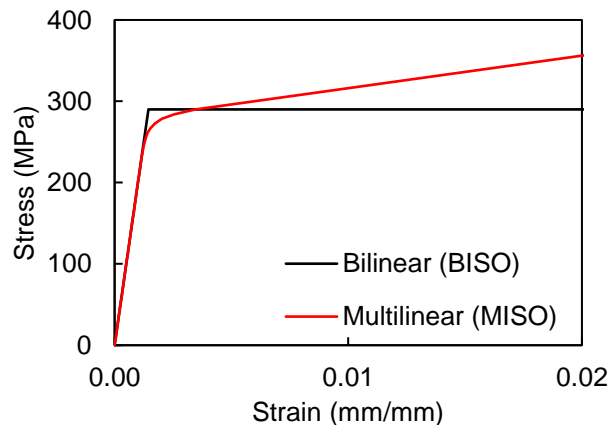
Source: author's own.

The results of the material modelling technique study are examined in the

context of comparisons between load-displacement responses of each case analysed for two beam span lengths (0.5 m and 0.9 m), as shown in Figure 3.18. In both cases, a bilinear material model presented higher flexural strength and stiffness. Deviations between the ultimate bending moment predicted with bilinear and multilinear material models of 1.09% and 3.45% were found for member lengths of 0.5 m and 0.9 m, respectively. Thus, to avoid overestimating the flexural strength and stiffness of the beams, the multilinear material model was chosen for subsequent analyses.

Figure 3.18 — Load-displacement responses of finite element models with different material modelling techniques plotted against experimental results.

Source: author's own.
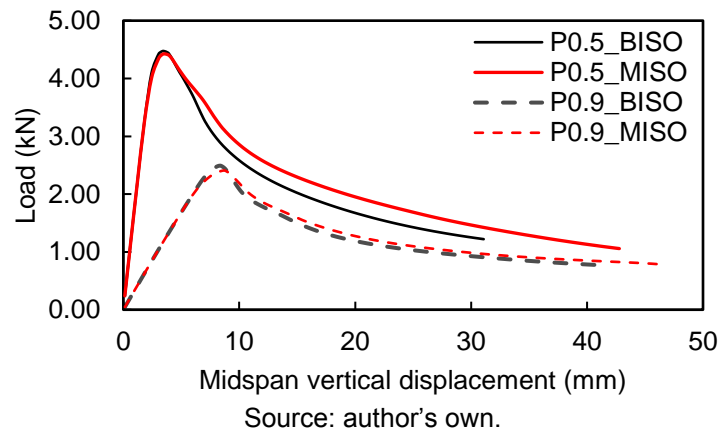
3.2.1.3.5 Initial geometrical imperfection sensitivity

Initial geometrical imperfections may play an important role in the prediction of failure mode and post-collapse regime in finite element analyses of cold-formed steel members (SCHAFER; LI; MOEN, 2010). As mentioned in section 2.2.2, three main factors must be considered to properly assess model initial geometrical imperfections: imperfection shapes, magnitude factors and combination coefficients.

In this research, imperfection shape is generated from a finite element buckling analysis. The lowest critical buckling mode is used as the imperfection shape. Buckling analyses were performed with modelling techniques similar to those used by Favarato et al. (2019b) (details in (FAVARATO, 2018)). Favarato (2018) conducted a series of finite element buckling analyses to predict critical buckling moments of the Trelifácil® solution steel formwork. Four-node shell elements (SHELL181) were also used to discretize the finite element model. At each support, translations were restrained in the x-axis in the webs' plane portions and in the y-axis in the bottom flange's flat portion, creating fork supports. Nodal forces were applied at both ends to create a stress distribution of a unitary bending moment (1 Nm) about the minor axis of inertia. Figure

3.19 illustrates the boundary conditions adopted by Favarato (2018).

Figure 3.19 — Illustration of the end moments (edge forces) and boundary conditions used in the finite element elastic buckling analysis conducted by Favarato (2018).
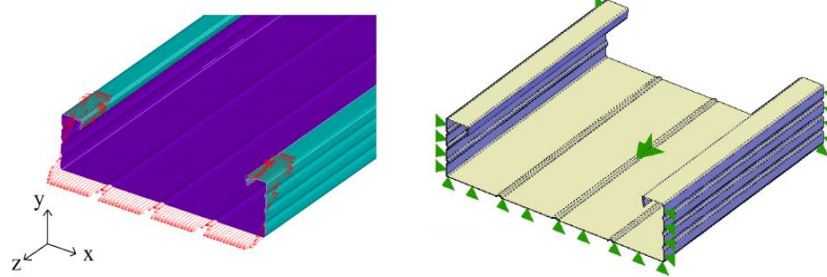
Source: (FAVARATO, 2018).

Scientific literature provides a variety of recommendations to determine magnitude factors. Most studies, as reported in section 2.2.2, prescribe values between $0.1t$ and $0.75t$ for both local and distortional imperfection shapes. According to statistical analyses performed by Schafer and Peköz (1998b), which are shown in Table 2.2, there are few cases in which magnitude values are above $0.75t$. Therefore, in this research, three values of magnitude factors are examined: $0.1t$, $1.0t$ and $4.0t$. The combination factor is equal to one, since only one imperfection shape is used to create the perturbed mesh.

The buckling modes used as imperfection shape for beam span lengths of 0.5 m and 0.9 m are shown in Figure 3.20. Close values between finite strip and finite element critical buckling moments (M_{cr}) were observed. While finite strip critical buckling moment is 0.39 kNm, finite element critical buckling moments are 0.40 kNm and 0.37 kNm for beams with a length of 0.5 m (P0.5) and 0.9 m (P0.9), respectively. Additionally, similar buckling mode shape and half-wavelength was observed by comparing responses from both methods. As such, the finite element solid model geometry was updated (UPGEOM) to these eigenvectors factored by the magnitude values.

Figure 3.20 — Buckling modes used as imperfection shape of (a) P0.5 and (b) P0.9 FE models.

(a) P0.5: $M_{cr} = 0.40\ kNm$ (b) P0.9: $M_{cr} = 0.37\ kNm$
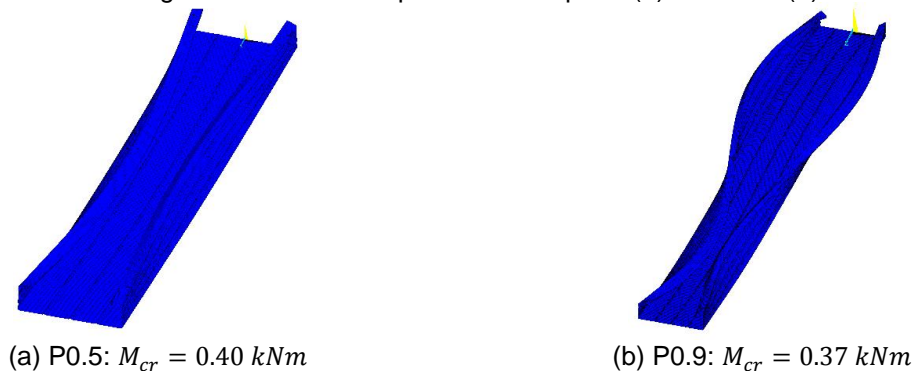
Source: author's own.

The results of the initial geometrical imperfection study are examined in the context of losses in flexural strength. Moment capacity of models with different magnitude factors $M_{u,case\ \#}$ are normalized by those attained values of models without inclusion of geometrical imperfections $M_{u,case\ 1}$. Table 3.6 summarises the results of specimen P0.5 and Table 3.7 of specimen P0.9. Also, Figure 3.21 shows the load-displacement responses of the nonlinear analyses conducted for each case studied. The results indicate low sensitivity to the inclusion of geometrical imperfections, as well as to the variation increase of magnitude factor. Ultimate bending moment, post-collapse response and failure mode have not shown significant variations as function of the initial geometrical imperfection. As such, they will be neglected in subsequent analyses.

Table 3.6 — Summary of gains or losses in flexural strength and stiffness of the specimen P0.5 by including initial geometrical imperfections with different magnitude factors.

Case #	Specimen	Magnitude factor	$\dfrac{M_{u,case\ \#}}{M_{u,case\ 1}}$
1	P0.5	0.0	1.00000
2	P0.5	$0.1t$	0.99961
3	P0.5	$1.0t$	0.99601
4	P0.5	$4.0t$	0.98401

Table 3.7 — Summary of gains or losses in flexural strength and stiffness of the specimen P0.9 by including initial geometrical imperfections with different magnitude factors.

Case #	Specimen	Magnitude factor	$\dfrac{M_{u,case\ \#}}{M_{u,case\ 1}}$
1	P0.9	0.0	1.00000
2	P0.9	$0.1t$	0.99999
3	P0.9	$1.0t$	0.99916
4	P0.9	$4.0t$	0.98867

Figure 3.21 — Load-displacement responses of the initial geometrical imperfection sensitivity study with different magnitude factors.
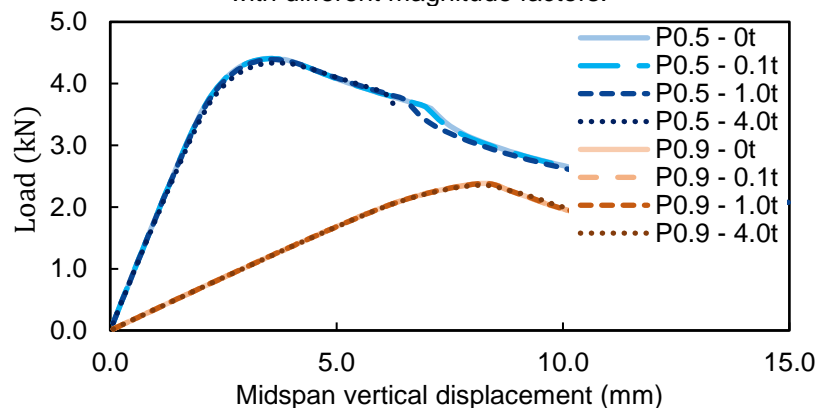
Source: author's own.

3.2.1.4 Confrontation of numerical and experimental results of Gomes et al. (2019)

In this section all numerical results, i.e., the DSM and FEM results, are confronted to the measured data found with the pilot experiments conducted by Gomes et al. (2019). The DSM results and details are presented in section 3.2.1.2. The FEM results are obtained with the following modelling techniques:

a) four-node shell elements (SHELL181) with nominal mesh size of 4 mm and 21 points of integration through the cross-section thickness;

b) geometrical and material nonlinear analyses of simply supported beams under four-point bending solved with Full Newton-Raphson method controlled by artificial damping;

c) loads applied with displacement control;

d) no initial geometrical imperfections;

e) plasticity model represented by a multilinear stress-strain curve with von Mises yield criterion, associative flow rule and isotropic hardening.

Results are presented in the context of comparisons between finite element and experimental flexural strength responses. Table 3.8 presents finite element moment capacity $M_{u,FE}$ normalised by experimental values $M_{u,Exp}$, while load-displacement responses are shown in Figure 3.22. The typical observed failure modes found in physical tests are shown alongside with finite element collapse modes in Figure 3.23.

On one hand, good agreement was found between numerical and experimental strength predictions. A mean $M_{u,FE}/M_{u,exp}$ ratio of 1.03 was obtained for the finite element results, while a mean $M_{Rk,DSM}/M_{u,exp}$ ratio of 0.91 for the DSM values. Further, in all cases the beam specimens failed predominantly by distortional buckling with half-wavelength equal to the load span length (see Figure 3.23), i.e., the distance between loading points, equally to those observed in the physical tests. Therefore, both peak load and collapse mode indicate the accuracy of the finite element strength predictions.

On the other hand, it can be noted in Figure 3.22 that the finite element model failed to accurately predict the flexural stiffness observed in the physical tests. The unquantified stiffness promoted by the wooden blocks in the load and support points challenges the agreement between numerical and experimental flexural stiffness. Nevertheless, both FEM and DSM could satisfactorily predict the flexural strength

observed in the pilot experiments conducted by Gomes et al. (2019), which is the main focus of this pilot study. Additionally, the pilot experiment and numerical analyses conducted contribute to the design of future investigation on this subject, which is also amongst the goals of this research.

Table 3.8 — Comparison of finite element strength and stiffness predictions with average experimental results.

Specimen	$M_{u,FE}/M_{u,exp}$	$M_{Rk,DSM}/M_{u,exp}$
P0.5a	1.06	0.93
P0.5b	1.09	0.95
P0.5c	1.03	0.90
P0.9a	0.94	0.85
P0.9b	1.01	0.91
P0.9c	1.05	0.95
Average	**1.03**	**0.91**
Coefficient of variation (COV)	**0.04**	**0.04**

Figure 3.22 — Load-displacement responses of finite element models with different material modelling techniques plotted against experimental results.


(a) $L = 0.50\ m$

(b) $L = 0.90\ m$
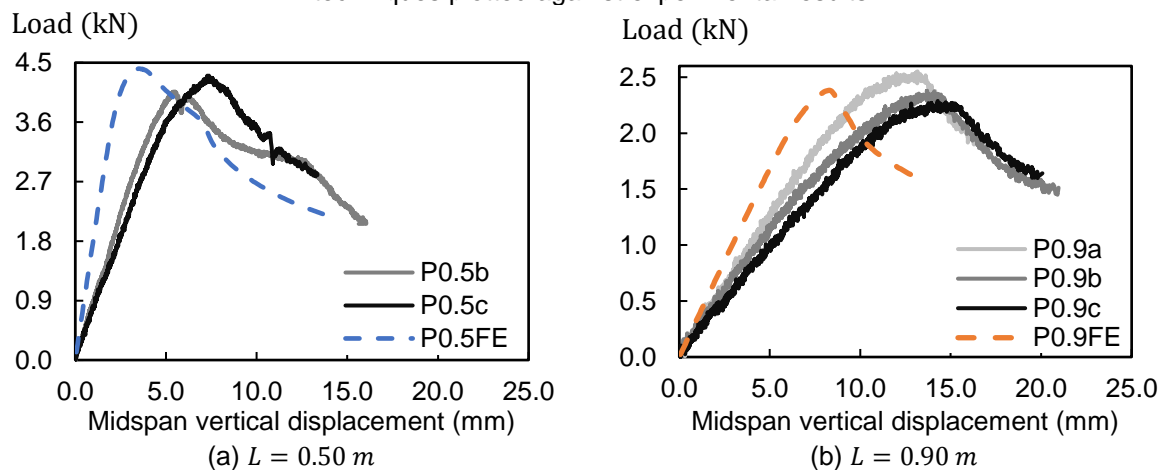
Source: author's own.

Figure 3.23 — Comparison of the typical modes of failures found in the experimental and finite element analyses.

(a) Mode of failure of the P0.5 specimen

(b) Mode of failure of the P0.9 specimen
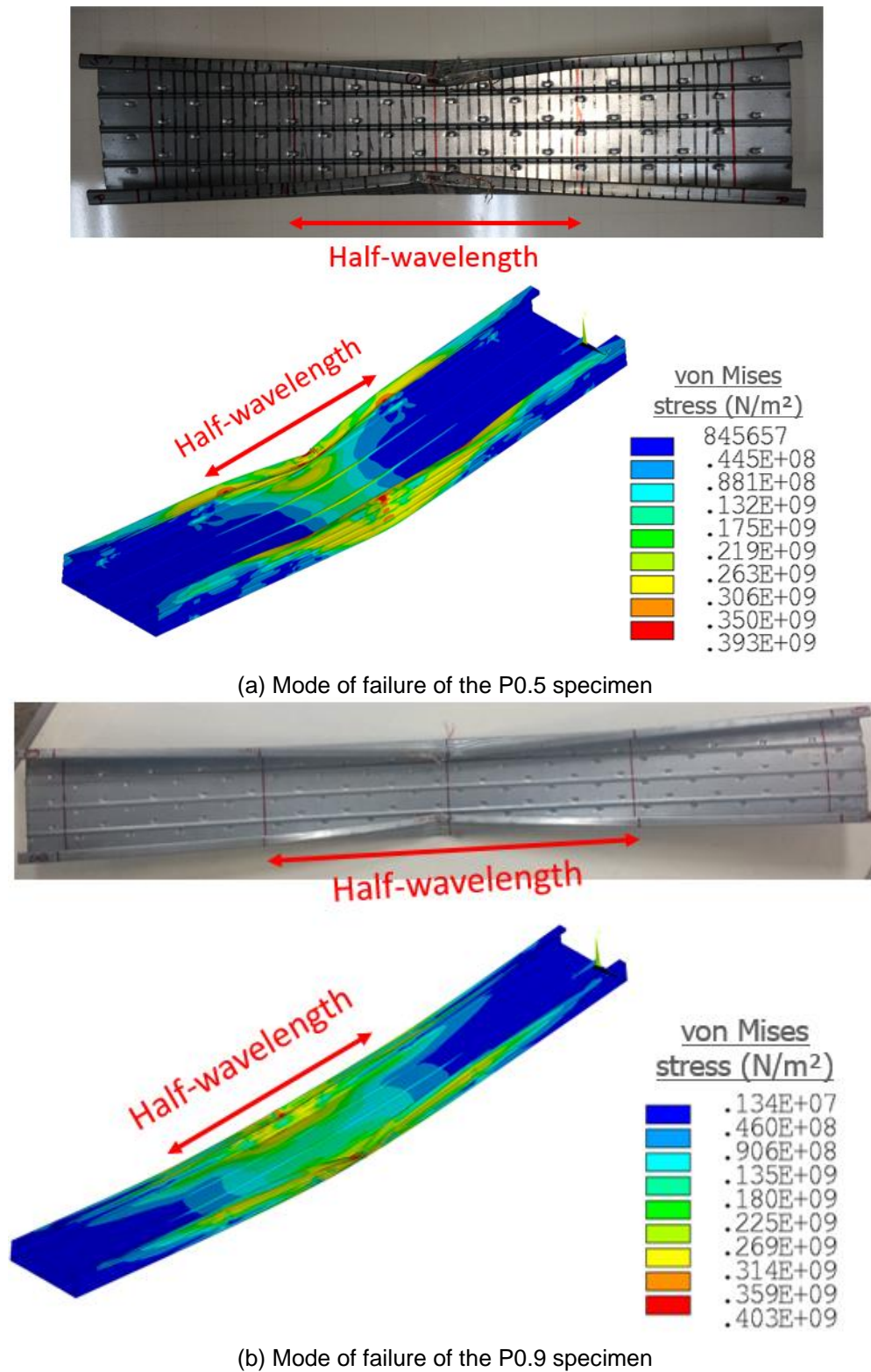
Source: author's own.

3.2.2 Finite element modelling of physical tests conducted by Candido (2020, in progress)

The key differences between the testing program conducted by Candido (2020, in progress) and the pilot experiment of Gomes et al. (2019) are the removal of wooden blocks and the substitution of loading apparatus. Even though the research of Candido (2020, in progress) is underway, some tests were already conducted and the data reasonably agree with FEM and DSM results. The following sections present a brief review of testing setup, as well as basic features of the theoretical and finite element predictions.

3.2.2.1   Testing setup of Candido (2020, in progress)

Candido (2020, in progress) conducted collapse tests of six simply supported beams subjected to four-point bending. Figure 3.24 shows the experimental layout of these tests. Nominal dimensions of the cross-sections are shown in Figure 1.9. In this study, three beam span lengths are tested: 1.0 m, 1.4 m and 1.8 m. Two linear variable displacement transducers (LVDT) are used to measure vertical deflections at midspan. A hydraulic press was used to apply a concentrated load on a spreader beam, which equally divided the load into two loading rollers distanced by 464.25 mm from each other. Figure 3.25 illustrates the employed instrumentation of the four-point bending tests and Table 3.9 shows the dimensions of the cold-formed steel beams tested. A detailed description of these physical tests will be given in Candido (2020, in progress), while the measured ultimate bending moments and load-displacement responses are presented with numerical results in Section 3.2.2.4.

Figure 3.24 — Experimental layout of four-point bending tests conducted by Candido (2020, in progress).
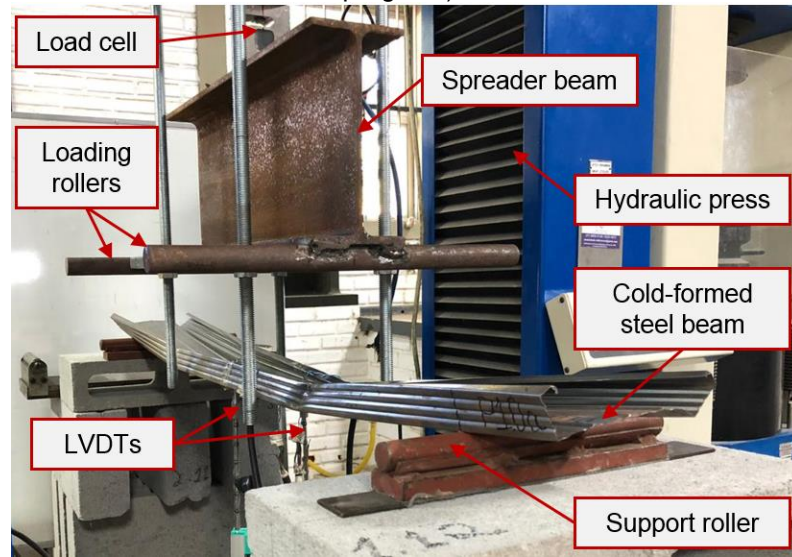
Source: author's own.

Figure 3.25 — Instrumentation employed in the tests conducted by Candido (2020, in progress).

(a) Elevation

(b) Cross-section *A-A*
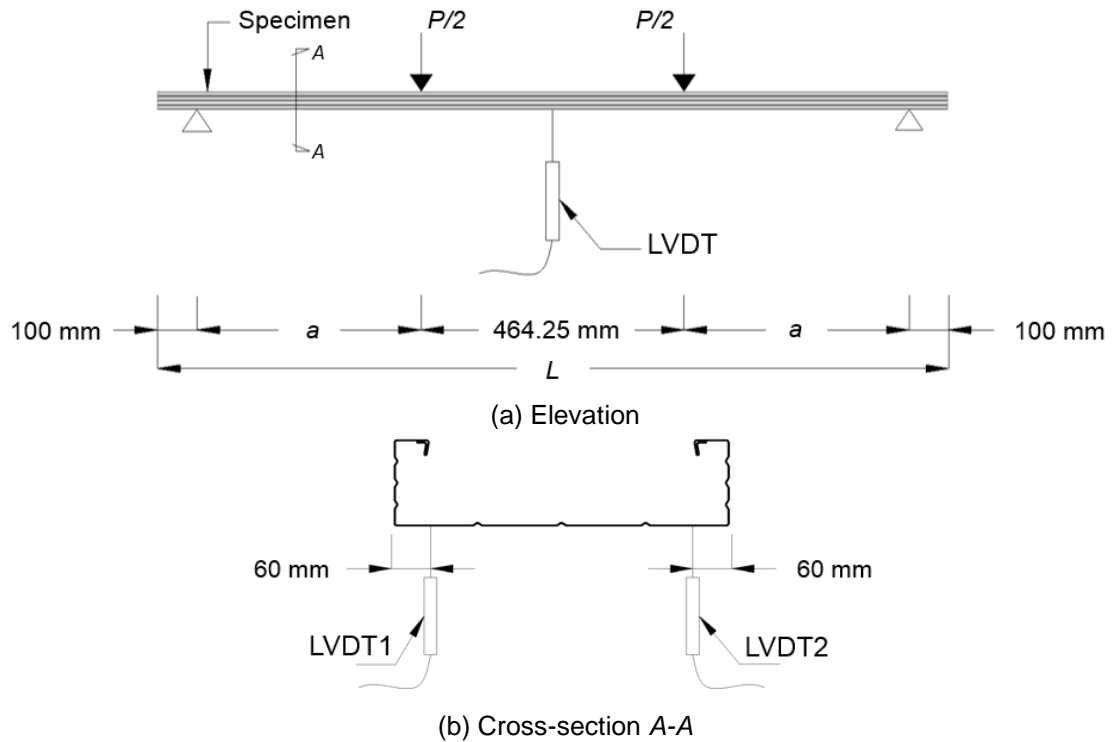
Source: author's own.

Table 3.9 — Dimensions of cold-formed steel beams used in the tests of Candido (2020, in progress).

Specimen	Free span length (mm)	*L* (mm)	*a* (mm)
P1.0	1000	1200	267.875
P1.4	1400	1600	467.875
P1.8	1800	2000	667.875

3.2.2.2 Theoretical predictions

The Direct Strength Method was used to obtain the theoretical predictions of nominal flexural strength ($M_{Rk,DSM}$) of the physical tests conducted by Candido (2020, in progress). Table 3.10 presents the values of critical buckling moments obtained using CUFSM, as well as slenderness and moment capacity determined for specimens P1.0, P1.4 and P1.8. A measured thickness of 0.515 mm and yield stress (0.2% proof stress $\sigma_{0.2}$) of 327 MPa provided by the steel manufacturer were used, the latter of which obtained from coupon tests carried out for samples cut from the coil prior to section-forming. For all member lengths, distortional buckling controlled the moment capacity prediction. Comparisons with experimental results are shown in Section 3.2.2.4.

Table 3.10 — Theoretical predictions of nominal flexural strength (in kNm) per Direct Strength Method for the specimens tested by Candido (2020, in progress).

	Wf_y	Lateral-torsional buckling			Local buckling			Distortional buckling			$M_{Rk,DSM}$
		M_e	$`_0$	$M_{R,e}$	M_ℓ	$`_\ell$	$M_{R,\ell}$	M_{dist}	$`_{dist}$	$M_{R,dist}$	
P1.0	0.30	2.57	0.34	0.30	2.86	0.33	0.30	0.39	0.88	0.26	**0.2580**
P1.4	0.30	1.32	0.48	0.30	2.86	0.33	0.30	0.39	0.88	0.26	**0.2580**
P1.8	0.30	0.80	0.62	0.30	2.86	0.32	0.30	0.39	0.88	0.26	**0.2580**

3.2.2.3 Finite element model

The main modifications in the finite element models developed in the last section is related to boundary conditions. The boundary conditions were applied at bottom nodes on the corners to provide vertical support and at top corner nodes to impose loads in the finite element model (again with displacement control), as illustrated in Figure 3.26. Due to the removal of the wooden blocks during the physical tests, a portion of the beam web lost contact with the support rollers so that only bottom corners points remained in place, which justifies the modification of support conditions. The choice for applying loads at top corner nodes relies on the points of contact between the loading apparatus and the member specimen. Therefore, excepting the boundary conditions, all finite element modelling features used in this study were similar to those described in sub-section 3.2.1.4.

Figure 3.26 — Boundary conditions for the second set of finite element models.
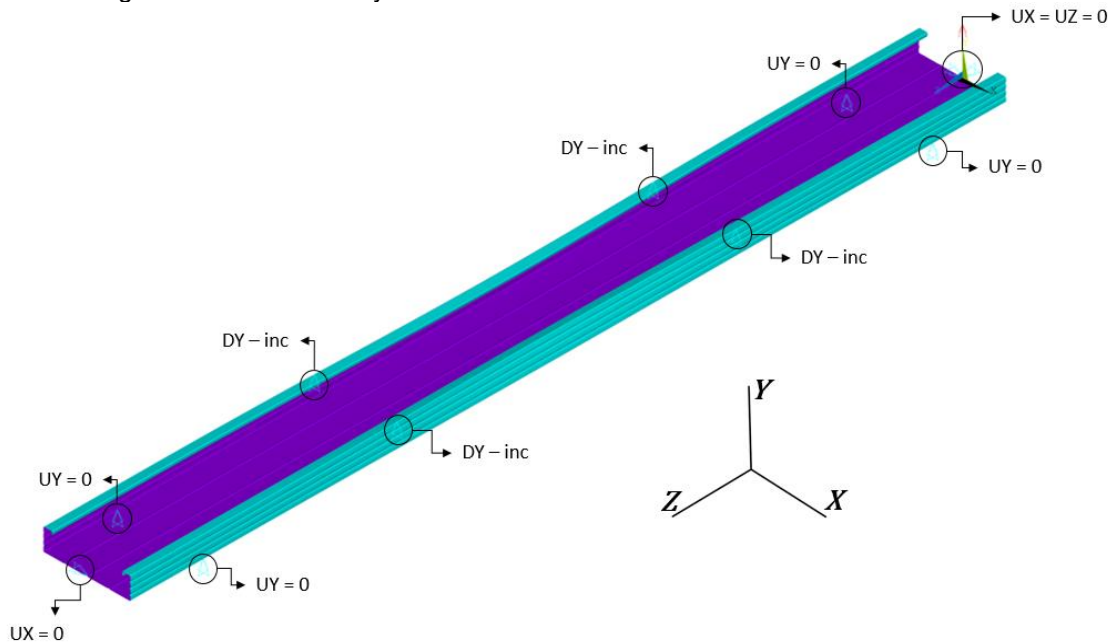
Source: author's own.

3.2.2.4 Confrontation of numerical and experimental results of Candido (2020, in progress)

In this sub-section, both finite element and theoretical predictions are confronted with the experimental data of Candido (2020, in progress).

Table 3.11 presents comparisons between finite element and DSM predictions with the measured data for ultimate moment capacities ($M_{u,FE}$, $M_{Rk,DSM}$ and $M_{u,exp}$, respectively). Good agreement was found between finite element and experimental strength predictions with a mean $M_{u,FE}/M_{u,exp}$ ratio of 0.93. In addition, finite element and experimental failure modes presented similar behaviours, as shown in Figure 3.28 to Figure 3.30.

DSM predictions for flexural strength ($M_{Rk,DSM}$) were also close to those attained experimentally values ($M_{u,exp}$) with an average ratio $M_{Rk,DSM}/M_{u,exp}$ of 0.99. In this case, however, with a high coefficient of variance (COV), of about 16.5 %, due to the high deviation found for the flexural strength of the 1.0 m beams. As shown in Figure 3.28, the failure mode observed for the P1.0 specimen tests was predominantly caused by load point crippling and distortion of the support cross-section. The theoretical predictions for this case, on the other hand, considered only the ultimate limits related to bending, differently to those observed in the tests. Therefore, the results of P1.0 specimens could not be compared to the DSM predictions, leading the

average flexural ratio and COV to 0.87 and 2.08%, respectively, indicating the actual accuracy of the DSM to predict the ultimate bending moment of the beams.

Table 3.11 — Summary of comparisons between numerical and test results.

Specimen	$M_{u,FE}/M_{u,exp}$	$M_{Rk,DSM}/M_{u,exp}$
P1.0a	0.99	1.26
P1.0b	0.91	1.16
P1.4a	0.89	0.90
P1.4b	0.88	0.89
P1.8a	1.01	0.87
P1.8b	0.99	0.85
Average	**0.95**	**0.99**
COV	**0.05**	**0.16**

Figure 3.27 — Confrontation of the load-displacement response obtained from finite element analysis and experimental tests of Candido (2020, in progress).
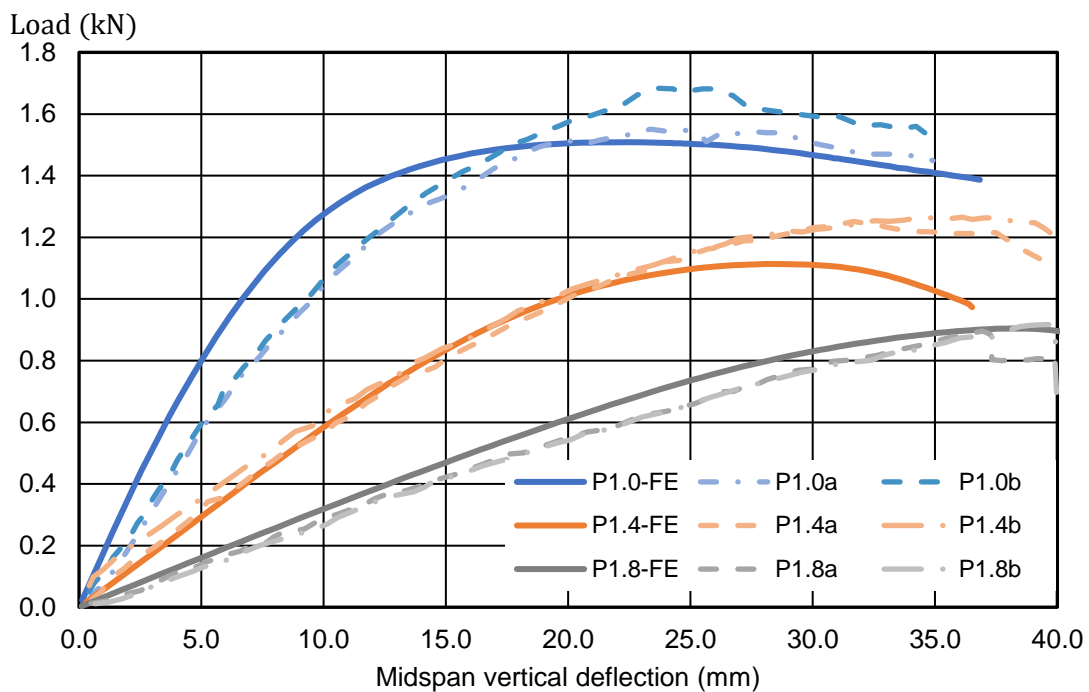
Source: author's own.

Figure 3.28 — Comparison of typical observed failure mode from test and numerical analysis for specimens P1.0.
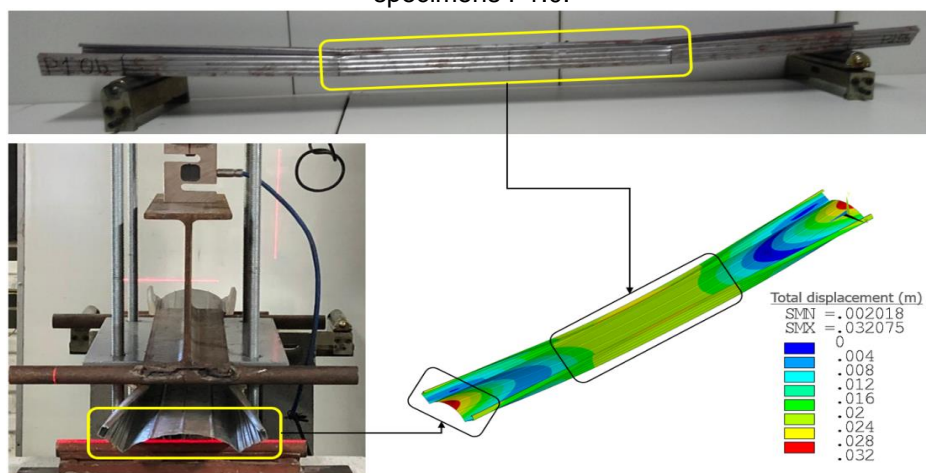
Source: author's own.

Figure 3.29 — Comparison of typical observed failure mode from test and numerical analysis for specimens P1.4.
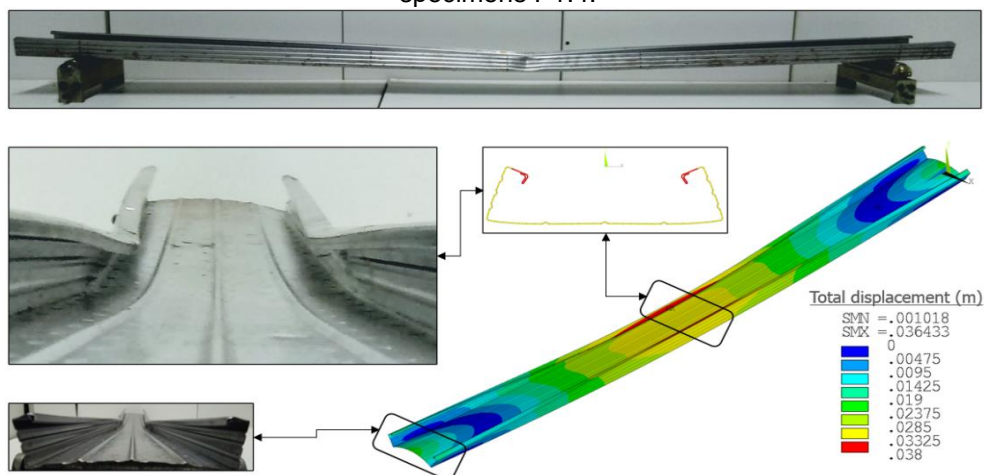
Source: author's own.

Figure 3.30 — Comparison of typical observed failure mode from test and numerical analysis for specimens with 1.8 m of free span length.
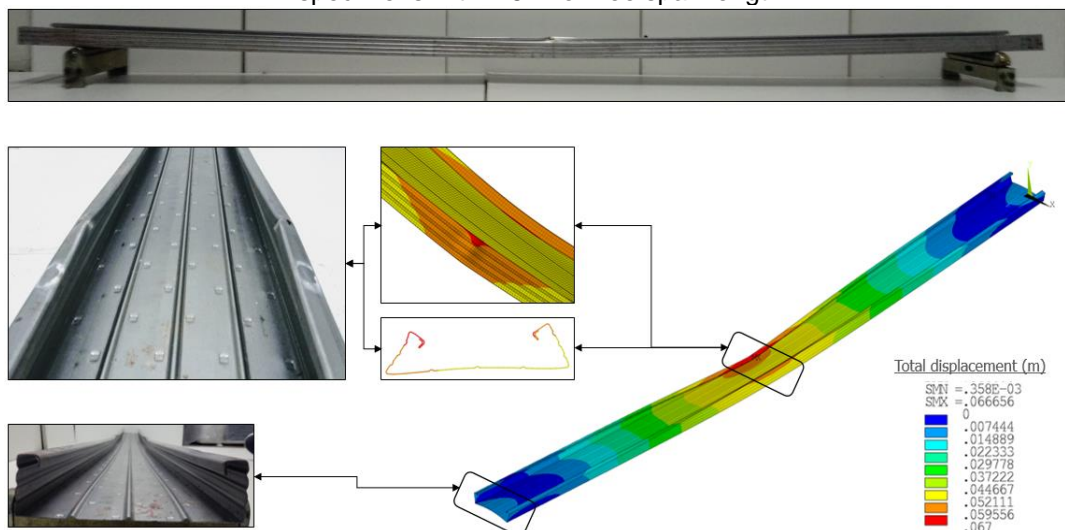
Source: author's own.

3.3   Finite element modelling of the Trelifácil® solution

As mentioned earlier, the finite element model developed to simulate the entire configuration of the Trelifácil® solution, i.e., a trussed girder attached to a cold-formed steel member, could not be validated against measured data, since they are not yet available in the literature. Hence, this section aims to present a proposal for modelling the Trelifácil® solution. The following sections describe the basic features of the finite element model developed for the Trelifácil® solution, that is: boundary condition and loading position, mesh and element discretization, material models, initial geometrical imperfections and solution scheme. Then, a study of the interaction between the trussed reinforcement and the cold-formed steel member is presented.

3.3.1 Basic features of the Trelifácil® solution finite element model

First of all, similar techniques used to model the cold-formed steel beams of Candido (2020, in progress) are employed in this study. In summary, a finite element mesh of 4 mm linear shell elements with reduced integration (SHELL181) is used to represent the CFS member. Also, the boundary condition and loading positions used in the analysis are similar to those shown in Figure 3.26. The multilinear isotropic hardening material model presented on the previous section is used to model the stress-strain behaviour of the steel formworks. Moreover, Full Newton-Raphson method solution scheme with nonlinear stabilisation (STABILIZE) was employed to solve the nonlinear analyses for the model of trussed girder coupled to the CFS member. In what follows, a brief description of the finite modelling techniques implemented to include the trussed girder in the finite element model developed for the cold-formed steel member is presented.

Beam elements with six degree of freedom (BEAM188) at each node are used to discretise geometry of the trussed girder. The reason for this element choice is to allow the interaction study of translation (in X, Y and Z directions) and rotation (about X, Y and Z directions) degrees of freedom between both trussed girder and CFS member. According to ANSYS® theory manual, the beam element BEAM188 is based on Timoshenko beam theory, which includes shear-deformation effects, and can be modelled with linear, quadratic or cubic shape functions. This element also allows large rotation and/or large strain, nonlinear behaviour and is compatible with nonlinear material models.

In this research, BEAM188 elements with linear shape function are used. The finite element mesh is created with 11 elements for diagonal chords and 22 elements for top and bottom chords between connection points, as shown in Figure 3.31. An elastic perfectly-plastic material model is implemented to simulate the trussed girder steel stress-strain behaviour. Material properties are adopted in accordance with the Brazilian standard for steel used in reinforced concrete structures, ABNT NBR 7850:2007. Therefore, a density of 7850 kg/m³ and a yield stress of 600 MPa are adopted, since this material features CA-60 steel rebar. The values for elastic modulus are not mentioned in this standard. Hence, a value of 210 GPa is assumed for this property, based on recommendations from ABNT NBR 6118:2016 (Brazilian design guide for concrete structures), and a Poisson's ratio equal to 0.3, usually adopted for metallic materials.

Figure 3.31 — Finite element model for the entire configuration of the Trelifácil® solution.
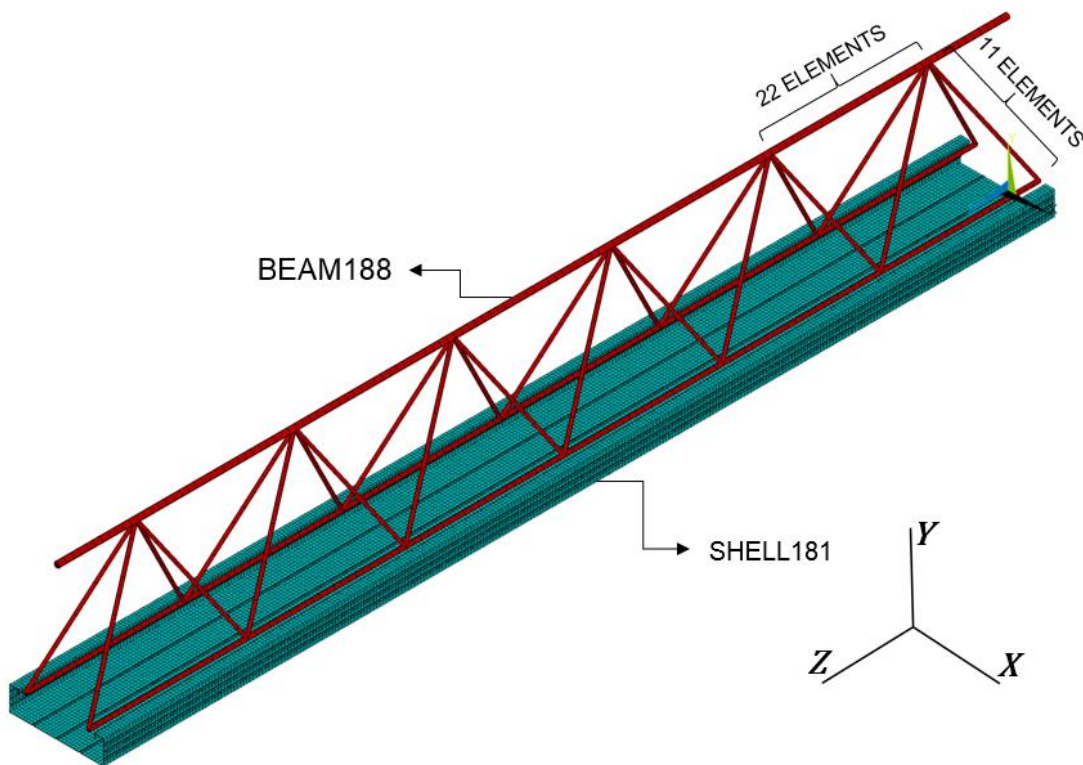
Source: author's own.

3.3.2 Sensitivity study of the interaction between trussed girder and cold-formed steel member

As shown in Figure 3.32 and mentioned before, the trussed girder and cold-formed steel formwork are connected to each other via plastic spacers. As an

alternative for modelling plastic spacers, the strategy employed herein to simulate their influence on the structural system was to couple the degrees of freedom (DOF) of nodes positioned near the connected region. As shown in Figure 3.32, the bottom chords of the trussed girder are fixed on the plastic spacers, which in turn are fixed on the steel formwork. It is expected that vertical displacements (UY) can be transferred from the nodes on the web of the steel member to nodes along the bottom chord of the trussed girder. Similarly, horizontal displacements in the transversal direction (UX) can be linked between nodes of bottom chords and the steel member flange, where the plastic spacers are fixed. Therefore, the study described in this section aims to present the finite element model sensitivity to the amount of coupled DOF. To this end, three nonlinear analyses are conducted to investigate two different aspects:

a) whether to (i) exclude or (ii) include compatibility of the rotational degrees of freedom (ROTZ and ROTX) between nodes of the trussed girder and formwork in regions connected by plastic spacers, as shown in Figure 3.32.

b) consideration of (iii) full or (i and ii) no interaction of translations in the longitudinal direction (UZ) promoted by the plastic spacers.

Figure 3.33 shows the boundary conditions, loading position and sets of coupled DOF applied to the sensitivity studies of the Trelifácil® solution finite element model. Nine sets of coupled DOF are applied at distances of 150 mm along the length of the CFS member. Although the manufacturer recommends a distance of 330 mm between plastic spacers, shorter spacing was applied to promote more interaction between the components of the Trelifácil® solution. In addition, Figure 3.33 presents the FE model with only transversal DOF couples (i.e., UX and UY) in the region of the plastic spacers, which corresponds to investigation (i). On the second case, labelled as (ii), rotations about X and Z axis (ROTX and ROTZ) are coupled and boundary conditions are identical to case (i), as shown in Figure 3.33. Alternatively, on case (iii) the boundary conditions are slightly changed. Since the longitudinal displacements are coupled between trussed girder and CFS member nodes, the imposed restraint in the Z-direction applied to the node on the top chord at midspan is removed. This restraint was originally applied to prevent the trussed girder from undergoing rigid body motion in the finite element models of the cases (i) and (ii).

Figure 3.32 — Illustration of three possible node coupling to assess the interaction between trussed girder and CFS formwork provided by plastic spacers.

Source: author's own.

Figure 3.33 — Boundary conditions, loading position and sets of coupled degrees-of-freedom (DOF) applied to the sensitivity studies of the Trelifácil® solution finite element model.

Source: author's own.

The load-displacement responses of the finite element models are shown in Figure 3.34. It was observed that the composite action between cold-formed steel beam and trussed girder was more sensitive to the connection of longitudinal

displacements (UZ) than rotational DOF (ROTX and ROTZ). A quantitative analysis can be carried out using Figure 3.35, where the ultimate moment capacity $M_{u,FE}$ and stiffness $(EI)_{FE}$ of cases (ii) and (iii) are normalised by the ultimate moment capacity $M_{u,FE,i}$ and stiffness $(EI)_{FE,i}$ of case (i), i.e., an equivalent system without coupling the longitudinal displacements (UZ) and rotational degrees-of-freedom (ROTX and ROTZ). Whereas the flexural capacity and stiffness of the FE model (iii) increased more than 50% relative to case (i), these gains were below 10% for case (ii). Therefore, it is conservative and reasonable to assume the coupled behaviour characterized by model (i), i.e., only the horizontal and vertical translational DOF (UX and UY) are coupled between the Trelifácil® solution components.

Figure 3.34 — Force *versus* displacement curves of the FE models (i), (ii) and (iii).

Source: author's own.
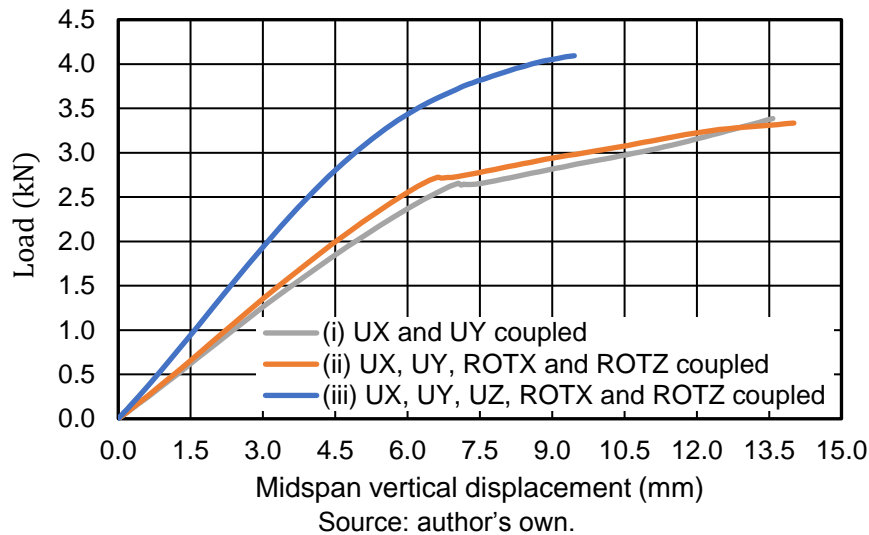
Figure 3.35 — Enhancements in moment capacity and flexural stiffness of the FE model (ii) and model (ii) relative to the FE model (i).

Source: author's own.
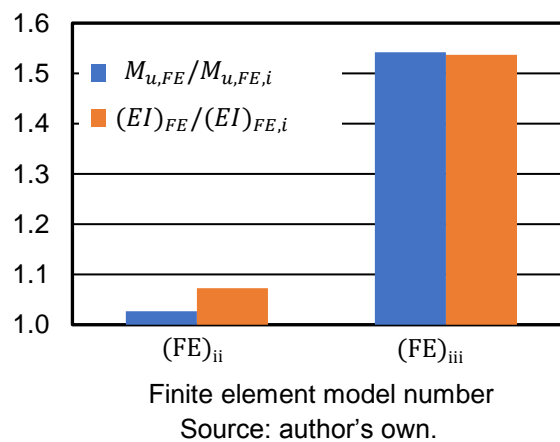
4 PARAMETRIC STUDY

4.1 Introduction

In this section, a variety of parametric studies is presented in order to extrapolate measured data and to examine the influence of span length, cross-section thickness, different trussed girder dimensions and spacing between plastic connectors on the flexural capacity and stiffness of the Trelifácil® solution. The next two sub-sections present the studies conducted for the Trelifácil® solution without and with the trussed girder attached to, namely specimen type 1 and specimen type 2, respectively.

4.2 Specimen type 1

Specimen type 1 is comprised only of the cold-formed steel beam employed in the Trelifácil® solution. For this specimen type, a parametric study is conducted to assess the influence of different span lengths and section thicknesses on the ultimate bending moment $M_{u,FE}$. In addition, these results are used to examine the accuracy of the Direct Strength Method (DSM) to predict such value designated here as M_{DSM}. As mentioned in section 2.1, the nominal resistant bending moment calculated with the DSM ($M_{u,DSM}$) relies on the determination of critical elastic moments related to flexural-torsional buckling (M_e), local buckling (M_ℓ) and distortional buckling (M_{dist}). In this research, those values are taken from the findings of Favarato et al. (2019b), which were determined using finite element buckling analysis and are shown in Table 4.1. To assess the accuracy of those values, critical elastic moments related to local and distortional buckling were also obtained using CUFSM (LI; SCHAFER, 2010; SCHAFER; ÁDÁNY, 2006) and good agreement was found between finite element and finite strip buckling moments. As such, the values from Favarato et al. (2019b) were used in the parametric studies to maintain the consistency with these previous studies.

Table 4.1 presents values of critical buckling moments for cold-formed steel members with eight different free span lengths (L), varying from 0.6 m to 2 m, for three different cross-sectional thicknesses, 0.65 mm, 0.8 mm, and 1.08 mm. Even though Favarato et al. (2019b) found maximum values of unpropped distances from 1.0 m to 1.2 m, depending on the materials and geometry adopted, longer spans will be assessed in order to evaluate the gains in flexural strength and stiffness when the trussed girder is coupled to the steel formwork. Thickness values greater than the

nominal thickness (i.e., 0.65 mm) are used to evaluate the sensitivity of the flexural behaviour to changes in cross-sectional dimensions. Therefore, a total of 24 beams are tested in this parametric study. The adopted modelling techniques are shown in section 4.2.1 and results are presented and discussed in section 4.2.2.

Table 4.1 — Critical buckling moments (in Nm) for the Trelifácil® solution cold-formed steel beam with different free span lengths and cross-sectional thicknesses.

L (m)	$t = 0.65$ mm			$t = 0.8$ mm			$t = 1.08$ mm		
	M_e	M_ℓ	M_{dist}	M_e	M_ℓ	M_{dist}	M_e	M_ℓ	M_{dist}
0.6	1151.7	1147.4	575.7	1498.2	1779.3	909.9	2034.3	3339.7	1792.0
0.8	1083.7	1147.7	645.9	1407.8	1755.0	967.3	1919.0	3295.8	1653.2
1	911.2	1180.8	598.7	1204.6	1742.0	899.8	1632.6	3280.7	1664.8
1.2	613.4	1154.9	588.4	870.6	1734.5	931.6	1287.5	3274.9	1661.5
1.4	537.2	1145.2	618.2	721.4	1730.2	912.8	1007.3	3270.5	1645.4
1.6	451.2	1147.0	591.8	588.1	1727.4	905.9	802.1	3266.3	1667.8
1.8	375.4	1115.1	590.5	482.8	1725.8	926.1	652.9	3264.4	1647.3
2	314.1	1113.9	604.5	401.9	1724.5	908.7	542.7	3263.3	1680.7
CUFSM	--	1117.1	612.9	--	1825.1	941.3	--	3486.3	1755.3

Source: adapted from (FAVARATO et al., 2019b).

4.2.1 Finite element modelling techniques adopted

In this parametric study, the validated finite element model developed to simulate the physical tests of Candido (2020, in progress) was altered to predict moment capacity in accordance with the Direct Strength Method.

The finite element models developed herein were validated against physical tests conducted by Candido (2020, in progress), which follows the recommendations of full cross-section bending tests prescribed by the European code for cold-formed steel structures, EN 1993-1-3:2004. This code establishes that "a pair of point loads should be applied to the specimen to produce a length under uniform bending moment at midspan of at least 0.2 x (span) but not more than 0.33 x (span)". In the experimental program, however, the distance between loading points were set equal to 0.46425 m for all tests. Therefore, this distance was altered to 0.33 x (span) for all numerical models of the parametric studies. Furthermore, to prevent rigid body motion, transversal horizontal displacements (U_x) are restrained at both ends and longitudinal displacements (U_z) at one end. Figure 4.1 shows an overall view of the boundary conditions and loading position used in these parametric studies. The remaining features of the finite element model are equal to those adopted in the validated model presented in section 3.2.2.

Figure 4.1 — Boundary condition and loading position used in the parametric studies.
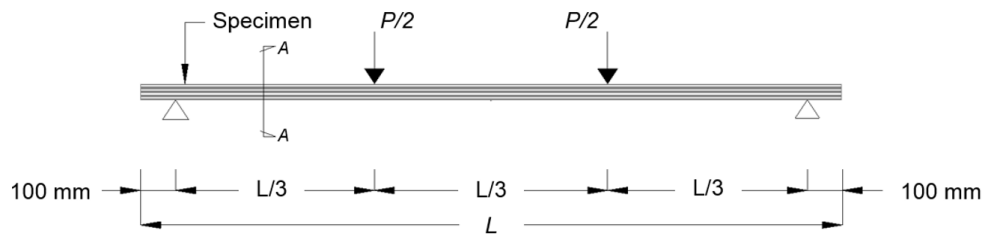
Source: author's own.

4.2.2 Results and discussion

Results of parametric studies are examined in the context of comparisons between theoretical (DSM) and finite element predictions of moment capacity, which are summarised in Table 4.2 and displayed in Figure 4.2. Overall, the moment capacity was higher for members with thicker cross-sections and it rises more gradually for smaller cross-section thicknesses. Further, for all cross-section thicknesses assessed, this value tends to remain unaltered for longer span lengths.

Table 4.2 — Results of parametric studies in terms of moment capacity.

L	$t = 0.65\ mm$			$t = 0.80\ mm$			$t = 1.08\ mm$		
	$M_{u,FE}$	M_{DSM}	$\dfrac{M_{DSM}}{M_{u,FE}}$	$M_{u,FE}$	M_{DSM}	$\dfrac{M_{DSM}}{M_{u,FE}}$	$M_{u,FE}$	M_{DSM}	$\dfrac{M_{DSM}}{M_{u,FE}}$
(m)	(kNm)	(kNm)		(kNm)	(kNm)		(kNm)	(kNm)	
0.6	0.19	0.34	1.83	0.26	0.45	1.72	0.44	0.63	1.45
0.8	0.21	0.35	1.70	0.30	0.46	1.53	0.51	0.63	1.24
1.0	0.23	0.35	1.48	0.34	0.45	1.22	0.52	0.63	1.19
1.2	0.26	0.34	1.32	0.37	0.44	1.26	0.51	0.60	1.19
1.4	0.28	0.34	1.19	0.35	0.43	1.25	0.50	0.58	1.15
1.6	0.27	0.32	1.21	0.34	0.40	1.20	0.50	0.55	1.09
1.8	0.26	0.30	1.17	0.34	0.38	1.13	0.50	0.51	1.02
2.0	0.25	0.28	1.10	0.33	0.35	1.05	0.50	0.47	0.94
Mean			1.37			1.30			1.16
Standard deviation			0.22			0.17			0.11

Figure 4.2 — Influence of free span length and cross-section thickness on moment capacity of the Trelifácil® CFS member.
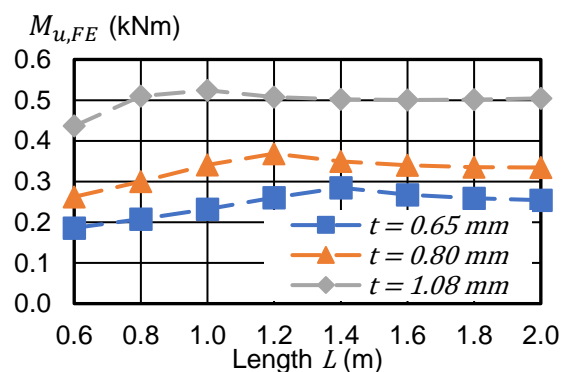
Source: author's own.

Comparisons between theoretical (DSM) and finite element results in terms of moment capacity are shown in Figure 4.3. On one hand, it seems that the DSM overestimates the moment capacity of the CFS member used in the Trelifácil® solution for shorter beam lengths. On the other hand, it is important to note that for shorter beam lengths the specimens undergo ultimate limit states not included in the DSM predictions, such as load point crippling and limit states related to combined shear and bending. However, as span lengths are increased, results gradually converge to the finite element predictions.

Figure 4.3 — Comparison of the flexural capacity and midspan vertical deflection obtained from DSM and FE analysis.
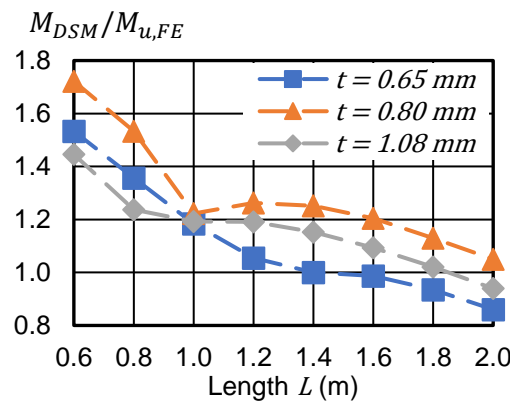
Source: author's own.

4.3 Specimen type 2

For the specimen with the trussed girder attached to it, named specimen type 2 in this research, a series of parametric studies is conducted to investigate the influence of length and thickness of the cold-formed steel beam, different trussed girders and the spacing between plastic connectors on the flexural behaviour of the structural member. The results are examined in the context of gains in flexural capacity and stiffness.

The modelling techniques implemented here were similar to those described in section 3.3. Thus, differently from the parametric studies of specimen type 1, the span of uniform bending moment is equal to 0.46425 m and the beam cross-section thickness equal to 0.52 mm. Conservatively, it is assumed for the degree of coupled action between the Trelifácil® solution components that no longitudinal displacements (UZ) and rotational DOF (ROTX and ROTZ) are transferred by the plastic spacers, as presented in section 3.3.2. Due to the number of parameters, two sets of parametric studies are performed.

First, nine structural systems are evaluated, consisting of three distinct span lengths and three distinct trussed girders. The beam span lengths are equal to the physical test specimens of Candido (2020, in progress), i.e., 1.0 m, 1.4 m and 1.8 m. Trussed girder types with height of 120 mm (TR12645) and 160 mm (TR16745) were also selected in conformity with the research of Candido (2020, in progress). The 300 mm high trussed girder (TR30856) was then included in the study to assess a wider height range. Table 4.3 presents the designation used for each finite element model developed in this first investigation.

Table 4.3 — Summary of examined structural systems of the first set of parametric studies.

	$L = 1.0$ m	$L = 1.4$ m	$L = 1.8$ m
Trussed girder TR12645	P1.0TR12645	P1.4TR12645	P1.8TR12645
Trussed girder TR16745	P1.0TR16745	P1.4TR16745	P1.8TR16745
Trussed girder TR30856	P1.0TR30845	P1.4TR30845	P1.8TR30845

The second parametric study conducted aims to assess the influence of the number of plastic spacers (i.e., the distance between plastic spacers) along the beam length on the flexural capacity and stiffness of the structural system. Once again, beams with span lengths of 1.0 m, 1.4 m and 1.8 m are evaluated. The previous parametric studies were conducted with nine plastic spacers along the length of the beam. Then, the number of plastic spacers is doubled to eighteen plastic spacers to perform this comparative study. Table 4.4 presents the designation used for each FE model developed in this second investigation. Note that only one type of trussed girder is used, which has an intermediate height amongst those available.

Table 4.4 — Summary of examined structural systems of the second set of parametric studies.

	$L = 1.0$ m	$L = 1.4$ m	$L = 1.8$ m
9 plastic spacers	P1.0TR16745_9S	P1.4TR16745_9S	P1.8TR16745_9S
18 plastic spacers	P1.0TR16745_18S	P1.4TR16745_18S	P1.8TR16745_18S

4.3.1 Results and discussion

For the two sets of parametric studies conducted, results are examined in the context of load-displacement response and of gains in flexural capacity $M_{u,FE}$ and stiffness $(EI)_{FE}$ relative to the correspondent structural system without trussed girder. To this end, these results are normalised by the moment capacity $M_{u,FE,CFS}$ and flexural stiffness $(EI)_{FE,CFS}$ of the finite element models comprised only of the CFS member. In what follows, results are presented and discussed for each set of investigations

performed.

Figure 4.4 shows the load-displacement responses of the first set of parametric studies conducted. Comparing the curves, it is observed that the moment capacity and flexural stiffness increased with the introduction of the trussed girder into the CFS member. In contrast, the structural system loses its ductility when the trussed girder is included. Quantitatively, these conclusions are reinforced by the results shown in Figure 4.5. Maximum moment capacity was enhanced by almost 100 per cent for specimen P1.8TR12645 and a minimum increase of over 50 per cent is observed for specimen P1.4TR30856. Comparing the different trussed girders evaluated, the moment capacity of specimens with longer span lengths (1.4 m and 1.8 m) decreased when the tallest trussed girder (TR30856) was used. The flexural capacity of shorter members, in turn, presented a gradual rise with the increments of trussed girder height. In contrast, flexural stiffness either increased or remained the same as changes in trussed girder height were introduced. Further, longer beam lengths presented higher stiffness enhancements, reaching over 400 per cent for the specimen P1.8TR30856. Overall, these finite element model predictions suggest that the flexural capacity and stiffness of the Trelifácil® solution are substantially increased by coupling vertical (UY) and transversal (UX) displacements between its components.

Figure 4.4 — Influence of the trussed girder on the finite element load *versus* displacement responses of the Trelifácil® solution.
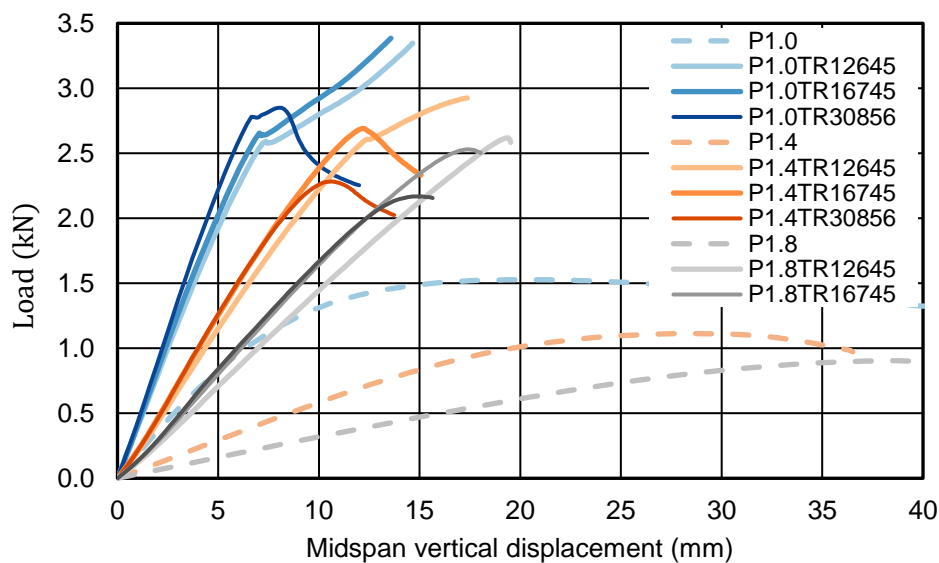
Source: author's own.

Figure 4.6 shows the load-displacement response of the finite element models in which the number of plastic spacers along beam length was varied. The graph

indicates that both flexural capacity and stiffness are sensitive to the number of plastic spacers in the cold-formed steel member. Numerically, as shown in Figure 4.7, the gains in moment capacity were in a range of 60 to 100 per cent, while the stiffness enhancements increased by more than 500 per cent for the longer specimen. Comparing the gains in flexural strength and stiffness obtained by increasing the number of plastic spacers with those resulting from changes in trussed girder height, the former brought greater benefits, except for the shorter specimen flexural capacity, which percentage points grew similarly in both cases.

Figure 4.5 — Enhancements in flexural capacity and stiffness of the Trelifácil® solution relative to the corresponding CFS member without trussed girder included.

Source: author's own.

Figure 4.6 — Influence of the number of plastic spacers on the finite element load *versus* displacement responses of the Trelifácil® solution.
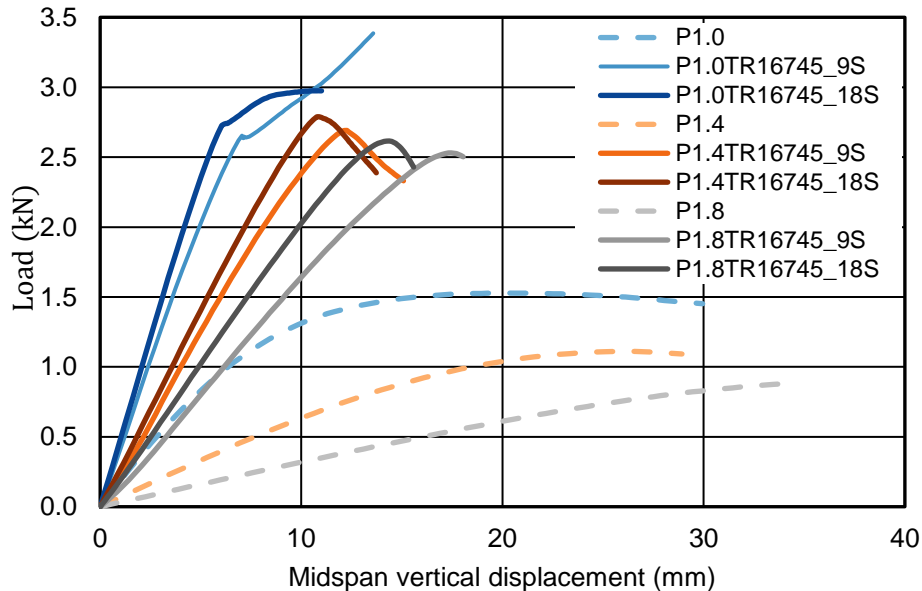
Source: author's own.

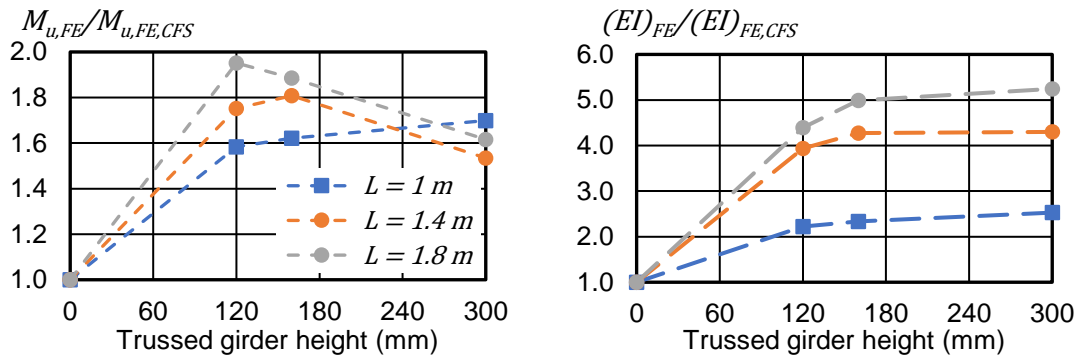Figure 4.7 — Enhancements in flexural capacity and stiffness of the Trelifácil® solution with the increase of the plastic spacer quantity along the beam length.
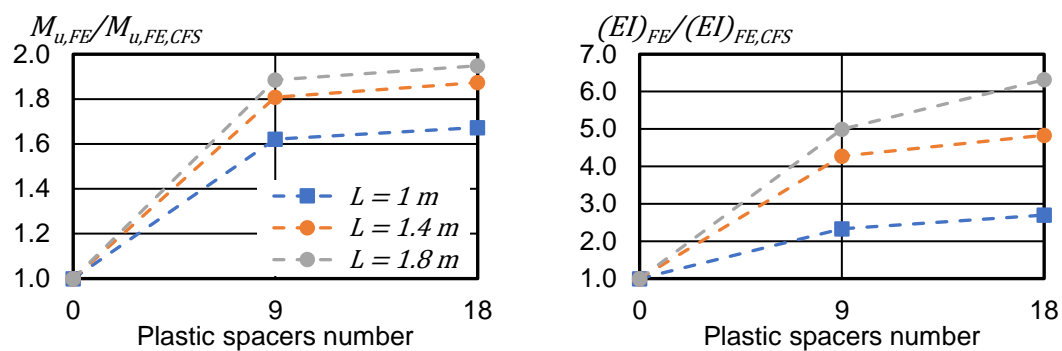
Source: author's own.

5 CONCLUSIONS AND FUTURE RESEARCH

5.1 Conclusions

Although the Trelifácil® solution has shown potential for replacing lattice reinforced concrete girders, it is only recently that researchers have started looking into the design of these structural elements, as well as into the feasibility of considering the composite action between their components within the flooring system during construction and in service. Therefore, in this research finite element models were developed using ANSYS® 2020R1 to predict the flexural behaviour of this structural element.

A variety of sensitivity studies, described in detail in Chapter 3, have been conducted to evaluate the accuracy of the finite element modelling techniques used to simulate the mechanical behaviour of the cold-formed steel beam employed in the Trelifácil® solution under four-point bending. The examined parameters consist of boundary conditions, loading position, element and mesh choice, initial geometrical imperfections, solution solver scheme and material model. Numerical analyses with the finite element method and the Direct Strength Method could satisfactorily predict the results found with the flexural tests conducted by Gomes et al. (2019) and Candido (2020, in progress). From the investigations it follows that:

a) four-node linear shell element (SHELL181) and eight-node quadratic shell element (SHELL281) presented similar behaviour when the nominal element size is smaller than 5 mm;

b) ultimate bending moment responses presented little sensitivity to initial geometrical imperfections;

c) arc-length (Riks) method and Full Newton-Raphson method with artificial damping, both with displacement control, can predict the geometrical and material nonlinear load-displacement response of the finite element models developed. However, only artificial damping could capture the peak load and post-collapse response when the trussed girder was coupled to the cold-formed steel member;

d) satisfactory results were found with a material model comprised by the basic Ramberg-Osgood stress-strain relationship up to 0.2% proof stress followed by a straight line with a constant slope expressed as a fraction of the initial elastic modulus.

Thereafter, a proposal of finite element model to simulate the complete configuration of the Trelifácil® solution was presented in Chapter 3. These initial investigations aimed to address the sensitivity of the model to the degree of coupled action between trussed girder and cold-formed steel formwork. Overall, results showed that coupling the longitudinal translational DOF (UZ) between the Trelifácil® solution components may increase the strength and stiffness of the system by approximately 50 per cent.

Finally, parametric studies have been conducted in order to examine the structural performance of the two finite element models developed. In addition, the accuracy of the Direct Strength Method to predict the flexural strength of the cold-formed steel member about the minor axis of inertia was assessed for different span lengths and cross-section thicknesses. The results of the parametric studies suggest that:

a) moment capacity of the cold-formed steel beams tends to a plateau with the increase of span length;

b) considering the composite action in the proposed finite element model of the Trelifácil® solution substantially increased its strength and stiffness, which would lead to longer unpropped span lengths for the flooring system during construction. Further, these gains are further increased when either the trussed girder height is increased or the spacing between plastic connectors is reduced.

The main conclusions that can be drawn from this research are:

a) the prediction of flexural behaviour by geometric and material nonlinear finite element analysis for the cold-formed steel member of the Trelifácil® solution is highly sensitive to boundary conditions, loading position, element choice, mesh density, plasticity model and solution scheme. Based on literature review, this research presented possible modelling techniques for each of these major issues;

b) the gains in strength and stiffness found with the suggested finite element model for the entire configuration of the Trelifácil® solution reinforced the potential of this structural system that can be derived through the consideration of coupled action between its components.

5.2 Suggestions for future research

Potential areas of future research include investigation of the behaviour of these beams under loading and boundary conditions as used in service or even under extreme loads. Continuous beams under uniformly distributed loading would represent, for instance, a real condition of the system, which involves the use of propping to support the slab until it gains enough strength to support itself. This subject would also be useful to investigate the current analytical formulations for the design of continuous beams subjected to minor axis bending with stiffeners under tension.

Additionally, since the consideration of coupled action between the Trelifácil® solution components were promising, it is suggested for future researchers to focus on innovative means to optimize the Trelifácil® solution geometry so that material usage can be reduced. Further, the exploitation of the composite action between cold-formed steel and concrete may also present enhancements to the capacity of the floor system capacity after concrete curing, which can be addressed by the development of sophisticated finite element models validated by physical tests.

REFERENCES

ABAMBRES, M.; QUACH, W.-M. Residual stresses in steel members: a review of available analytical expressions. **International Journal of Structural Integrity**, v. 7, n. 1, p. 70–94, fev. 2016.

AMERICAN IRON AND STEEL INSTITUTE. **Direct Strength Method Design Guide.** Washington, D.C.: AISI, 2006.

AMOUZEGAR, H.; SCHAFER, B. W.; TOOTKABONI, M. An incremental numerical method for calculation of residual stresses and strains in cold-formed steel members. **Thin-Walled Structures**, v. 106, p. 61–74, 1 set. 2016.

ANBARASU, M. Local-distortional buckling interaction on cold-formed steel lipped channel beams. **Thin-Walled Structures**, v. 98, p. 351–359, 1 jan. 2016.

ANSYS® 2020R1. **ANSYS® Academic Research Mechanical,** Release 2020R1.

ARCELORMITTAL. **Catálogo Trelifácil®**, 2017a. Disponível em: <https://brasil.arcelormittal.com/files/produtos-catalogos/d669932b-07fd-4fff-863c-230991986230>. Acesso em: 24 fev. 2019.

ARCELORMITTAL. **Trelifácil®: muito mais facilidade para construir lajes. | ArcelorMittal**, 2017b. Disponível em: <http://blog.arcelormittal.com.br/trelifacil-muito-mais-facilidade-para-construir-lajes/>. Acesso em: 24 fev. 2019.

ARRAYAGO, I.; REAL, E.; GARDNER, L. Description of stress-strain curves for stainless steel alloys. **Materials and Design**, v. 87, p. 540–552, 15 dez. 2015.

AUSTRALIAN STANDARD. **AS 4084:** Steel storage rackling. 2012.

ASSOCIAÇÃO BRASILEIRA DE NORMAS TÉCNICAS. **ABNT NBR 14762:** Design of cold-formed steel structures. Rio de Janeiro: ABNT, 2010.

ASSOCIAÇÃO BRASILEIRA DE NORMAS TÉCNICAS. **ABNT NBR 14859-2:** Pre-fabricated concrete slabs. Part 2: Inert elements for filling and mold — Requirements. Rio de Janeiro: ABNT, 2016.

ASSOCIAÇÃO BRASILEIRA DE NORMAS TÉCNICAS. **ABNT NBR 14859-3:** Pre-fabricated concrete slabs. Part 3: Pre-fabricated steel lattice reinforcement for concrete structures — Requirements. Rio de Janeiro: ABNT, 2017.

ASSOCIAÇÃO BRASILEIRA DE NORMAS TÉCNICAS. **ABNT NBR 15696:** Formworks and shoring for concrete structures — Bill, dimensioning and procedures executives. Rio de Janeiro: ABNT, 2009.

ASSOCIAÇÃO BRASILEIRA DE NORMAS TÉCNICAS. **ABNT NBR 6118:** Design of concrete structures — Procedure. Rio de Janeiro: ABNT, 2014.

ASSOCIAÇÃO BRASILEIRA DE NORMAS TÉCNICAS. **ABNT NBR 7480:** Steel for the reinforcement of concrete structures — Specification. Rio de Janeiro: ABNT, 2007.

ASSOCIAÇÃO BRASILEIRA DE NORMAS TÉCNICAS. **ABNT NBR 8800:** Design of steel and composite structures for building. Rio de Janeiro: ABNT, 2008.

BATISTA, E. DE M.; RODRIGUES, F. G. RESIDUAL STRESS MEASUREMENTS ON COLD-FORMED PROFILES. **Experimental Techniques**, v. 16, n. 5, p. 25–29, 15 dez. 1992.

BEBIANO, R.; CAMOTIM, D.; GONÇALVES, R. GBTUL 2.0 − A second-generation code for the GBT-based buckling and vibration analysis of thin-walled members. **Thin-Walled Structures**, v. 124, p. 235–257, 1 mar. 2018.

BELTRÃO, A. J. N. **Comportamento Estrutural de Lajes-mistas com Corrugações na Alma de Perfis de Chapa Dobrada**. Dissertação (Mestrado) – Departamento de Engenharia Civil, Pontifícia Universidade Católica do Rio de Janeiro, Rio de Janeiro, 2003.

BONADA, J. et al. Selection of the initial geometrical imperfection in nonlinear FE analysis of cold-formed steel rack columns. **Thin-Walled Structures**, v. 51, p. 99–111, 1 fev. 2012.

BRAZIER, L. G. On the flexure of thin cylindrical shells and other "thin" sections. **Proceedings of the Royal Society of London. Series A, Containing Papers of a Mathematical and Physical Character**, v. 116, n. 773, p. 104–114, 1 set. 1927.

CAIXETA, D. P. **Contribuição ao Estudo de Lajes Pré-Fabricadas com Vigas Treliçadas**. Dissertação (Mestrado) – Faculdade de Engenharia Civil, Universidade Estadual de Campinas, Campinas,1998.

CANDIDO, D. C. M. **Análise Experimental de Laje Nervurada Treliçada com Incorporação de Fôrma Intermitente em Perfil de Aço Formado a Frio**. Dissertação (Mestrado) – Departamento de Engenharia Civil, Universidade Federal do Espírito Santo, Vitória, 2020. In progress.

CARVALHO, R. C.; PARSEKIAN, G. A.; FIGUEIREDO FILHO, J R de; MACIEL, A. M. Estado da arte do cálculo das lajes pré-fabricadas com vigotas de concreto. **Encontro Nacional de Pesquisa-Projeto-Produção em Concreto Pré-moldado**, v. 2, 2005.

CHEN, W. F.; HAN, D. J. Plasticity for structural engineers. **Springer, New York.**, 1988.

CHODRAUI, G. M. B.; SHIFFERAW, Y.; MALITE, M.; SCHAFER, B. W. **Cold-formed Steel Angles under Axial Compression**. INTERNATIONAL SPECIALTY CONFERENCE ON COLD-FORMED STEEL STRUCTURES. **Anais**...Orlando, Florida: 2006.

CHOU, S. M.; CHAI, G. B.; LING, L. Finite element technique for design of stub columns. **Thin-Walled Structures**, v. 37, n. 2, p. 97–112, 1 jun. 2000.

CRISFIELD, M. A. **Non-linear Finite Element Analysis of Solids and Structures**, **Volume 1**. London: John Wiley and Sons, 1991.

DAT, D. T.; PEKÖZ, T. **The strength of cold-formed steel columns**. **Report no. 80-4.** Department of Structural Engineering, Cornel University, Ithaca, New York: 1980.

DAWSON, R.; WALKER, A. C. Post-Buckling of Geometrically Imperfect Plates. **Journal of the Structural Division, ASCE**, v. 98, n. 1, p. 75–94, 1972.

DEGTYAREV, V. V. Concentrated load distribution in corrugated steel decks: A parametric finite element study. **Engineering Structures**, v. 206, p. 110–158, 2020.

DINIS, P. B.; CAMOTIM, D. Local/distortional mode interaction in cold-formed steel lipped channel beams. **Thin-Walled Structures**, v. 48, n. 10–11, p. 771–785, 2010.

DINIS, P. B.; CAMOTIM, D. **Local/distortional/global buckling mode interaction in cold-formed steel lipped channel columns**. Proceedings of SSRC Annual Stability Conference. **Anais**...2009

DINIS, P. B.; CAMOTIM, D. **Post-buckling behavior of cold-formed steel lipped channel columns affected by distortional/global mode interaction**. Proceedings of SSRC Annual Stability Conference. **Anais**...2008

DOLAMUNE KANKANAMGE, N.; MAHENDRAN, M. Behaviour and design of cold-formed steel beams subject to lateraltorsional buckling. **Thin-Walled Structures**, v. 51, p. 25–38, 2012.

DROPPA JR., A. **Análise estrutural de lajes formadas por elementos pré-moldados tipo vigota com armação treliçada**. Dissertação (Mestrado) – Escola de Engenharia de São Carlos, Universidade de São Paulo, São Carlos, 1999.

DUBINA, D.; UNGUREANU, V. Effect of imperfections on numerical simulation of instability behaviour of cold-formed steel members. **Thin-Walled Structures**, v. 40, n. 3, p. 239–262, 1 mar. 2002.

ELLOBODY, E.; YOUNG, B. Behavior of cold-formed steel plain angle columns. **Journal of Structural Engineering**, v. 131, n. 3, p. 457–466, mar. 2005.

EUROPEAN COMMITTE FOR STANDARDIZATION. **EN 1993-1-6, Eurocode 3**: Design of Steel Structures - Part 1.6: strength and stability of shell structures. Brussels, Belgium: CEN, 2007.

FARZANIAN, S.; LOUHGHALAM, A.; SCHAFER, B. W.; TOOTKABONI, M. Geometric imperfection models for CFS structural members , Part I : Comparative review of current models. **Thin-Walled Structures**, 2019. Preprint.

FAVARATO, L. F. **DIMENSIONAMENTO DE LAJES COM VIGOTAS TRELIÇADAS COM FORMA EM PERFIL U FORMADO A FRIO**. Trabalho de Conclusão de Curso (Graduação) – Departamento de Engenharia Civil, Universidade Federal do Espírito Santo, Vitória, 2018.

FAVARATO, L. F.; CALENZANI, A. F. G.; VIANNA PIRES, J. C.; JUNGES, E.; FERRARETO, J. A. Evaluation of the resistance of trussed slabs with steel formwork in cold formed U profile. **Latin American Journal of Solids and Structures**, v. 16, n. 7 CILAMCE 2018, 18 jul. 2019b.

FAVARATO, L. F.; CANDIDO, D. C. M.; GOMES, A. V. S.; CALENZANI, A. F. G.; VIANNA, J. C.; FERRARETO, J. A. **Lateral-torsional buckling of cold-formed continuous beams with stiffened u sections bent about the axis of lower inertia**. CONSTRUMETAL 2019 - 8º Congresso Latino-Americano da Construção Metálica. **Anais**...São Paulo, SP, Brazil: 2019a.

FAVARATO, L.F., GOMES, A.V.S., CANDIDO, D.C.M., CALENZANI, A.F.G., VIANNA, J.C. AND FERRARETO, J.A. Proposition of a simplified analytical design procedure for lattice girder slabs with shuttering in cold-formed steel lipped channel section. **Revista IBRACON de Estruturas e Materiais**, v. 13, n. 5, p. 2020, 2020.

FERREIRA, T. R.; DE LIMA, M. C. V.; DELALIBERA, R. G. Otimização estrutural de lajes formadas por vigotas treliçadas com e sem protensão. **Ciencia y Engenharia/ Science and Engineering Journal**, v. 26, n. 2, p. 1–9, 1 jul. 2017.

GARDNER, L. **A new approach to structural stainless steel design**. Thesis (Doctor of Philosophy) – Department of Civil and Environmental Engineering, Imperial College London, London, 2002.

GARDNER, L.; BU, Y.; FRANCIS, P.; BADDOO, N. R.; CASHELL, K. A.; MCCANN, F. Elevated temperature material properties of stainless steel reinforcing bar. **Construction and Building Materials**, v. 114, p. 977–997, 1 jul. 2016.

GARDNER, L.; ASHRAF, M. Structural design for non-linear metallic materials. **Engineering Structures**, v. 28, n. 6, p. 926–934, 1 maio 2006.

GASPAR, R. **Análise da segurança estrutural das lajes pré-fabricadas na fase de construção.** Dissertação (Mestrado) – Escola de Engenharia de São Carlos, Universidade de São Paulo, São Carlos, 1997.

GOMES, A. V. S.; CANDIDO, D. C. M.; FAVARATO, L. F.; FERRARETO, J. A.; VIANNA, J. C.; CALENZANI, A. F. G. **Numerical and experimental study of a cold formed steel profile employed in steel-concrete composite ribbed slabs**. CONSTRUMETAL 2019 - 8º Congresso Latino-Americano da Construção Metálica. **Anais**...São Paulo, SP, Brazil: 2019.

HAIDARALI, M. R. **Local and Distortional buckling behaviour of cold-formed steel Z section beams**. Thesis (Doctor of Philosophy) – Department of Civil and Environmental Engineering, Imperial College London, London, 2011.

HAIDARALI, M. R.; NETHERCOT, D. A. Finite element modelling of cold-formed steel beams under local buckling or combined local/distortional buckling. **Thin-Walled Structures**, v. 49, n. 12, p. 1554–1562, 1 dez. 2011.

HANCOCK, G. J.; KWON, Y. B.; BERNARD, E. S. Strength design curves for thin-

walled sections undergoing distortional buckling. **Journal of Constructional Steel Research**, v. 31, n. 2–3, p. 169–186, 1 jan. 1994.

HUI, C. **Moment Redistribution in ColddFormed Steel Purlin Systems**. Thesis (Doctor of Philosophy) – Department of Civil and Environmental Engineering, Imperial College London, London, 2014.

INGVARSSON, L. **Cold-forming Residual Stresses Effect on Buckling**. Proceedings of the Third International Specialty Conference on Cold-Formed Steel Structures. **Anais**...University of Missouri-Rolla, St Louis, MO: 1975.

JANDERA, M.; GARDNER, L.; MACHACEK, J. Residual stresses in cold-rolled stainless steel hollow sections. **Journal of Constructional Steel Research**, v. 64, n. 11, p. 1255–1263, 1 nov. 2008.

JAVARONI, C. E. **Estruturas de Aço: Dimensionamento de Perfis de Aço Formados a Frio**. 1. ed. Rio de Janeiro: Elsevier, 2015.

KUMAR, N.; SAHOO, D. R. Optimization of lip length and aspect ratio of thin channel sections under minor axes bending. **Thin-Walled Structures**, v. 100, p. 158–169, 2016.

KYVELOU, P. **Structural behaviour of composite cold-formed steel systems**. Thesis (Doctor of Philosophy) – Department of Civil and Environmental Engineering, Imperial College London, London, 2017.

KYVELOU, P.; GARDNER, L.; NETHERCOT, D. A. Finite element modelling of composite cold-formed steel flooring systems. **Engineering Structures**, v. 158, p. 28–42, 1 mar. 2018.

LAÍM, L.; RODRIGUES, J. P. C.; SILVA, L. S. DA. Experimental and numerical analysis on the structural behaviour of cold-formed steel beams. **Thin-Walled Structures**, v. 72, p. 1–13, 2013.

LANDESMANN, A.; CAMOTIM, D. On the Direct Strength Method (DSM) design of cold-formed steel columns against distortional failure. **Thin-Walled Structures**, v. 67, p. 168–187, 1 jun. 2013.

LECCE, M.; RASMUSSEN, K. Distortional buckling of cold-formed stainless steel sections: Finite-element modeling and design. **Journal of Structural Engineering**, v. 132, n. 4, p. 505–514, abr. 2006.

LI, Z.; SCHAFER, B. Buckling Analysis of Cold-formed Steel Members with General Boundary Conditions Using CUFSM Conventional and Constrained Finite Strip Methods. **International Specialty Conference on Cold-Formed Steel Structures**, 3 nov. 2010.

LIU, G.-R.; QUEK, S. S. **The finite element method: a practical course**. Butterworth-Heinemann, 2013.

MAGALHÃES, F. L. **Estudo dos momentos fletores negativos nos apoios de lajes formadas por elementos pré-moldados tipo nervuras com armação treliçada**. Dissertação (Mestrado) – Escola de Engenharia de São Carlos, Universidade de São Paulo, São Carlos, 2001.

MAIA, W. F. et al. Experimental and numerical investigation of cold-formed steel double angle members under compression. **Journal of Constructional Steel Research**, v. 121, p. 398–412, 1 jun. 2016.

MARTINS, A. D. et al. On the mechanics of local-distortional interaction in thin-walled lipped channel columns. **Thin-Walled Structures**, v. 125, n. May, p. 187–202, 2018.

MARTINS, A. D.; CAMOTIM, D.; DINIS, P. B. Local-distortional interaction in cold-formed steel beams: Behaviour, strength and DSM design. **Thin-Walled Structures**, v. 119, n. June, p. 879–901, 2017.

MATSUBARA, G. Y.; BATISTA, E. DE M.; SALLES, G. C. Lipped channel cold-formed steel columns under local-distortional buckling mode interaction. **Thin-Walled Structures**, v. 137, p. 251–270, 1 abr. 2019.

MCANALLEN, L. E.; PADILLA-LLANO, D.; ZHAO, X.; MOEN, C.; SCHAFER, B. W.; EATHERTON, M. **Initial geometric imperfection measurement and characterization of cold-formed steel C-section structural members with 3D non-contact measurement techniques**. Annual Stability Conference Structural Stability Research Council. **Anais**...Toronto, Canada: 2014

MIRAMBELL, E.; REAL, E. On the calculation of deflections in structural stainless steel beams: An experimental and numerical investigation. **Journal of Constructional Steel Research**, v. 54, n. 1, p. 109–133, 1 abr. 2000.

MOEN, C. D.; IGUSA, T.; SCHAFER, B. W. Prediction of residual stresses and strains in cold-formed steel members. **Thin-Walled Structures**, v. 46, n. 11, p. 1274–1289, 1 nov. 2008.

NARAYANAN, S.; MAHENDRAN, M. Ultimate capacity of innovative cold-formed steel columns. **Journal of Constructional Steel Research**, v. 59, n. 4, p. 489–508, 1 abr. 2003.

OBST, M.; KURPISZ, D.; PACZOS, P. The experimental and analytical investigations of torsion phenomenon of thin-walled cold formed channel beams subjected to four-point bending. **Thin-Walled Structures**, v. 106, p. 179–186, 1 set. 2016.

PUMA ARMAÇÃO TRELIÇADA. Disponível em: <https://www.puma.com.br/downloads.php>. Acesso em: 15 jul. 2020.

QUACH, W.-M. **Residual stresses in cold-formed steel sections and their effect on column behaviour**. Thesis (Doctor of Philosophy) – Department of Civil and Structural Engineering, The Hong Kong Polytechnic University, 2005.

RAMBERG, W.; OSGOOD, W. R. **Description of stress-strain curves by three**

parameters. Technical Note No. 902. National Advisory Committee for Aeronautics. Washington, D.C: 1943.

RASMUSSEN, K. J. R. et al. Numerical modelling of stainless steel plates in compression. **Journal of Constructional Steel Research**, v. 59, n. 11, p. 1345–1362, nov. 2003a.

RASMUSSEN, K. J. R. Full-range stress-strain curves for stainless steel alloys. **Journal of Constructional Steel Research**, v. 59, n. 1, p. 47–61, 1 jan. 2003b.

RONDAL, J. **Coupled Instabilities in Metal Structures – Theoretical and Design Aspects**. Springer, Wien, New York: 1998.

SANTOS, W. S. **On the Strength and DSM Design of End-Bolted Cold-Formed Steel Columns Buckling in Distortional Modes**. Tese (Doutorado) – Programa de Pós-graduação em Engenharia Civil, COPPE, Universidade Federal do Rio de Janeiro, Rio de Janeiro, 2017.

SANTOS, W. S.; LANDESMANN, A.; CAMOTIM, D. Distortional strength of end-bolted CFS lipped channel columns: Experimental investigation, numerical simulations and DSM design. **Thin-Walled Structures**, v. 148, p. 1-25, 1 mar. 2019.

SARTORTI, A. L.; FONTES, A. C.; PINHEIRO, L. M. Analysis of the assembling phase of lattice slabs. **Revista IBRACON de Estruturas e Materiais**, v. 6, n. 4, p. 623–660, ago. 2013.

SCHAFER, B. W.; PEKÖZ, T. Computational modeling of cold-formed steel: characterizing geometric imperfections and residual stresses. **Journal of Constructional Steel Research**, v. 47, n. 3, p. 193–210, 1 set. 1998a.

SCHAFER, B. W. Review: The Direct Strength Method of Cold-Formed Steel Member Design. **Journal of Constructional Steel Research**, v. 64, p. 766–778, 2008.

SCHAFER, B. W.; ÁDÁNY, S. **Buckling analysis of cold-formed steel members using CUFSM: conventional and constrained finite strip methods**. 18th International Specialty Conference on Cold-Formed Steel Structures. **Anais**...Orlando, Florida: 2006.

SCHAFER, B. W.; LI, Z.; MOEN, C. D. Computational modeling of cold-formed steel. **Thin-Walled Structures**, v. 48, n. 10–11, p. 752–762, 1 out. 2010.

SCHAFER, B. W.; PEKÖZ, T. Computational modeling of cold-formed steel: characterizing geometric imperfections and residual stresses. **Journal of Constructional Steel Research**, v. 47, n. 3, p. 193–210, 1 set. 1998b.

Sheet Metal Forming. Disponível em: <http://www.custompartnet.com/wu/sheet-metal-forming>. Acesso em: 15 jul. 2020.

SIVAKUMARAN, K. S.; ABDEL-RAHMAN, N. A finite element analysis model for the behaviour of cold-formed steel members. **Thin-Walled Structures**, v. 31, n. 4, p. 305–

324, 1 ago. 1998.

STORCH, I. S.; DOBELIN, J. G. S.; BATALHA, L. C.; SARTORTI, A. L. Self-supporting tests in lattice joists subject to negative bending. **Revista IBRACON de Estruturas e Materiais**, v. 10, n. 6, p. 1366–1395, nov. 2017.

SUN, J.; BUTTERWORTH, J. W. **Behaviour of steel single angle compression members axially loaded through one leg**. Proc. Australasian Struct. Engrg. Conference, Auckland. **Anais**...1998.

TAKEY, T. H. **Sistemas de Laje Mista para Edificações com uso de Perfis de Chapa Metálica**. Dissertação (Mestrado) – Departamento de Engenharia Civil, Pontifícia Universidade Católica do Rio de Janeiro, Rio de Janeiro, 2001.

THOMPSON, M. K.; THOMPSON, J. M. **ANSYS Mechanical APDL for Finite Element Analysis.** Pittsburdh, USA: Elsevier Science, 2017.

TORABIAN, S.; ZHENG, B.; YARED, S.; SCHAFER, B. W. Direct Strength Prediction of Cold-Formed Steel Beam-Columns. **Reseacrh Report RP16-3 sponsored by AISI**, 2016a.

TORABIAN, S. et al. **Finite element modeling protocols and parametric analyses for short cold-formed steel zee-section beam-columns**. Structural Stability Research Council Annual Stability Conference 2016, SSRC 2016. **Anais**..., p. 305–316, 2016b.

TORABIAN, S.; ZHENG, B.; SCHAFER, B. **Experimental study and modeling of cold-formed steel lipped channel stub beam-columns**. Structural Stability Research Council Annual Stability Conference 2014, SSRC 2014. **Anais**...2014

TORABIAN, S.; ZHENG, B.; SCHAFER, B. W. Experimental response of cold-formed steel lipped channel beam-columns. **Thin-Walled Structures**, v. 89, p. 152–168, 2015.

Trelifácil® - Lajes Real. Disponível em: <https://lajesreal.blog/trelifacil/>. Acesso em: 15 jul. 2020.

TUPER. **Catálogo da Tuper**. Disponível em: <https://www.tuper.com.br/lajes/#informacao-tecnica>. Acesso em: 24 fev. 2019.

VIANNA, J. C. **Sistema de laje-mista para edificações residenciais com o uso de perfis embossados de chapa dobrada**. Dissertação (Mestrado) – Departamento de Engenharia Civil, Pontifícia Universidade Católica do Rio de Janeiro, Rio de Janeiro, 2005.

VIEIRA JUNIOR, L. C. M. **Análise numérica do comportamento estrutural e da resistência de terças de aço restringidas pelas telhas**. Dissertação (Mestrado) – Escola de Engenharia de São Carlos, Universidade de São Paulo, São Carlos, 2007.

VIEIRA, J. D. **Estudo teórico-experimental do comportamento de laje mista com**

perfis incorporados de chapa dobrada. Dissertação (Mestrado) – Departamento de Engenharia Civil, Pontifícia Universidade Católica do Rio de Janeiro, Rio de Janeiro, 2003.

YE, J.; HAJIRASOULIHA, I.; BECQUE, J.; PILAKOUTAS, K. Development of more efficient cold-formed steel channel sections in bending. **Thin-Walled Structures**, v. 101, p. 1–13, 1 abr. 2016.

YE, J.; BECQUE, J.; HAJIRASOULIHA, I.; MOJTABAEI, S. M.; LIM, J. B. P. Strength and deflection behaviour of cold-formed steel back-to-back channels. **Engineering Structures**, v. 177, p. 641–654, 15 dez. 2018.

YOUNG, B. Design of channel columns with inclined edge stiffeners. **Journal of Constructional Steel Research**, v. 60, n. 2, p. 183–197, 1 fev. 2004.

YOUNG, B.; RASMUSSEN, K. J. R. Design of Lipped Channel Columns. **Journal of Structural Engineering**, v. 124, n. 2, p. 140–148, fev. 1998.

YOUNG, W. C.; BUDYNAS, R. G. **Roark's Formulas for Stress and Strain**. Seventh ed. New York: McGraw-Hill, 2002.

YU, C.; SCHAFER, B. W. Simulation of cold-formed steel beams in local and distortional buckling with applications to the direct strength method. **Journal of Constructional Steel Research**, v. 63, n. 5, p. 581–590, 1 maio 2007.

YU, W. W.; LABOUBE, R. A.; CHEN, H. **Cold-formed steel design**. 5th ed. John Wiley and Sons, 2019.

YUAN, W. BIN. Nonlinear instability analyses of channel-section beams subjected to minor-axis pure bending. **International Journal of Mechanical Sciences**, v. 73, p. 77–81, 2013.

YUAN, W.; CHEN, C. Nonlinear Bending Response and Buckling of Channel Section Beams of Finite Length under Minor-Axis Pure Bending. **Advances in Structural Engineering**, v. 18, n. 7, p. 1043–1050, 1 jul. 2015.

ZEINODDINI, V. M. **Geometric imperfections in cold-formed steel members**. Thesis (Doctor of Philosophy) – Department of Civil Engineering, Johns Hopkins University, Baltimore, Maryland, 2011.

ZEINODDINI, V. M.; SCHAFER, B. W. Simulation of geometric imperfections in cold-formed steel members using spectral representation approach. **Thin-Walled Structures**, v. 60, p. 105–117, 1 nov. 2012.

ZHOU, Z.; XU, L.; SUN, C.; XUE, S. Brazier Effect of Thin Angle-Section Beams under Bending. **Sustainability**, v. 10, n. 9, p. 3047, 27 ago. 2018.

ZIEMIAN, R. D. **In Guide to Stability Design Criteria for Metal Structures:** 6th ed. Wiley, 2010.

ZIENKIEWICZ, O. C.; TAYLOR, R. L. **The finite element method for solid and structural mechanics**. 6th ed. Elsevier, 2005.